msc

Materials Sciences Corporation

LEVEL II

(12)

P.

STUDY OF GRAPHITE/EPOXY

COMPOSITES FOR MATERIAL

FLAW CRITICALITY

S.N. CHATTERJEE AND R.B. PIPES

APPROVED FOR PUBLIC RELEASE; DISTRIBUTION IS UNLIMITED.

PREPARED FOR:
NAVAL AIR DEVELOPMENT CENTER
WARMINSTER, PENNSYLVANIA

MSC TFR-1106/1103
NADC-78241-60
NOVEMBER, 1980

81 7 13 079

msc

Materials Sciences Corporation

STUDY OF GRAPHITE/EPOXY COMPOSITES

FOR MATERIAL FLAW CRITICALITY

MSC TFR 1106/1103
Technical Final Report
November 1980

Prepared by:

S. N. Chatterjee

R. B. Pipes

Prepared for:

Naval Air Development Center
Warminster, PA

under Contract N62269-79-C-0209

(9) Final rept. 1? Fr. '79-31 Oct ??)

(14) REPORT DOCUMENTATION PAGE	READ INSTRUCTIONS BEFORE COMPLETING FORM	
1. REPORT NUMBER (18) NADC-78241-60	2. GOVT ACCESSION NO. AD-A101492	3. RECIPIENT'S CATALOG NUMBER
4. TITLE (and Subtitle) Study of Graphite/Epoxy Composites for Material Flaw Criticality	5. TYPE OF REPORT & PERIOD COVERED Final	
	6. PERFORMING ORG. REPORT NUMBER (14) MSC/TFR/1106/1103	
7. AUTHOR(s) S.N. Chatterjee R.B. Pipes	8. CONTRACT OR GRANT NUMBER(s) (13) N62269-79-C-0209	
9. PERFORMING ORGANIZATION NAME AND ADDRESS Materials Sciences Corporation Blue Bell Office Campus Merion Towle House, Blue Bell, PA 19422	10. PROGRAM ELEMENT, PROJECT, TASK AREA & WORK UNIT NUMBERS (12) 146	
11. CONTROLLING OFFICE NAME AND ADDRESS Naval Air Development Center Warminster, PA	12. REPORT DATE October 31, 1980	
	13. NUMBER OF PAGES 145	
14. MONITORING AGENCY NAME & ADDRESS(if different from Controlling Office) (11) Nov 80	15. SECURITY CLASS. (of this report) Unclassified	
	15a. DECLASSIFICATION DOWNGRADING SCHEDULE	

16. DISTRIBUTION STATEMENT (of this Report)

Approved for public release, distribution unlimited

17. DISTRIBUTION STATEMENT (of the abstract entered in Block 20, if different from Report)

18. SUPPLEMENTARY NOTES

19. KEY WORDS (Continue on reverse side if necessary and identify by block number)

Composite Materials
Non-destructive Evaluation
Graphite/Epoxy
Delamination,
Buckling, Fatigue,

Non-destructive testing
Defect Characterization
Fracture Mechanics
Ultrasonic Wave Propagation,
Moisture Conditioning

20. ABSTRACT (Continue on reverse side if necessary and identify by block number)
Usefulness of NDE methodology for assessing criticality of disbonds with two-dimensional planforms located in laminated graphite/epoxy composites has been examined. Linear elastic fracture mechanics approach, semi-empirical growth laws and methods of stress analysis based on a modified laminated plate theory have been studied for assessing growth rates of disbonds in a transverse shear environment. Elastic stability analysis has been utilized for laminates with disbonds subjected to in-plane compression and/or shear.

DD FORM 1473   EDITION OF 1 NOV 65 IS OBSOLETE
1 JAN 73

-ii-

Results of nondestructive inspections and destructive tests
have been correlated with analytical predictions. In addition,
effects of moisture conditioning and cyclic loading on wave
velocities and attenuation of sound in graphite/epoxy composites
and in neat resin samples have been studied.

SUMMARY

Usefulness of NDE methodology for assessing criticality of disbonds with two-dimensional planforms located in laminated Graphite/Epoxy composites has been examined. A linear elastic fracture mechanics approach, semi-empirical growth laws, and methods of stress analysis based on a modified laminated plate theory have been studied for assessing growth rates of disbonds in a transverse shear environment. Elastic stability analysis has been utilized for laminates with disbonds subjected to in-plane compression and/or shear.

Results of nondestructive inspections and destructive tests have been correlated with analytical predictions. In addition, effects of moisture conditioning and cyclic loading on wave velocities and attenuation of sound in Graphite/Epoxy composites and in neat resin samples have been studied.

Accession For	
NTIS GRA&I	X
DTIC TAB	☐
Unannounced	☐
Justification	
By	
Distribution/	
Availability Codes	
Dist	Avail and/or Special
A	

FOREWORD

Approved:

B. Walter Rosen
Program Director

TABLE OF CONTENTS

TABLE OF CONTENTS (Continued)

LIST OF TABLES

LIST OF FIGURES

INTRODUCTION

Use of nondestructive evaluation techniques for assessing criticality of defects in aircraft structural components is an attractive method for defining their residual strength or lifetime. It also provides a basis for defining regular inspection intervals for a structural element during its service and for determining the need for mandatory repair. Application of such techniques to components made of fiber reinforced composites is being studied by various investigators. A number of nondestructive inspection techniques have been and are being examined for detecting flaws in composite structural members and quantifying their location, size, and shape. These include ultrasonics, acoustic emission, x-ray and thermography, use of penetrants as well as holography.

After the flaw characteristics have been quantified by means of ND measurements, it is necessary to assess criticality by the use of analytical techniques. For metal structural components such techniques are well known and their validity is well established. Since fiber composites have been in use for only a few years, suitable analytical methodologies for the definition of critical flaws are not fully developed. Also, because of their highly anisotropic properties, stress analysis in a flawed composite component involves lengthy and complicated computations and different types of flaws may result in a wide variety of failure modes. For these reasons usefulness of analytical methods for assessing flaw criticality in composite structures has not been clearly demonstrated.

Since it is practically impossible to use a single analytical technique to cover the whole spectrum of fatigue, fracture and/or failure for various types of flaws, a logical procedure for studying criticality is to select a few types of commonly encountered flaws and develop appropriate analytical models for each type of defect. Such analytical studies should, of course,

be supplemented with nondestructive as well as destructive tests to examine the range of validity of the model. Such attempts have been made in references 1 and 2 for interlaminar disbonds in a laminated beam. These defects are quite common in laminated members because they can exist as "birth" defects or can be created during service by foreign object impact or various other reasons. Presence of a disbond does not affect the structural performance of a laminated beam or plate member under in-plane loads except when such loads can cause local buckling due to in-plane compression or shear. Under transverse shear, catastrophic and slow growth of a disbond may occur due to quasi-static and cyclic loading, respectively. Criticality and growth rate of disbonds in laminated beams under quasi-static or cyclic transverse shear have been determined (ref. 2) by the use of principles and methods of fracture mechanics as well as empirical crack growth laws. Failure of a disbonded laminate under compressive loading has been defined in terms of buckling and an elastic stability analysis has been utilized for assessing criticality. Sizes and shapes of disbonds implanted in test specimens have been quantified and their growth monitored by the use of ultrasonic "C" scans. Results from tests have been compared with analytical predictions and usefulness of the NDE methodology has been demonstrated. An approach, which is qualitatively similar to the one described above, has been utilized in reference 3 for studying growth of inherent disbonds ("birth" defects) in laminated composites subjected to compression fatigue. Although the philosophy and the analytical methodology of assessing criticality of disbonds have been shown to be effective, their range of validity as well as their usefulness for more complicated disbond geometries and loading conditions are yet to be demonstrated. The work reported in this study is an attempt in this direction.

In the present work, ultrasonic "C" scans are used to quantify shapes of disbonds with nearly elliptic planforms which are implanted in wide beams. "C" scans are also used to monitor growth

of the disbonds under cyclic transverse shear. Destructive tests
are performed to determine quasi-static failure. Sandwich beams
with compression skins containing circular as well as nearly el-
liptic disbonds are loaded to failure for determining criticality
of the disbonded skin.

Analytical methods are developed for determining the effect
of elliptic shaped disbonds on the stress field in a composite
laminate. The analysis yields the strain energy release rates,
G_I, G_{II}, and G_{III}, associated with opening (Mode I), sliding
(Mode II), and tearing (Mode III) modes, respectively, as func-
tions of position along the boundary of the disbond. The possi-
bility of predicting flaw growth under cyclic loading is examined.
Effects of in-plane compressive or shear loads are also included
in the analysis, and therefore, failure of disbonded laminates
due to elastic instability is also predicted. Data correlation
studies are performed with the help of experimental data.

In addition, wave propagation studies are performed on resin
and laminate samples, for quantifying changes in wave velocity
and attenuation induced by moisture conditioning and fatigue
damage. Results are studied to examine the usefulness of velo-
city and attenuation measurements as NDT techniques for quantita-
tive assessment of such damages.

ANALYTICAL METHODS

DESCRIPTION OF THE MODEL

A laminated composite plate of finite thickness with a delamination between any two of the laminae, as shown in figure 1, is considered in this study. The displacements and stresses in such a plate, due to applied loads, can be calculated as the sum of the solutions of two problems as described below.

1. The problem of calculation of stresses and displacements without the presence of the flaw - self-equilibrating surface tractions on the two surfaces of the delamination, as determined from this solution, are used as inputs for the second problem.

2. Effects of tractions equal in magnitude but opposite in sign to those calculated in (1), acting on the surfaces of the delamination.

In many cases the solution to the first problem is either known or can be determined by known analytical techniques using two-dimensional elasticity or laminated plate theories. When the periphery of the delamination is located quite far from the edges of the plate, the solution to the second problem is insensitive to the boundary conditions at these edges and therefore, the flaw is assumed to be located in a plate of finite thickness, but the other two dimensions of the plate are infinitely large.

A rigorous three-dimensional elasticity solution of the second problem under consideration seems possible, but will be extremely complicated because of the anisotropy of the individual layers as well as the laminated structure of the plate. The complexity of the problem will be clear from past studies on a two-dimensional elasticity solution for the problem of a laminated composite beam containing delaminations (refs. 2,4) and a three-dimensional elasticity solution for an elliptic crack in an

anisotropic medium (refs. 5,6). In this study a lower order structural theory, based on a laminated plate theory with shear deformations (ref. 7) which is modified as described in Appendix A-1 to include the effects of tractions on the bounding surfaces of the plate (see fig. 2), is used to obtain results for the following cases.

1. Contributions of mode I, mode II and mode III types of deformations to strain energy release rates as functions of position on the periphery of a disbond with elliptic plan form as shown in figure 1.
2. Critical values of membrane stresses (compressive, as shown in fig. 1, or shear) to cause buckling failure of the unsupported part of the compression skin above the disbond.

Under the assumptions of shear deformation plate theory and Griffith separation, the analysis for case (1) is self-consistent and yields an exact solution. The model consists of two laminated plates, as shown in figure 1, bonded to each other everywhere except over the area of the disbond. As described in Appendix A-2, the theory admits the presence of three distinct singularities at the periphery of the disbond associated with normal and two tangential stresses in the form of line loads due to discontinuities in displacement gradients across the disbond boundary, thus yielding finite values of G_I, G_{II} and G_{III}, the strain energy release rates corresponding to modes I, II and III, respectively. These types of singularities have been noted in the dynamic problem of debonding of a Timoshenko-beam from a rigid substrate (ref. 8). Quasi-static growth of disbonds have also been studied by several authors (refs. 8-18) using various types of structural theories. Results from references 18 and 1 are compared in references 2 and 4 with a 2-D elasticity solution for a laminated beam containing delaminations in an environment dominated by transverse shear stresses. The comparison shows

that the strain energy release rates obtained from the two theor-
ies are close to each other when the ratio of disbond length to
the thickness of each of the two beams in the disbonded laminate
is greater than five. For decreasing values of disbond length,
the lower order theory results become non-conservative. This
phenomenon is expected because of inherent limitations in the
shear deformation beam theory. It is noted, however, that for
small values of disbond length, flexural failure of composite
laminates usually occurs before catastrophic disbond propagation
is initiated under quasi-static load, although slow disbond
growth may occur under cyclic loading (ref. 1). Also, when the
disbond length is only an order of magnitude higher than the
diameter of fibers, or fiber spacing, use of elasticity theory
with the assumption that the individual layers are homogeneous
becomes questionable and further refinements in analysis seems
either impossible or too complicated. It appears, therefore,
that for all practical purposes shear deformation theory used
herein is quite adequate for a wide range of disbond size. For
cyclic loading, semi-empirical growth laws of the type given be-
low are commonly used for metals, where a single mode of deforma-
tion (I, II or III) is usually dominant.

$$\frac{da}{dN} = C(\Delta K - \Delta_0 K)^n \tag{1}$$

where a = crack length,

   N = number of cycles,

   C,n = empirical constants

   ΔK = stress intensity factor range = $K_{max} - K_{min}$, and

   $\Delta_0 K$ = the threshold value of ΔK below which propagation does
        not occur.

Equation (1) is commonly used for studying self-similar
crack growth in 2-D problems and has been used for modeling the
growth of disbonds in composite laminates (refs. 2,3). Since
the model used here does not yield the stress intensity factors,
use of the following relationship may be attempted.

$$\frac{da}{dN} = C_1 [\Delta(\sqrt{G}) - \Delta_0(\sqrt{G})]^n \tag{2}$$

where $\Delta(\sqrt{G}) = \sqrt{G_{max}} - \sqrt{G_{min}}$, and

$\Delta_0(\sqrt{G})$ = the threshold value of $\Delta(\sqrt{G})$ below which propagation does not occur.

da can be considered as the movement of the disbond front in the direction of current normal. Equation (2) is consistent with (1) because the strain energy release rate is proportional to the square of the stress intensity factor.

For the buckling failure outlined in case (2), use of an iterative procedure yields critical loads based on linearized theory of elastic instability. Use of such a lower order theory for sandwich beams containing a disbonded compression skin has been found to predict buckling failure at loads close to experimentally observed values as long as the disbond length is sufficiently large. For small disbond lengths, the predictions tend to become non-conservative because of two reasons; namely: (i) inelastic buckling; and (ii) inherent limitations of shear deformation beam theory for small length to depth ratio. Theoretical results are, however, useful for a wide range of disbond length.

METHOD OF ANALYSIS

Double Fourier transform is made use of (see Appendix A-2) to handle the system of governing differential equations given in Appendix A-1. Three unknown functions are introduced to characterize the discontinuities in displacements in three directions over the area of the disbond. Elliptic disbonds are mapped onto a circle ($r \leq 1, 0 \leq \theta \leq 2\pi$) by a simple transformation and the unknown functions $u_k^*(r,\theta)$ and the three prescribed tractions $t_k(r,\theta)$, (k=1,2,3) are expanded in Fourier series in θ.

$$u_k^*(r,\theta) = \sum_{p=-\infty}^{\infty} r^{|p|} u_{kp}^*(r^2) e^{ip\theta}$$

$$(3)$$

$$t_k(r,\theta) = \sum_{p=-\infty}^{\infty} t_{kp}(r) e^{ip\theta}$$

where $u_{k(-p)}^*$ and $t_{k(-p)}$ are complex conjugates of u_{kp}^* and t_{kp}, respectively.

Introduction of the variables $u_{kp}(r^2)$ and $t_{kp}^*(r)$ given by

$$r\, u_{kp}(r^2) = \frac{d}{dr} u_{kp}^*(r^2) \qquad ; \quad 0<r<1$$

$$(4)$$

$$t_{kp}^*(r) = \int_0^r t_{kp}(r) r^{p+1} dr$$

and expansion of real and imaginary parts of u_{kp} and t_{kp}^* in a series of Legendre polynomials $P_{n-1}(2r^2-1)$, $n=1,2\ldots\infty$ as well as other algebraic manipulations results in an infinite system of linear algebraic equations which must be solved to determine the unknown constants u_{kpq_2n} for known values of the expansion coefficients $t_{jmp_1n'}$.

$$\sum_{q_1=1}^{2} \sum_{k=1}^{3} \sum_{p=0}^{\infty} \sum_{n=1}^{\infty} L_{kpq_2n}^{jmq_1n'} u_{kpq_2n} = t_{jmq_1n'} \; ; \; \begin{array}{l} j = 1,2,3 \\ m = 0,1,2\ldots\infty \\ q_1 = 1,2 \\ n' = 1,2,\ldots.\infty \end{array}$$

$$(5)$$

The expression for the elements of the matrix L, other details and method of calculation of strain energy release rates G_I, G_{II} and G_{III} are given in Appendix A-2. For the purpose of numerical solution it is necessary to truncate the system (equation 5) such that $m,p \leq m_{max}$ and $n,n' \leq n_{max}$. For orthotropic laminates with x,y as principal axes, the set of equations for u_{kp1n} and u_{kp2n} are uncoupled and are solved separately.

The condition that the system of equations is homogeneous, i.e. the determinant of the coefficient matrix is equal to zero, yields the critical loads for the buckling problem. Since the values of prestress enter each of the terms of the coefficient matrix in a complex fashion, the condition yields a complicated transcendental equation and therefore, the critical loads must be determined by trial and error procedures.

EXPERIMENTAL PROGRAM

SHEAR TESTS ON THICK DISBONDED LAMINATES

Specimen Geometry and Fabrication

Thick 64-ply Graphite/Epoxy laminates of stacking sequence
of $[(0_4/\pm 45_2/\mp 45_2/0_4)_s]_s$ were tested in three point bending with
a span of 152.4 mm. Specimens were 254 mm. in length, 76.2 mm.
in width and approximately 9.73 mm. in thickness. Two teflon
disbonds were implanted at the midsurface (between plies 32 and
33) in each specimen. The two disbonds were placed symmetri-
cally with respect to the center of the beam span. To minimize
the influence of free edges, widths of the flaws did not exceed
one-half of the specimen width. Criticality of various flaw
geometries were examined by using five different sizes and
shapes of disbond, namely: (i) circular disbonds of 25.4 mm.,
31.75 mm. as well as 38.1 mm. in diameter; (ii) oblong shaped
disbonds with semicircular ends of dimensions 31.75 mm. x 25.4
mm. and 38.1 mm. x 25.4 mm. (fig. 3). The oblong shaped dis-
bonds were placed in the beams with their largest dimension
parallel to the length of the beam. Centers of the disbonds
were located either ± 38.1 mm. or ± 50.8 mm. from the center of
the beam. The Teflon-Teflon disbonds were constructed from a
stock FEP Teflon film .0254 mm. in thickness by doubling the
sheet and using a steel punch to cut it in the shape of the dis-
bond geometry (fig. 4).

Hercules AS/3501-6 Graphite/Epoxy material in the form of
304.8 mm. wide prepreg tape was laminated into panels measuring
355.6 mm. in width by 355.6 mm. in length. Each panel was as-
sembled from two half panels of 32 plies, each having the stack-
ing sequence $(0_4/\pm 45_2/\mp 45_2/0_4)_s$. Four specimens were obtained
from each processed panel. After being processed, the panel was
inspected ultrasonically to check laminate integrity and deter-
mine the exact location of the specimens within the processed

panel. Individual specimens were cut from the panel using a
diamond impregnated saw.

Test Procedure

The thick laminated beams were tested in a three-point bend-
ing fixture, shown in figure 5. The 9.53 mm. round steel load
reaction pins ① served to transmit a line load across the
width of the beam. Support arms ② (fig. 6) were rigidly con-
nected to the main frame rail ③ . During preliminary tests
the 9.53 mm. loading nose ① caused localized delaminations and
surface damage which was corrected by inserting a 12.7 mm. x 76.2
mm. x 3.18 mm. copper pad ④ between the steel nose and specimen
surface.

Static tests were conducted in an Instron model TTCML Univer-
sal testing machine using a crosshead speed of 0.05 cm./min.
Failure was determined as the maximum load recorded on the load
deflection curve. Fatigue loading was performed in an Instron
model 1321 servo-hydraulic test frame. Sinusoidal loading was ap-
plied at a frequency of 10 Hz with a minimum to maximum stress
amplitude ratio of 0.1. The test duration was nominally 10^6 cy-
cles with periodic monitoring of the flaw propagation at selected
intervals during the load history.

Prior to testing, specimens were ultrasonically C-scanned to
provide initial flaw measurements and locate the midpoint between
the two disbonds. A line was marked on each beam corresponding
to the center of the span. The specimen was fatigue tested for
an interval, then C-scanned. In the beginning, C-scans were taken
after every 5,000 or 10,000 cycles. Once a feel for the growth
characteristics was obtained, appropriate test intervals were used
to expedite testing, based on disbond size and S-level. Once
propagation of the defect occurred, intervals were reduced for de-
tailed characterization of flaw growth. Termination of a test
occurred when the flaw failed to propagate despite continued

cycling, or when the specimen failed through catastrophic crack propagation. Tests were conducted at S-levels of 0.4, 0.5 and 0.6 depending on the size of the disbonds.

Pulse echo ultrasonic inspection was used to nondestructively monitor the flaw propagation during the tests. The ultrasonic system consists of a model 5052 Panametrics ultrasonic analyzer, Tektran tank with scanner and hot pen recorder, and a Tektronix dual trace oscilloscope. The gated peak detector section of the ultrasonic analyzer was used to select the portion of the waveform corresponding to the implanted defects enabling the study to focus on damage propagation from the implanted flaws.

Test Results

The results of the static tests were primarily utilized in the determination of the stress levels used in the fatigue program. The data are presented in table 1. All specimens first failed in flexure, then subsequently failed in shear (see fig. 7). Observation of specimen failures indicates tensile failure of ±45° plies adjacent to the outer 0° plies (plies 59-60). This led to subsequent failure of the 0° plies. Additional loading of the specimen caused the specimen to fail in shear.

Load levels for fatigue tests were determined based on a static failure load of 29,400N, which was estimated from the first few of the static tests. The data obtained from the fatigue testing program were compiled and produced as tables and graphs of crack length versus cycles. These results can be found in reference 19. C-scans of some of the specimens are shown in figures 8-18.

Two disbonds in each specimen gave rise to four crack fronts. Disbond I was the upper disbond (nearest the I.D. number), II the lower disbond. A and B were symbols used to denote the upper and lower halves of disbonds I and II, respectively. Likewise, C and D denoted the upper and lower halves of disbond II (see fig. 19).

These four disbond halves A, B, C and D initiated the four crack fronts. Measurements of crack lengths were taken at three points along each crack front (locations 1, 2 and 3 in the figure). These measurement locations were independent of disbond geometry or load level.

The number of cycles to which the specimens were loaded is listed in table 2, where the defect size in inches indicates the largest dimension of the initial flaw. The letters C and 0 indicate circular or oblong shaped flaws. For all oblong shaped flaws the minimum dimension was 25.4 mm. The location indicates the distance of the center of the flaw from the center of the beam.

SANDWICH BEAM TESTS

Sample Geometry and Fabrication

The specimen geometry consisted of a 22.0 in. x 3.0 in. x 1.6 in. (55.9 cm. x 7.6 cm. x 4.1 cm.) sandwich beam with a 12-ply 0° laminate on the tensile side and a $[(0/\pm45)_s]_s$ laminate on the compressive side. The core material was 24 lb. Hexcel aluminum honeycomb and the laminates were made of AS/3501-6 Graphite/Epoxy. The Graphite/Epoxy face sheets were bonded to the honeycomb core using FM300M sheet adhesive.

Before processing in the autoclave, the face sheets measured 0.064 in. (1.63 mm.) and the honeycomb core measured 1.503 in. (38.2 mm.). After processing the finished specimen measured 1.630 in. (41.4 mm.). This indicates that the core was compressed during the processing and bond line thickness could not be measured by a sum of the parts technique. The core compression ranged from 0.001 in. (0.025 mm.) to 0.003 in. (0.076 mm.). Bond line thickness was approximately 0.001 in. (0.025 mm.) as measured by microscopy. During the lay-up of the $[(0/\pm45)_s]_s$ face sheets, two-layer Teflon defects were imbedded between the

midplies, or between the -45° plies, three plies from the exposed face. The defects were of either circular or oblong geometries and were made by punching two-ply 0.001 in. (0.025 mm.) thick Teflon film against an abrasive surface. The abrasive surface causes the two layers of Teflon to bond together and form a Teflon-to-Teflon defect. The study required the fabrication of 18 sandwich beams with the defect sizes and locations given in table 3. In addition to those listed, one beam was fabricated with 1.5 in. circular defects implanted between the midplies of both the 12-ply 0° and the $[0/\pm 45_2/0]_s$ laminates. A schematic of the aluminum honeycomb, Graphite/Epoxy sandwich beam and the load application points is shown in figure 20.

Pretesting Ultrasonic C-Scan Inspection

Prior to testing, all samples were ultrasonically inspected to determine defect size and location. Using the ultrasonic C-scans as a reference, strain gages were applied to both the tensile and compressive faces at the center of the defect. A representative C-scan of each type of specimen is shown in figures 21a through 21f.

Testing Procedure

The experimental test setup is shown schematically in figure 22. Load and strain information was put into Vishay model 2120 bridge amplifiers and the conditioned output was graphed on two X-Y plotters. Load versus compressive strain was monitored on plotter No. 2. Loading was discontinued if buckling was observed or upon laminate failure. If buckling occurred, the sandwich beam was removed from the test machine and an ultrasonic C-scan performed on the sample to determine the presence and extent of any propagated interlaminar damage. After the ultrasonic nondestructive inspection, the specimen was tested beyond the buckling

-14-

load and removed from the test machine at intervals to character-
ize the extent and growth of damage. Figure 23 shows ultrasonic
C-scans of a near surface delamination specimen at various stages.
Figures 24 through 28 are representative photographs of failures
of the specimens. Photographs of some more specimens can be
found in reference 20.

Test Results

Three beams of each of the previously mentioned configura-
tions were tested and the results are summarized in table 4. For
the case of near surface defects, which showed some indication of
buckling prior to final failure, the test data are reported in
table 5.

Typical test results for some of the different configura-
tions tested are given in graphic form in figures 29 through 32.
These results show graphs of load and stress versus compressive
strain. Other typical results can be found in reference 20. In
all cases involving midply defects, the failures were instantan-
eous and catastrophic. For the near surface defect tests, test
results indicated that failure appeared to have started as buck-
ling above the defect region and progressed with increasing
damage to the surface plies. Failure continued with the instan-
taneous and catastrophic failure of the plies below the implanted
delamination. However, except for one specimen, all of the sam-
ples tested showed a sudden change in any reversal of strain in
the compression skin. The last of the samples with a 1.5 in.
near surface defect (see table 5), which appeared to have a de-
formed shape prior to testing, showed an increase in compressive
strain with initial loading and gradual decrease at a later stage.
This behavior, which is the characteristic of Euler type buckling,
is shown in figure 32.

ULTRASONIC WAVE PROPAGATION STUDIES

Sample Geometries

The specimens were prepared from 32-ply laminates of AS/
3501-6 Graphite/Epoxy. The two laminate configurations were
$[\pm 45_8]_s$ and $[0_{32}]$ and the laminates were machined into 1 in. x
9 in. tensile coupons. Resin samples were prepared from the
AS/3501-6 resin system at the University of Wyoming. The speci-
mens were cured at 177°C (350°F) and were then cut into 2.54 cm.
x 22.86 cm. (1 in. x 9 in.) test coupons. The surfaces had to
be ground in order to remove surface defects which consisted of
multiple shallow depressions a square inch or more in area and
a few thousandths of an inch deep. The specimens were then
post-cured for eight hours at 218°C (425°F) and the surfaces
were polished. Occasionally there are dark flecks in some of
the specimens. These appear to be impurities or contamination
in the resin as received from Hercules, Inc. The grinding and
polishing produces an excellent surface; however, examination
of the specimens in a polariscope indicate some residual stress-
es which were not completely annealed out during post-cure. An
attempt at a 204°C (400°F) post-cure for 10 hours was almost
totally ineffective in reducing the residual stresses.

Signal Processing Facility

The signal processing facility developed for the analysis
of ultrasonic waveforms is shown schematically in figure 33.
The system's input/output (I/O) components are a DEC LA36 paper
terminal, a Tektronix CRT graphic display terminal, a paper tape
reader/punch, and an Omnitec telephone modem. These components
are all directly connected to either the parallel or serial in-
terface ports of a Digital LSI 11 minicomputer which was expand-
ed by an additional 16 dual card slots in a Digital expansion
unit.

The data sampling and digitizing component in the system is a Nicolet digital oscilloscope. The oscilloscope has a maximum sampling rate of 20 MHz and digitizes the input to eight bits. The oscilloscope has the ability to store waveforms on a self-contained floppy disk and can also output waveforms to a flatbed plotter. Since the maximum frequency which can be digitized on this unit without aliasing is 10 MHz, a 10 MHz low-pass filter, whose 3-dB point is at 10 MHz and which is 65 dB down at 11 MHz, is used to pre-filter all inputs. A peripheral interface was constructed to join the Nicolet oscilloscope to the LSI 11 computer. The interface expands 16 input bits and 25 output bits on the LSI 11 to 112 input bits and 112 output bits. The oscilloscope requires 25 input bits and 20 output bits for control and data input and output. The remaining bits of the interface will be used for system expansion. All output bits are tristate-controlled from the front panel of the peripheral interface. This allows data and control lines to be set in the proper state prior to data transmissions and also allows manual operation of the oscilloscope. In order to perform the required data transmissions and manipulations, a control program named NICDAT was written in LSI 11 machine language. The details of this program and a listing of support programs are given in reference 21. The primary use of the NICDAT program is to control the peripheral interface and to transfer data, between set limits, from the Nicolet oscilloscope to the Burroughs B7700 computer where the data can be stored and analyzed.

The support programs allow the user to make velocity of sound measurements, attenuation measurements, interpolate the waveform using frequency domain information and obtain frequency spectra. The velocity of sound is obtained from measurements of the phase of the front surface echo and back surface echo independently. The phase of the two echoes can be determined from the Fourier transform of the individual echoes. This phase information can be used to determine the velocity of sound in the sample

as a function of frequency, and the theory behind the measurement is diagrammed in figure 34. A phase measurement is made of the first surface ϕ_0 and at the second surface ϕ_1. The thickness of the sample must be measured at the point on the sample where the phase measurements are made. With this information, the velocity of sound can be evaluated using equation (6).

$$c(\omega) = \frac{2d\omega}{[\phi_1(\omega) - \phi_0(\omega)]} \tag{6}$$

The results of this computation are shown for a 6.35 mm. (1/4 in.) Graphite/Epoxy sample in figure 35.

Attenuation of sound measurements are made using either frequency domain information or amplitude information. Using the Fourier transform of the front surface echo, back surface echo and second multiple echo, the attenuation coefficient α can be evaluated as a function of frequency ω using equation (7).

$$\alpha(\omega) = \frac{-1}{d} \ln \left[\left| \frac{R_3(\omega)}{R_2(\omega)} \right| + \left| \frac{R_2(\omega)}{R_3(\omega)} \right| \right] \tag{7}$$

$R_1(\omega)$, $R_2(\omega)$ and $R_3(\omega)$ are the magnitudes of the Fourier transforms of the three echoes mentioned and d is the thickness of the sample. An example of this measurement for 32-ply, 0° Graphite/Epoxy is shown in figure 36. The vertical lines in the waveform at the top of the figure indicate the boundaries of the Fourier transform of each echo.

The attenuation of sound may also be measured using the amplitudes of the echoes; however, α in this case will not be a function of frequency ω. For this measurement, equation (8) is used.

$$\alpha = \frac{-1}{2d} \ln \left[(R_3/R_2) - (R_2/R_1) \right] \qquad (8)$$

where: α is the linear amplitude attenuation coefficient in mm^{-1};

     d is the sample thickness in mm;

     R_1 is the amplitude of the front surface echo;

     R_2 is the amplitude of the back surface echo;

     R_3 is the amplitude of the second multiple echo.

Due to the inversion which occurs at the back surface interface, R_2 and R_3 are measured on the opposite side of the axis from R_1. The transducer used in all of the velocity and attenuation measurements is a 5 MHz type. The attenuation measured at 5 MHz for a 0° sample was 0.053 $mm.^{-1}$ using the frequency technique, and the attenuation was 0.061 $mm.^{-1}$ using the amplitude technique. There is a 13% difference between these measurements and this difference is typical of Graphite/Epoxy composites. The difference decreases to approximately 5% for more homogeneous materials such as the neat resin samples tested.

Data Scattering Test Results

In order to determine the reproducability of the ultrasonic velocity and attenuation measurements, eight sets of data were taken at several locations in a 32-ply ±45° Graphite/Epoxy test coupon. Four measurements (FORSCATA-FORSCATD) were made at the center of the sample without moving the transducer and four measurements (FORSCATE-FORSCATH) were made around a 1.27 mm. (0.050 in.) diameter circle 90° apart. The results of the velocity measurements are tabulated at 1 MHz intervals in reference 21, where the data are also plotted graphically. A 5 MHz nonfocused transducer was used to make all measurements. The transducer was positioned above the sample for a main bang delay of 137 µsec. (approximately 10.16 cm.). Although efforts were made to keep

the transducer stationary, it is indicated by the data that the
sample moved after the first set of data was taken. The remain-
ing data for FORSCATB through FORSCATH indicate a very low degree
of scatter at the 5 MHz frequency, as can be seen from the se-
lected statistics given in table 6.

Surface Texture and Post-Curing Test Results

Measurements were made to determine what effect either
polishing the surface of the graphite sample or post-curing the
sample would have on the velocity of sound and attenuation meas-
urements. Initial measurements were made on the top half and
bottom half of a 32-ply ±45° Graphite-Epoxy sample. These meas-
urements are reported in reference 21. The top half of the
sample was then polished on both faces to remove the rough sur-
face which is left when the peelply is removed after curing.
Velocity and attenuation measurements were then made over the
smooth half of the specimen. Comparing values of velocity and
attenuation before and after polishing indicates a very slight
change in velocity and no consistent change in attenuation over
the entire frequency range. The sample was then post-cured at
400°F for eight hours and velocity and attenuation measurements
were made over both the smooth and rough surfaces. The results
show no consistent change in the velocity of sound after post-
curing and only a slight increase in attenuation over the entire
frequency range. Since these results indicated no general change
due to polishing or post-curing, the remaining samples in the
test program were left rough and were not post-cured.

Moisture Conditioning of Neat Resin and Graphite/Epoxy Samples

Neat resin samples which were 2.54 cm. x 0.508 cm. x 22.86
cm. (1 in. x 0.2 in. x 9 in.) and Graphite/Epoxy samples which
were either $[\pm 45_8]_s$ or $[0°]_{32}$ were moisture conditioned by

submersion in water at 90°C. The samples were weighed before and after the four month con   )ning process and the percentage increase in weight due to .   cure absorption was 14.91% for the resin, 2.73% for the ±45° samples and 2.67% for the 0° samples. Ultrasonic velocity and attenuation measurements were made before and after conditioning. The results for a frequency of 5 MHz, which are summarized in tables 7 and 8, indicate no significant change in the velocity of sound for Graphite/Epoxy as well as neat resin materials. The attenuation measurements were made using both frequency and amplitude information and the results indicate significant changes in the attenuation coefficients of all materials. Results in table 8 show that it can be concluded with 95% confidence that moisture content alters the attenuation coefficients. Values for attenuation and velocity at 1 MHz intervals for all the samples before and after moisture conditioning as well as sample plots of these data can be found in reference 21.

In preparation for fatigue testing, static tests were made on the ±45° samples and the neat resin samples. Modulus information was also taken on the neat resin. The dry resin had an average ultimate stress of 30.63 MPa (4442 psi), an average Poisson's ratio of 0.377, and an average Young's modulus of 3.576 GPa (5.187×10^5 psi). The dry ±45° graphite samples were tested for ultimate stress and indicated an average σ_{ult} of 172.9 MPa (25,073 psi) for four samples. After moisture conditioning, both resin and ±45° samples were tested for residual strength. The results for ultimate stress were 19.90 MPa (2886 psi) for the resin and 161.4 MPa (23,415 psi) for the ±45° graphite samples. For the resin samples, all failures were in the center of the test section and figures 37 and 38 show the fractured ends of the dry and moisture conditioned resins.

Moisture conditioning also caused a significant darkening of the color of the resin samples, which is not evident in the photographs. Ultrasonic C-scans were made of statically tested dry and moisture conditioned ±45° samples. The C-scans indicate a

much larger degree of damage outside the failure region for the moisture conditioned samples. These C-scans are shown in figures 39 and 40. The large amount of damage present in the moisture conditioned samples was not present prior to testing.

Fatigue Conditioning of $[\pm 45_8]_s$ Graphite/Epoxy and Neat Resin Samples

Neat resin samples were fatigued at a 50% S-level for 200,000 cycles at a 5 Hz rate. Velocity and attenuation measurements were made at 50,000 cycle intervals and the results indicate no changes in either measurement.

The $[\pm 45_8]_s$ Graphite/Epoxy samples were fatigued at 75%, 65%, and 50% S-levels. The samples tested at 75% S-level failed after an average of 9030 cycles. The samples cycled at S=65% failed after 78,540 cycles and those fatigued at S=50% had not failed after 3,000,000 cycles. Velocity and attenuation measurements were made on the samples before testing and after failure as well as at 10 intervals during testing. Select statistics for measurements made at four locations for all load cycle intervals are summarized in table 9. Results of a regression analysis performed for examining the possibility that some correlation exists between the measured properties and number of load cycles are given in table 10. It appears that no significant correlation can be established. The same conclusion is obtained from the results of a paired "t" test reported in table 11. Ultrasonic C-scans were performed on the samples after testing or failure and are shown in figure 41. The scans indicate no damage outside the failure zones and no damage at all after 3,080,000 cycles at 50% S.

<u>ANALYTICAL/EXPERIMENTAL DATA CORRELATION</u>

DISBONDS IN SHEAR ENVIRONMENT

Strain energy release rates along the periphery of elliptic disbonds of various sizes located at the midsurface of a $[(0_4/\pm45_2/\mp45_2/0_4)_s]_s$ graphite/epoxy laminate were calculated by the use of the methods presented. Elastic properties of the unidirectionally reinforced composite (0° layer) as well as stiffnesses of the $(0_4/\pm45_2/\mp45_2/0_4)_s$ laminate are listed in table 12. Since D_{16} and D_{26} are negligible as compared to D_{11}, D_{12} and D_{22}, bending-twisting coupling were neglected and the two $(0_4/\pm45_2/\mp45_2/0_4)_s$ laminates above and below the disbond were considered orthotropic. Extensional and bending stiffnesses were calculated by the use of laminated plate theory (equations A-1.4) and the shear stiffnesses were computed with the help of equations (A-1.5) and (A-1.6) given in Appendix A-1. Shear correction factors k'_{55} and k'_{44} were taken equal to 0.833.

Retention of four terms (p,m $\leq$ 4 in equation A-2.57) in the Fourier expansions in θ (equations A-2.33, A-2.34 and 3) and four terms (n,n' $\leq$ 4 in equation A-2.57) in the series expansion in r were found to yield good accuracy in obtaining the results. 16 integration points were sufficient for numerical evaluation of the definite integrals with respect to ϕ in equations (A-2.61) and (A-2.62). 32 integration points were found to be enough to yield reasonable accuracy for evaluation of the infinite integrals with respect to ζ in equation (A-2.62).

Figures 42 and 43 show the variation of strain energy release rates G_{II} and G_{III} with θ (along the disbond periphery) for various disbond geometries, due to the application of self-equilibrating uniform shear stress in x-directions on the disbond surfaces. As the dimension of the semi-axis L_1 (in x-direction) is increased keeping the other semi-axis L_2 fixed, values of G_{II} first increase and then start decreasing whereas values of G_{III}

go on increasing. This phenomenon is consistent with what is observed in the three-dimensional elasticity solution of an elliptical crack in an infinite isotropic medium (ref. 22). Change in G_{II} at $x=L_1$, $y=0$ for increasing L_1 with L_2 held constant is more clearly demonstrated in figure 44. Figure 45 shows the variation of G_{II} at $x=L_1$, $y=0$ with L_1/L_2 as L_2 is increased with L_1 fixed. It should be noted that in the limiting case of $L_1/L_2 \to 0$, the problem reduces to that of generalized plane strain. Results from the two-dimensional elasticity solution (ref. 2) for this problem are also shown in figure 45. Although the results for the limiting case cannot be obtained by the methods used in this study, the results in figure 45 indicate that laminated plate theory solution yields values of $\sqrt{G_{II}}$ which are about 7% to 10% lower than the elasticity solution. Similar differences were observed between the elasticity solution (ref. 2) and the strength of materials type solution (ref. 1) as indicated in figure 37 of reference 2.

Experimental data from thick beam specimens tested under quasi-static loading do not indicate any failure due to propagation of disbonds. Therefore it was not possible to make any assessment of critical values of strain energy release rates to cause quasi-static propagation of disbonds. Analytical results indicate that for a disbond of 38.1 mm. diameter, G_{II} at $\theta=0°$ ($x=19.05$ mm., $y=0$) can reach a value of 716 N/m for an applied load of 20,300 Newtons, which is less than the average failure load of 30,740 Newtons. Tests referred to in reference 1 on 25.4 mm. wide beams containing delaminations of the same width but of various lengths, indicated a critical value of G_{II} of 716 N/m (see ref. 2). In the specimens used in the current study, values of G_{II} and G_{III} at points other than at $\theta=0°$ are significantly lower than 716 N/m for the same load of 20,300 Newtons. In fact, G_{II} is a maximum at $\theta=0°$ and reduces to zero at $\theta=\pi/2$ and G_{III} has a maximum value of 189 N/m at $\theta=\pi/2$ and reduces to zero at $\theta=0°$ (see figs. 42 and 43). Therefore, the

load required to cause disbond propagation is likely to be much
higher than the load which caused flexural failure in the speci-
mens. As reported in reference 19, the calculated value of
load to cause failure of the 45° plies is 32,300 Newtons, which
is a little higher than the average experimental value of
30,740 Newtons.

Growths of disbonds under cyclic loading were measured and
are tabulated in reference 19. The results show that the growth
in y-direction at $\theta=\pi/2$ is not at all significant. Growth rates
in x-direction were measured at six points (y=0 and y=±9.53 mm.).
The distance L_1 of the two disbond fronts at y=0 from the center
of each of the two flaws were plotted against the number of
cycles N for each specimen. Representative plots are shown in
figures 46-51. Growth rates $\Delta L_1/\Delta N$ were then computed at various
points along the L_1 vs. N plots. Values of L_1 at these points
were then used to calculate $\Delta(\sqrt{G_{II}})$ by using the analytical meth-
ods outlined in Appendix A-2, with the assumption that the dis-
bond is elliptic with semi-axes L_1 and L_2. Values of dL_1/dN are
plotted against $\Delta(\sqrt{G_{II}})$ in figure 52. Experimental results in-
dicate that the growth rates are extremely small for S=0.4 and
practically no growth occurs up to a million cycles for disbonds
with an initial value of $2L_1 \leq 31.75$ mm. Therefore there appears
to exist a threshold value $\Delta_0(\sqrt{G_{II}})$ of $\Delta(\sqrt{G_{II}})$ below which propa-
gation of disbonds do not occur. The lowest value of $\Delta(\sqrt{G_{II}})$ for
which some growth was observed is of the order of 9.4 $(N/m)^{1/2}$.
Least square fits were therefore attempted to obtain the empiri-
cal constants C_1 and n in relationships of the form:

$$\frac{dL_1}{dN} = C_1\{\Delta(\sqrt{G_{II}}) - \Delta_0(\sqrt{G_{II}})\}^n \tag{9}$$

-25-

with a series of values of $\Delta_0(\sqrt{G_{II}})$ varying from 0 to 9 $(N/m)^{1/2}$.
The parameters for two curves which appear to give the closest
fit to the data are given below in Newton, meter units.

$\Delta_0(\sqrt{G_{II}})$, $(N/m)^{1/2}$	C_1 (N,m units)	n
7.0	0.678×10^{-9}	2.979
8.0	2.565×10^{-9}	2.518

The curve corresponding to the first set of parameters is
also shown in figure 52. The curve corresponding to the second
set practically coincides with the first in the range of $\Delta(\sqrt{G_{II}})$
shown in the figure. It should be noted that the growth law
given by equation (9) with the parameters given above is likely
to be applicable under generalized plane strain conditions.
Curve fits attempted in reference 2, which is appropriate under
generalized plane stress conditions, yielded a value of
$C_1 = 1.382 \times 10^{-9}$ and n = 2.776 with the threshold value
$\Delta_0(\sqrt{G_{II}})$ equal to zero. These values of C_1 and n lie between
the values given in the table above. For plane stress condi-
tions effects of free edges are likely to cause the flaws to
start growing under much smaller values of $\Delta(\sqrt{G_{II}})$. Therefore,
the values obtained in this study appear to be consistent with
those obtained in reference 2.

BUCKLING OF DISBONDED COMPRESSION SKIN

Properties of the laminates and the honeycomb are given in
table 13. For compression skins with defects in the midsurface
there is no extension-bending coupling and twisting-bending
coupling is not too large. Therefore, the two $(0/\pm 45/\mp 45/0)$
laminates can be considered to be orthotropic. For compression

-26-

skins with defects near surface (three plies below exposed sur-
face) there exist some amounts of bending-extension as well as
bending-twisting coupling. For the present study, however, all
such coupling effects were neglected to reduce the computer time
needed for calculation of critical loads by iterative methods.
Since the lowest value of critical load was to be determined,
two terms in the Fourier expansion θ (p,m $\leq$ 2) and two terms in
the series expansion in r (n,n' $\leq$ 2) were retained in the infin-
ite system of equations (5). 12 integration points were suffi-
cient for numerical evaluation of the definite integrals with
respect to ϕ in equations (A-2.61) and (A-2.62). For disbond
sizes not too large compared to the thickness of laminate 1, 32
integration points were found to yield reasonable accuracy for
evaluation of the infinite integrals with respect to ζ in equa-
tion (A-2.62). For larger disbond sizes use of 64 integration
points were necessary.

Figure 53 shows the variation of average compressive stress
in the skin required to cause buckling with flaw size and shape.
The pattern is similar to that of Euler type buckling. The cut-
off for small flaw sizes is set at experimental values of the
average compressive stress to cause failure without any defect.

Calculated values of critical stress for the specimens test-
ed are compared with experimental values of buckling and/or
failure stress in table 14. In general, the experimental values
are comparitively much higher than the calculated critical
stress. The reason for this discrepancy appears to be the fact
that under applied load the sandwich beams have certain curvature
which increases with load, but the portion of the laminate above
the disbond cannot have a buckled shape with curvature in the
same direction, because of constraints imposed on it. The buckled
shape has to have a curvature in the opposite direction. Studies
on buckling of initially curved bars under lateral loads (ref. 23)
show that loads to cause buckling increase rapidly with increas-
ing values of initial deformation and sudden reversal of

-27-

deflection occurs at the critical load. Sudden catastrophic failure of most of the sandwich beam specimens indicates similar behavior. It may be noted that only one of the specimens tested (specimen No. 3 with 38.1 mm. dia. near surface defect) showed a gradual change in the deflection pattern, and the experimental value of average compressive stress to cause strain reversal is lower than the calculated critical stress for this specimen. A detailed study of the phenomenon of deflection reversal in the types of specimens tested is beyond the scope of the present work but should be considered in future studies, since the simple Euler type buckling assumption underestimates the residual strength of sandwich beams tested under four-point bending.

DISCUSSIONS AND CONCLUSIONS

In the present study a NDE methodology for assessing critical-
ity of disbond type defects with nearly elliptic two-dimensional
planform has been developed and its usefulness has been examined.
In addition, effects of moisture conditioning and cyclic loading
on ultrasonic wave velocities and attenuation have been studied.
The following conclusions and comments can be made based on the
results obtained.

1. Linear elastic fracture mechanics approach and methods of
   stress analysis based on a modified laminated plate
   theory yield reasonably accurate values of strain energy
   release rates along the periphery of a disbond in a lam-
   inated composite subjected to transverse shear. Based on
   these calculated values of strain energy release rates
   and semi-empirical crack growth laws, growth of such dis-
   bonds under cyclic shear can be predicted. A growth law
   for dominant mode II behavior under generalized plane
   strain conditions has been obtained which appears to be
   consistent with such a law determined in reference 2 for
   generalized plane stress conditions. Further studies are
   needed for obtaining growth laws under combined actions
   of mode II and mode III behavior. Experimental results
   indicate that for the types of specimens tested mode II
   behavior dominates the growth of the disbonds. By the
   use of these laws and appropriate failure models, an
   assessment of residual strength and/or residual lifetime
   can be made.

2. Presence of disbonds can significantly lower the load
   carrying capacity of a laminated composite under compres-
   sion. A linearized elastic stability analysis can be
   used to assess criticality of disbonds with nearly ellip-
   tic planforms, but the analytical predictions appear to
   underestimate the failure loads of sandwich beams with

delaminated compression skins tested in four-point bending, where reversal of deflection has to occur before buckling and/or failure. These results and catastrophic failures of a majority of sandwich beams tested suggest the need for further studies on effects of deflection reversal on such failures. The possibility of alternative test plans to eliminate such effects should also be examined in future studies.

3. Moisture conditioning of Graphite/Epoxy composites has some effect on the attenuation of sound in the material, but appears to have little or no effect on the velocity of sound. Damages induced by moisture conditioning are distributed throughout the specimens. Damages caused by cyclic loading, however, are highly localized near the failure sites. Cyclic loading appears to cause no significant changes in velocity of sound and attenuation prior to as well as after failure of Graphite/Epoxy specimens. The same conclusion holds for neat resin samples tested.

REFERENCES

1. Ramkumar, R. L., Kulkarni, S. V., and Pipes, R. B.,
   "Definition and Modeling of Critical Flaws in Graphite
   Fiber Reinforced Composites," NADC 76228-30, Final Report,
   January 1978.

2. Chatterjee, S. N., Hashin, Z., and Pipes, R. B.,
   "Definition and Modeling of Critical Flaws in Graphite
   Fiber Reinforced Composites," NADC 77278-30, Final Report,
   August 1979.

3. Ratwani, M. M., and Kan, H. P., "Compression Fatigue
   Analysis of Fiber Composites," NADC 78049-60, Final Report,
   September 1979.

4. Chatterjee, S. N., "On Interlaminar Defects in a Laminated
   Composite," in Modern Developments in Composite Materials
   and Structures, ASME, New York, December 1979, p. 1.

5. Willis, J. R., Int. J. Eng'g. Sci., Vol. 6, 1968, p. 253.

6. Sekine, H., and Mura, T., Int. J. Eng'g. Sci., Vol. 17,
   1979, p. 641.

7. Whitney, J. M., and Pagano, N. J., Journal of Applied
   Mechanics, Vol. 37, 1970, p. 1031.

8. Hellan, K., Int. J. of Fracture, Vol. 14, 1978, p. 91.

9. Williams, M. L., Bull. of Seismological Soc. of America,
   Vol. 49, 1949, p. 199.

10. Malyshev, B. M., and Salagnik, R. L., Int. J. of Fracture
    Mechanics, Vol. 1, 1965, p. 119.

11. Rice, J. R., and Sih, G. C., Journal of Applied Mechanics,
    Vol. 32, Series E., No. 2, June 1965.

12. Williams, M. L., "Stress Singularities, Adhesion and
    Fracture," in Proc. Fifth U.S. Nat'l. Cong. of Applied
    Mechanics, 1966, p. 451.

13. Benett, S. J., Devries, K. L., and Williams, M. L.,
    Int. J. of Fracture, Vol. 10, 1974, p. 33.

14. Kendall, K., Int. J. of Fracture, Vol. 11, 1975, p. 3.

15. Williams, M. L., J. of Adhesion, Vol. 4, 1972.

REFERENCES (Continued)

16. Kulkarni, S. V., and Frederick, D., Int. J. of Fracture, Vol. 9, 1973.

17. Updike, D. P., Int. J. of Fracture, Vol. 12, 1976, p. 815.

18. Ramkumar, R. L., Kulkarni, S. V., Pipes, R. B., and Chatterjee, S. N., "Analytic Modeling and ND Monitoring of Interlaminar Defects in Fiber Reinforced Composites," in Fracture Mechanics, ASTM STP 677, June 1978, p. 668.

19. Dimondi, V., "Interlaminar Flaw Propagation, Mode II," Center for Composite Materials, University of Delaware, Newark, Delaware, CCM 80-18, September 1980.

20. Blake, R. A., Jr., "Interlaminar Defect Criticality in Graphite/Epoxy Sandwich Beam Composites," Center for Composite Materials, University of Delaware, Newark, Delaware, CCM 80-19, September 1980.

21. Blake, R. A. Jr., "Measurement of Ultrasonic Material Property Degradation Due to Moisture Conditioning or Fatigue Loading," Center for Composite Materials, University of Delaware, Newark, Delaware, CCM 80-20, September 1980.

22. Sih, G. C., and Liebowitz, H., "Mathematical Theories of Brittle Fracture," in Fracture Vol. II, H. Liebowitz, ed., Academic Press, 1968.

23. Timoshenko, S. P., and Gere, J. M., Theory of Elastic Stability, McGraw-Hill Book Company, 1961.

24. Chatterjee, S. N., and Kulkarni, S. V., AIAA Journal, Vol. 17, 1979, p. 498.

25. Chou, P. C., and Carleone, J., AIAA Journal, Vol. 11, 1973, p. 1333.

26. Gradshteyn, I. S., and Ryzhik, I. M., Table of Integrals Series and Products, Academic Press, 1965.

Table 1. Laminated Beam Static Test Results

$$([0_4/\pm45_2/\mp45_2/0_4]_s)_s$$

Width=76.2 mm., Thickness=9.7 mm.

Specimen Number	Defect Size (mm./in.)	Failure Load (N/lbs.)
1-1	25.4/1.0	25,310/5,690
1-2	25.4/1.0	29,360/6,600
1-11	25.4/1.0	36,740/8,260
1-13	25.4/1.0	30,380/6,830
1.25-1	31.8/1.25	34,790/7,820
1.25-2	31.8/1.25	32,300/7,260
1.5-2	38.1/1.5	30,380/6,830
1.5-4*	38.1/1.5	26,690/6,000
Average		30,740/6,920

*Note: Failed in Interlaminar Shear

Table 2. Thick Beam Specimens Tested in Fatigue

Specimen No. $[[0_4/45_2/45_2/0_4]_s]_s$	Defect Size/Shape/Location (in.) (in.)	S-Level	Total Cycles Tested
1-17	1.0/C/1.5	.4	< 625,000
1-18	1.0/C/1.5	.4	<1,075,000
1.25-5	1.25/O/1.5	.4	<1,000,000
	1.25/O/1.5	.4	< 725,000
1.5-5	1.5/O/1.5	.4	135,000
1.5-6	1.5/O/1.5	.4	115,000
1-14	1.0/C/1.5	.5	180,000
1-15	1.0/C/1.5	.5	130,000
1.25-3	1.25/O/1.5	.5	50,000
1.25-4	1.25/O/1.5	.5	100,000
1.5-1	1.5/O/1.5	.5	27,500
1.5-3	1.5/O/1.5	.5	25,000
1-19	1.0/C/1.5	.6	32,000
1-20	1.0/C/1.5	.6	12,170
1.25-7	1.25/O/1.5	.6	11,500
1.25-8	1.25/O/1.5	.6	11,000
1.5-7	1.5/O/1.5	.6	13,000
1.5-8	1.5/O/1.5	.6	16,000
1.25C-1	1.25/C/1.5	.5	60,000
1.25C-2	1.25/C/1.5	.5	33,500
1.5C-1	1.5/C/1.5	.5	10,000
1.5C-2	1.5/C/1.5	.5	22,000
1.25C-3	1.25/C/1.5	.6	6,870
1.25C-4	1.25/C/1.5	.6	15,000

Table 2 (continued). Thick Beam Specimens Tested in Fatigue

Specimen No. $[[0_4/\pm45_2/\pm45_2/0_4]_s]_s$	Defect Size/Shape/Location (in.) (in.)	S-Level	Total Cycles Tested
1.5C-3	1.5/C/1.5	.6	8,880
1.5C-4	1.5/C/1.5	.6	4,150
1.0C2-1	1.0/C/2.0	.5	700,000
1.0C2-2	1.0/C/2.0	.5	328,700
1.25C2-1	1.25/C/2.0	.5	118,000
1.25C2-2	1.25/C/2.0	.5	56,000
1.5C2-1	1.5/C/2.0	.5	19,840
1.5C2-2	1.5/C/2.0	.5	6,750
1.0C2-3	1.0/O/2.0	.6	65,650
1.0C2-4	1.0/O/2.0	.6	117,910
1.25C2-3	1.25/C/2.0	.6	12,580
1.25C2-4	1.25/C/2.0	.6	47,090

Table 3. Specimen Fabrication Requirements for
Sandwich Beam Defect Criticality Study

Defect Size	Defect Location	Number of Samples
No defect	---	3
1.0-in. Circular	Near surface*	3
1.5-in. Circular	Near surface*	3
1.5-in. Circular	Midply	3
2.0-in. Circular	Midply	3
2.0-in. 2.5-in. Oblong	Midply	3
1.5-in. Circular	Midply-both faces	1

TOTAL: 19

*Near surface defects are located three plies below the
exposed surface.

Table 4. Sandwich Beam Failure Test Data

Defect Size	Defect Location	Maximum Load (kg)	Maximum ε_T 10^{-6}	Maximum ε_C 10^{-6}
No defect	--	2925	5100	15125
No defect	--	3425	5775	18100
No defect	--	3300	5850	15200
1 in. cir.	Near	2950	--	
1 in. cir.	Near	2750	--	
1 in. cir.	Near	2800	--	
1.5 in. cir.	Near	2900	--	Buckled
1.5 in. cir.	Near	2730	--	
1.5 in. cir.	Near	2810	--	
1.5 in. cir.	Mid	2210	3750	9150
1.5 in. cir.	Mid	2715	4325	11300
1.5 in. cir.	Mid	1325	2150	5425
2 in. cir.	Mid	2275	3925	9850
2 in. cir.	Mid	2050	3450	8700
2 in. cir.	Mid	2500	4225	10500
2 in.x2.5 in.	Mid	2350	3800	11725
2 in.x2.5 in.	Mid	2435	4025	11000
2 in.x2.5 in.	Mid	1960	3450	8425

Table 5. Sandwich Beam Buckling Test Data

Defect Size	Defect Location	Buckling Load (kg)	Buckling ε_T 10^{-6}	Buckling ε_C 10^{-6}
1 in. cir.	Near	1695	2820	6550
1 in. cir.	Near	1280	2350	5200
1 in. cir.	Near	140J	1770	4100
1.5 in. cir.	Near	635	1075	2350
1.5 in. cir.	Near	775	1330	2900
1.5 in. cir.	Near	200*	340	105

*Appeared to have a deformed shape

Table 6. Select Statistics for Ultrasonic
Property Measurement

<u>5 MHz</u>

Location	Mean $\overline{x}$	Standard Deviation σ	Variance σ^2	Average Deviation $\Sigma|x-\overline{x}|/n$
<u>Velocity</u> (m./sec.)				
BCD	3027.72	0.4359	0.1267	0.720
EFGH	3028.27	2.053	4.2158	1.635
<u>Attenuation</u> (mm.$^{-1}$)				
BCD	0.0936	0.0043	$1.25\times10^{-?}$	0.0022
EFGH	0.0935	0.0069	3.58×10^{-5}	0.0049

Table 7. Select Statistics for Moisture Conditioning Results

	Mean $\overline{x}$	Standard Deviation σ_{n-1}	Variance σ^2	Average Deviation $\Sigma |x-\overline{x}|/n$
±45° Graphite				
Velocity (m./sec.)				
Dry	3292.7	54.13	2511.9	37.01
Moist	3192.9	80.52	5557.3	62.13
Amp Atten (mm.$^{-1}$)				
Dry	.06139	.01142	.00011	.00898
Moist	.09503	.01076	.00010	.00817
Freq Atten (mm.$^{-1}$)				
Dry	.06897	.00949	.00008	.00682
Moist	.11998	.02670	.00061	.02118
0° Graphite				
Velocity (m./sec.)				
Dry	3213.4	106.8	9120.2	77.68
Moist	3244.2	87.1	6065.8	70.24
Amp Atten (mm.$^{-1}$)				
Dry	.06244	.00859	.00006	.00751
Moist	.09812	.00749	.00004	.00586
Freq Atten (mm.$^{-1}$)				
Dry	.07412	.01841	.00027	.01602
Moist	.12262	.01945	.00030	.01366
Neat Resin				
Velocity (m./sec.)				
Dry	2921.7	50.36	2173.6	35.13
Moist	2869.4	35.93	1106.5	28.60
Amp Atten (mm.$^{-1}$)				
Dry	.12844	.00529	.00002	.00397
Moist	.17773	.00337	.00001	.00258
Freq Atten (mm.$^{-1}$)				
Dry	.12341	.00774	.00005	.00567
Moist	.18567	.01585	.00021	.01420

Table 8. Paired "t" Test for Moisture Conditioning Results

	Sample Mean $\bar{x}$	"Dry" Mean $\bar{x}_D$	"Moist" Mean $\bar{x}_M$	Sample Standard Deviation σ	n_D	n_M	n	Est. Pop. Standard Deviation $s_{\bar{x}_D - \bar{x}_M}$	DOF	t_{obs}	t_{crit} 95%
±45° Graphite											
Velocity (m./sec.)	3242.7	3292.7	3192.9	93.84	7	7	14	44.81	12	2.227	2.179
Ampl. Att. (mm.$^{-1}$)	.07821	.06139	.09503	.0205	7	7	14	.01096	12	3.069	2.179
Freq. Att. (mm.$^{-1}$)	.09448	.06897	.11998	.0327	7	7	14	.01748	12	2.918	2.179
0° Graphite											
Velocity (m./sec.)	3228.8	3213.4	3244.2	93.27	5	5	10	58.99	8	0.522	2.306
Ampl. Att. (mm.$^{-1}$)	.08028	.06244	.09812	.0203	5	5	10	.01284	8	2.779	2.306
Freq. Att. (mm.$^{-1}$)	.09873	.07412	.12262	.0310	5	5	10	.01961	8	3.777	2.306
Neat Resin											
Velocity (m./sec.)	2895.6	2921.7	2869.4	50.02	7	7	14	26.74	12	1.956	2.179
Ampl. Att. (mm.$^{-1}$)	.15309	.12844	.17773	.0259	7	7	14	.01384	12	3.561	2.179
Freq. Att. (mm.$^{-1}$)	.15454	.12341	.13567	.0345	7	7	14	.01344	12	3.338	2.179

Table 9. Select Statistics for ±45° Fatigue Results

Position	Mean $\overline{x}$	Standard Deviation σ_{n-1}	Variance σ^2	Average Deviation $\Sigma\|x-\overline{x}\|/n$
	Velocity (m./sec.)			
1	3202.8	82.45	6042.5	63.26
4	3234.2	116.58	12231.8	89.44
5	3318.1	120.29	13022.3	82.14
6	3286.2	95.88	8273.8	69.40
	Attenuation ($mm.^{-1}$)			
1	.07366	.01110	.00011	.00840
4	.05242	.03633	.00117	.02425
5	.09871	.01593	.00023	.01804
6	.07870	.03835	.00132	.02512

Table 10. Regression Analysis of ±45° Fatigue Results*

Position	Mean $\bar{x}$	Standard Deviation σ	Slope m	Intercept b	Corr Coef r	n	Confidence Level on "r"
Velocity (m./sec.)							
1	3202.89	82.45	-0.0247	3223.6	0.324	9	62%
4	3234.20	116.57	-0.0657	3286.1	0.583	10	92%
5	3316.10	120.26	-0.0606	3365.5	0.515	10	87%
6	3286.20	95.88	-0.0407	3318.3	0.439	10	80%
Attenuation (mm.$^{-1}$)							
1	0.0736	0.0111	1.8×10^{-6}	0.0722	0.166	10	38%
4	0.0524	0.0363	25.7×10^{-6}	0.0303	0.760	9	98%
5	0.0987	0.0159	8.7×10^{-6}	0.0911	0.581	9	90%
6	0.0787	0.0383	-1.9×10^{-6}	0.0800	0.051	10	<20%

* $E(x|C) = b + mC$, C in 10^3 Cycles

Table 11. Paired "t" Test for ±45° Fatigue Results

Position	Sample Mean $\bar{x}$ 0 - 350* $\bar{x}_1$	1420 - 3080* $\bar{x}_2$	Sample Standard Deviation σ	n_1	n_2	n	Est. Pop. Standard Deviation $S_{\bar{x}_1-\bar{x}_2}$	DOF	t_{obs}	t_{crit} 95%
Velocity (m./sec.)										
1	3202.8	3149.7	82.45	6	3	9	58.30	7	1.369	2.365
4	3234.2	3105.7	116.58	7	3	10	80.45	8	1.575	2.306
5	3318.1	3283.3	120.29	7	3	10	83.01	8	0.599	2.306
6	3286.2	3216.0	95.88	7	3	10	66.16	8	1.516	2.306
Attenuation (mm.$^{-1}$)										
1	.07366	.07633	.01110	7	3	10	.00766	8	0.4986	2.306
4	.05242	.07680	.03633	6	3	9	.02569	7	1.4235	2.365
5	.09871	.11427	.01593	6	3	9	.01126	7	2.0728	2.365
6	.07870	.07363	.03835	7	3	10	.02646	8	0.2736	2.306

* Thousands of Cycles

-44-

Table 12.   Elastic Properties of 0° Layer and
Stiffnesses of $(0_4/\pm45_2/\mp45_2/0_4)_s$
Laminate

Transversely Isotropic 0° Layer

E_A = 125 GPa

E_T = 10 GPa

ν_A = 0.28

G_A = 5.8 GPa

$(0_4/\pm45_2/\mp45_2/0_4)_s$ Laminate

A_{11} = 4.06 x 10^8 N/m. D_{11} = 877 Nm.

A_{12} = 0.79 x 10^8 N/m. D_{12} = 131 Nm.

A_{22} = 1.24 x 10^8 N/m. D_{22} = 218 Nm.

A_{66} = 0.95 x 10^8 N/m. D_{66} = 160 Nm.

$A_{16} = A_{26}$ = 0.0 $D_{16} = D_{26}$ = 3.25 Nm.

$B_{\alpha\beta}$ = 0.0 $(\alpha,\beta = 1,2,6)$

K_{55} = 2.12 x 10^7 N/m. K_{44} = 1.75 x 10^7 N/m.

Ply Thickness = 0.1519 mm.

Table 13. Stiffnesses of the Laminates Comprising
the Compression Skin and Properties of
the Core in Sandwich Beams

(0/±45/∓45/0) Laminate, Ply Thickness = 0.1354 mm.

A_{11} = 5.64 x 10^7 N/m. B_{11} = 0 D_{11} = 4.51 N.m.

A_{12} = 1.68 x 10^7 N/m. B_{12} = 0 D_{12} = 0.48 N.m.

A_{22} = 2.50 x 10^7 N/m. B_{22} = 0 D_{22} = 0.86 N.m.

A_{66} = 1.92 x 10^7 N/m. B_{66} = 0 D_{66} = 0.62 N.m.

A_{16} = 0 B_{16} = 0 D_{16} = 0.29 N.m.

A_{26} = 0 B_{26} = 0 D_{26} = 0.29 N.m.

K_{55} = 0.34 x 10^7 N/m. K_{45} = 0 K_{44} = 0.30 x 10^7 N/m.

(0/±45) Laminate, Ply Thickness = 0.1354 mm.

A_{11} = 2.82 x 10^7 N/m. B_{11} = -1.55 x 10^3 N D_{11} = 0.46 N.m.

A_{12} = 0.84 x 10^7 N/m. B_{12} = 0.49 x 10^3 N D_{12} = 0.093 N.m.

A_{22} = 1.25 x 10^7 N/m. B_{22} = 0.57 x 10^3 N D_{22} = 0.15 N.m.

A_{66} = 0.96 x 10^7 N/m. B_{66} = 0.98 x 10^3 N D_{66} = 0.11 N.m.

A_{16} = 0 B_{16} = -0.53 x 10^3 N D_{16} = -0.072 N.m.

A_{26} = 0 B_{26} = -0.53 x 10^3 N D_{26} = -0.072 N.m.

K_{55} = 0.17 x 10^7 N/m. K_{45} = 0 K_{44} = 0.15 x 10^7 N/m.

Table 13 (continued). Stiffnesses of the Laminates Comprising the Compression Skin and Properties of the Core in Sandwich Beams

$(\overline{\mp}45/0/\pm45/\overline{\mp}45/0)$ Laminate, Ply Thickness = 0.1354 mm.

$A_{11} = 8.46 \times 10^7$ N/m. $B_{11} = 1.55 \times 10^3$ N $D_{11} = 10.69$ N.m.

$A_{12} = 2.52 \times 10^7$ N/m. $B_{12} = -0.49 \times 10^3$ N $D_{12} = 3.05$ N.m.

$A_{22} = 3.75 \times 10^7$ N/m. $B_{22} = -0.57 \times 10^3$ N $D_{22} = 4.58$ N.m.

$A_{66} = 2.88 \times 10^7$ N/m. $B_{66} = -0.98 \times 10^3$ N $D_{66} = 3.50$ N.m.

$A_{16} = 0$ $B_{16} = 0.53 \times 10^3$ N $D_{16} = -0.22$ N.m.

$A_{26} = 0$ $B_{26} = 0.53 \times 10^3$ N $D_{26} = -0.22$ N.m.

$K_{55} = 0.51 \times 10^7$ N/m. $K_{45} = 0$ $K_{44} = 0.45 \times 10^7$ N/m.

Core Properties

Thickness = 38.17 mm.

Young's Modulus = 5.17 GPa

Shear Modulus (L) = 2.55 GPa

Shear Modulus (W) = 0.62 GPa

Subgrade Modulus in x-Direction = 66.8 GN/m^3

Subgrade Modulus in y-Direction = 16.3 GN/m^3

Subgrade Modulus in z-Direction = 135.5 GN/m^3

Table 14. Comparison of Sandwich Beam Test Data With
Calculated Values of Critical Stress

Defect Size mm.	Location	Calculated Critical Stress MPa	Average Compressive Stress at Buckling MPa	Average Compressive Stress at Failure MPa
No Defect	--	--	--	590
No Defect	--	--	--	690
No Defect	--	--	--	660
25.4 mm. Circle	Near Surface	130	340	600
25.4 mm. Circle	Near Surface		260	560
25.4 mm. Circle	Near Surface		280	570
38.1 mm. Circle	Near Surface	60	130	580
38.1 mm. Circle	Near Surface		160	550
38.1 mm. Circle	Near Surface		40	570
38.1 mm. Circle	Mid-Ply	210	--	450
38.1 mm. Circle	Mid-Ply		--	550
38.1 mm. Circle	Mid-Ply		--	270
50.8 mm. Circle	Mid-Ply	120	--	460
50.8 mm. Circle	Mid-Ply		--	410
50.8 mm. Circle	Mid-Ply		--	510
50.8 mm. x 63.5 mm.	Mid-Ply	100	--	480
50.8 mm. x 63.5 mm.	Mid-Ply		--	490
50.8 mm. x 63.5 mm.	Mid-Ply		--	400
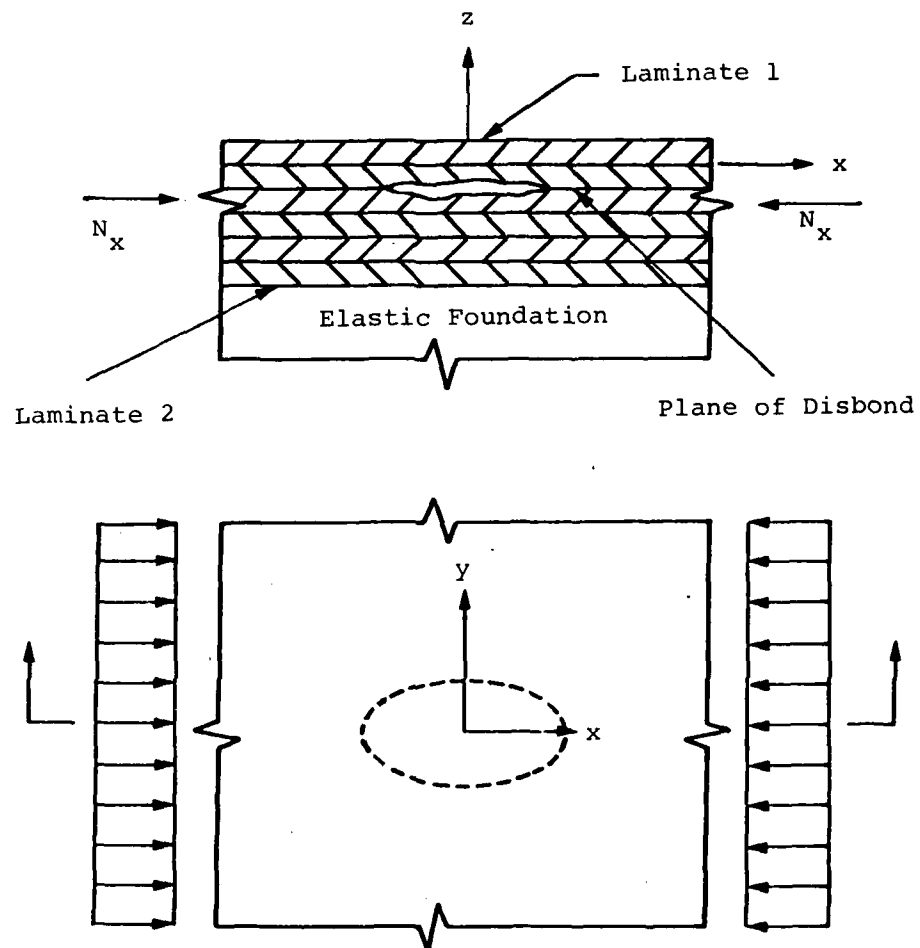
Figure 1. Disbonded Laminate
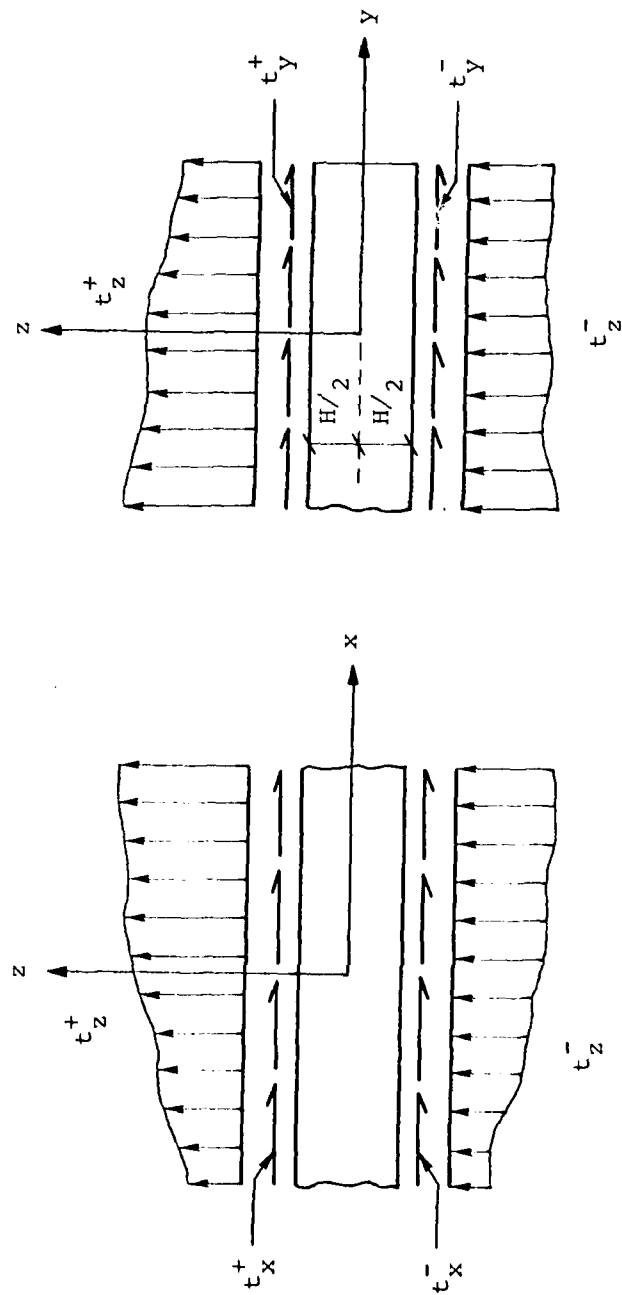
Figure 2. Surface Tractions on a Laminated Plate
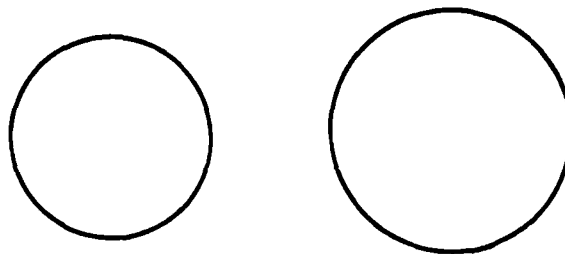
1.25" dia. circular   1.5" dia. circular

.5"r
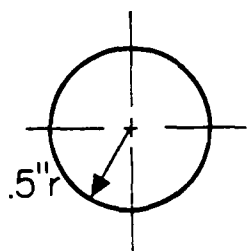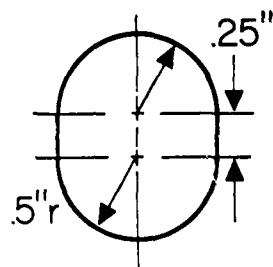
1.0" dia. circular   1.25"x1.0" elongated   1.5"x1.0" elongated
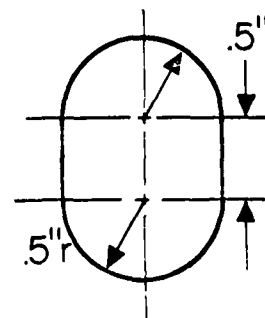
Figure 3.   Disbond Geometries
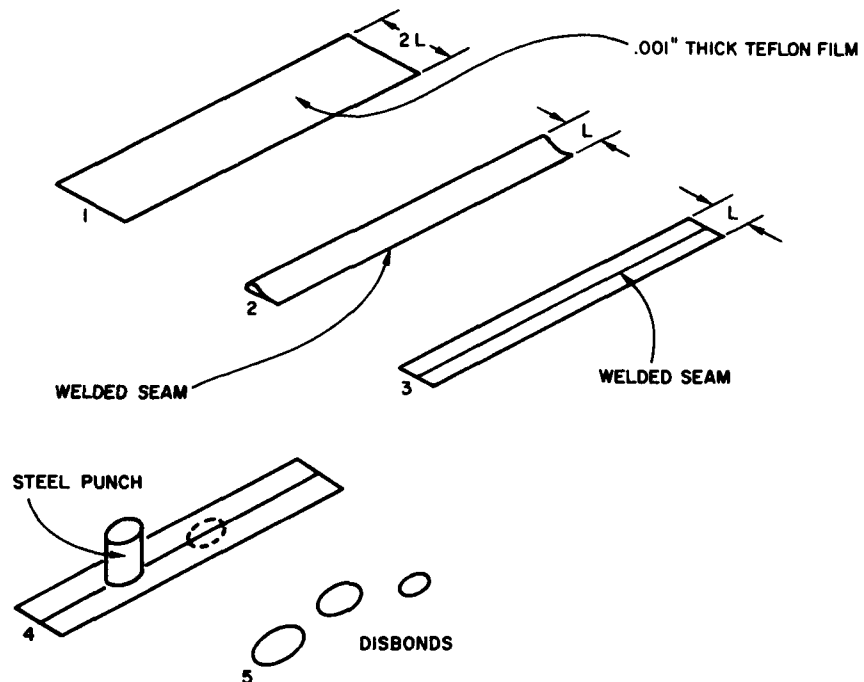
Figure 4. Disbond Fabrication Method
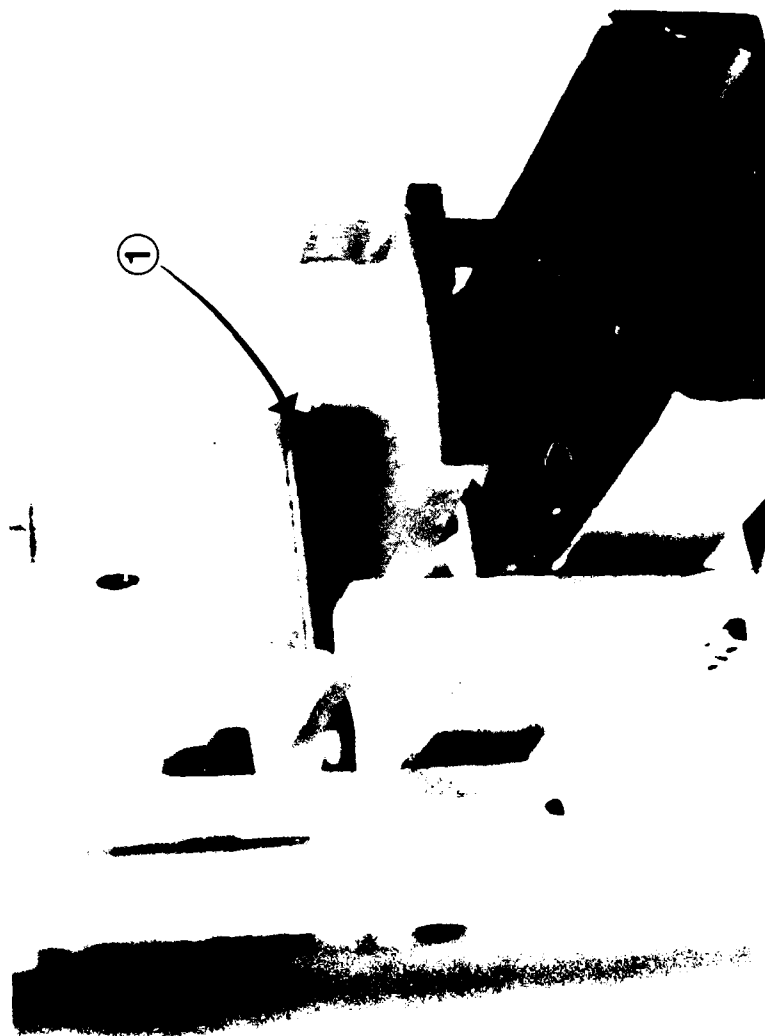
Figure 5. Test Fixture
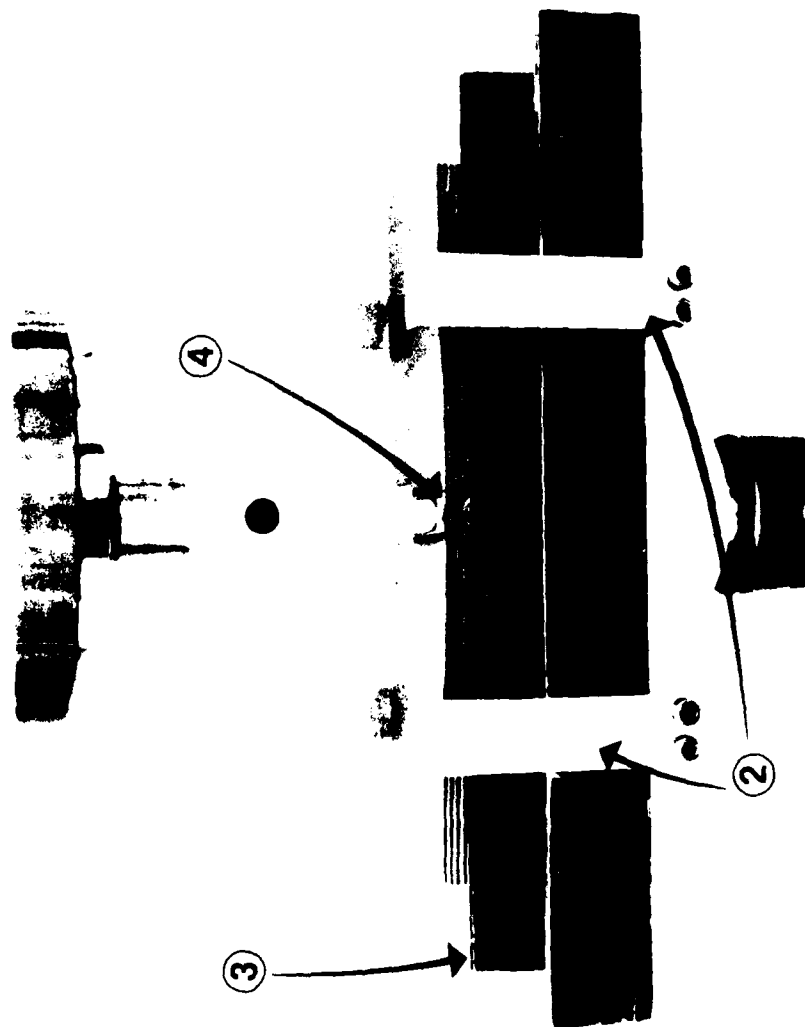
Figure 6. Test Fixture Components

-54-
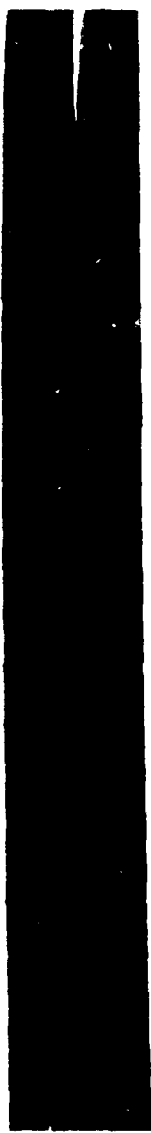
Figure 7. Static Interlaminar Shear Failure (End View)

S=0.5   SPECIMEN 1.0C2-2

40,000   130,000   220,000   265,000

290,000   310,000   325,000   328,700
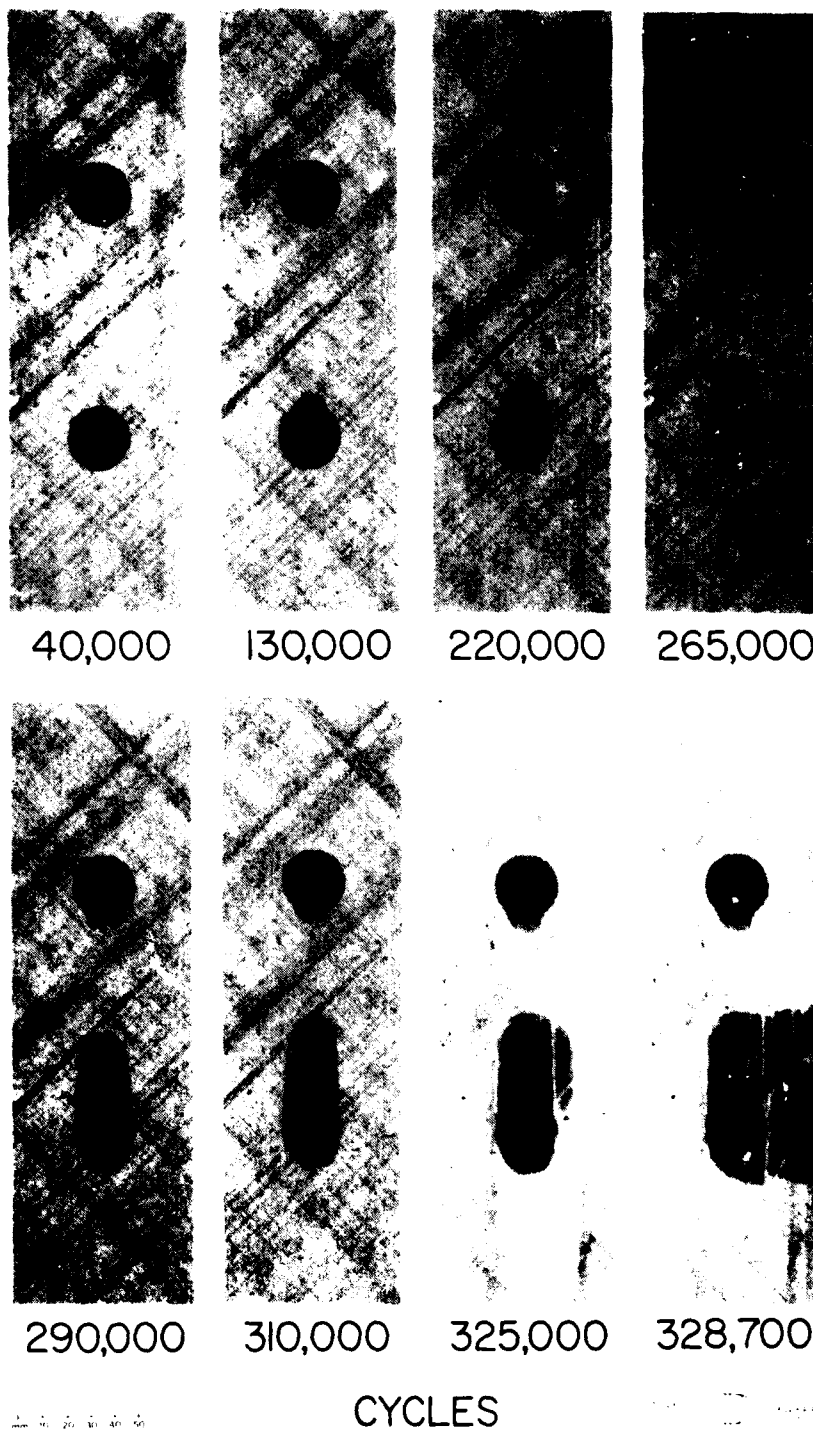
CYCLES

Figure 8.   C-Scan of Specimen 1.0C2-2, S=0.5

S=0.5   SPECIMEN 1.25C2-1

15,000   30,000   51,000   65,000

85,000   98,000   110,000   118,000
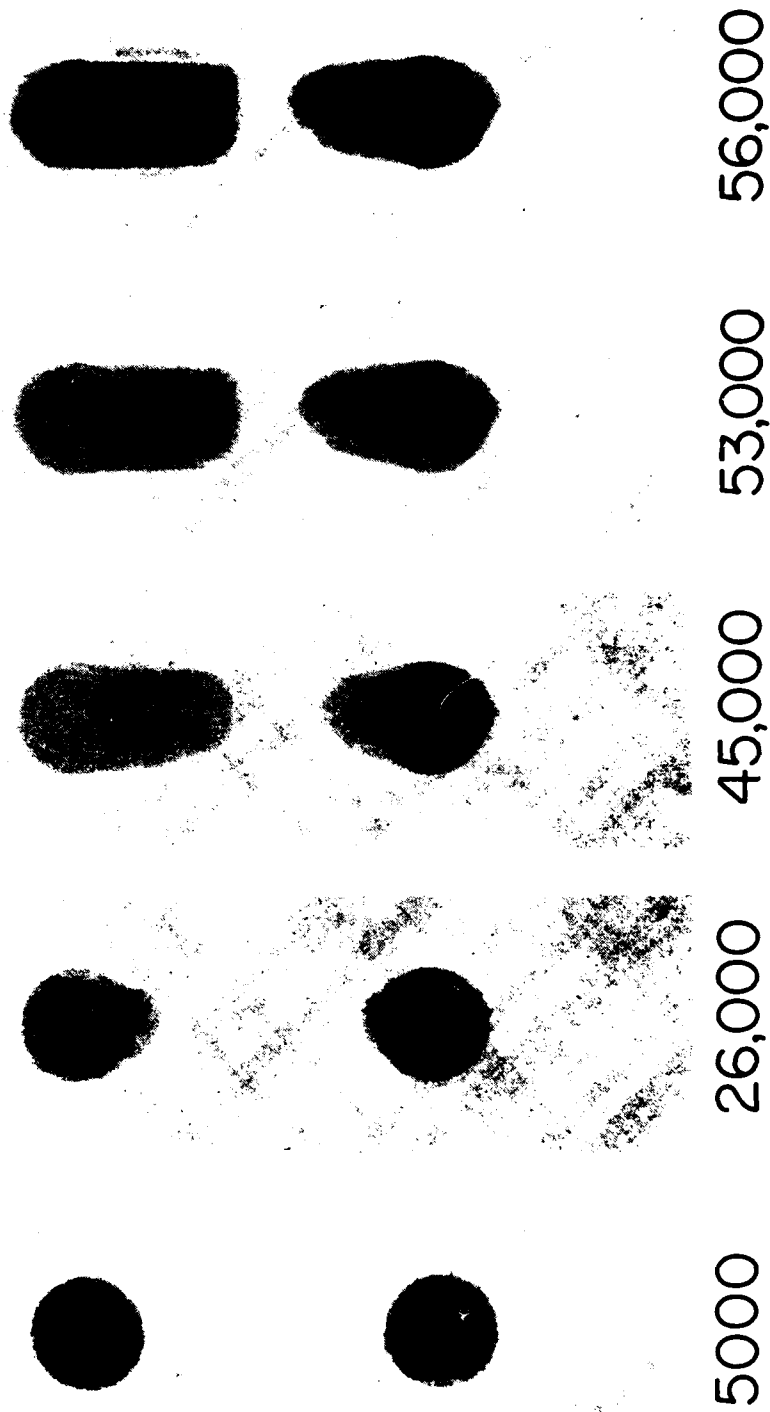
mm 10 20 30 40 50   CYCLES   UNIVERSITY OF DELAWARE

Figure 9.   C-Scan of Specimen 1.25C2-1, S=0.5

-57-

Figure 10. C-Scan of Specimen 1.25C2-2, S=0.5

S=0.5   SPECIMEN 1.5C-1

3000   4000   5000   6000

7000   8000   9000   10,000
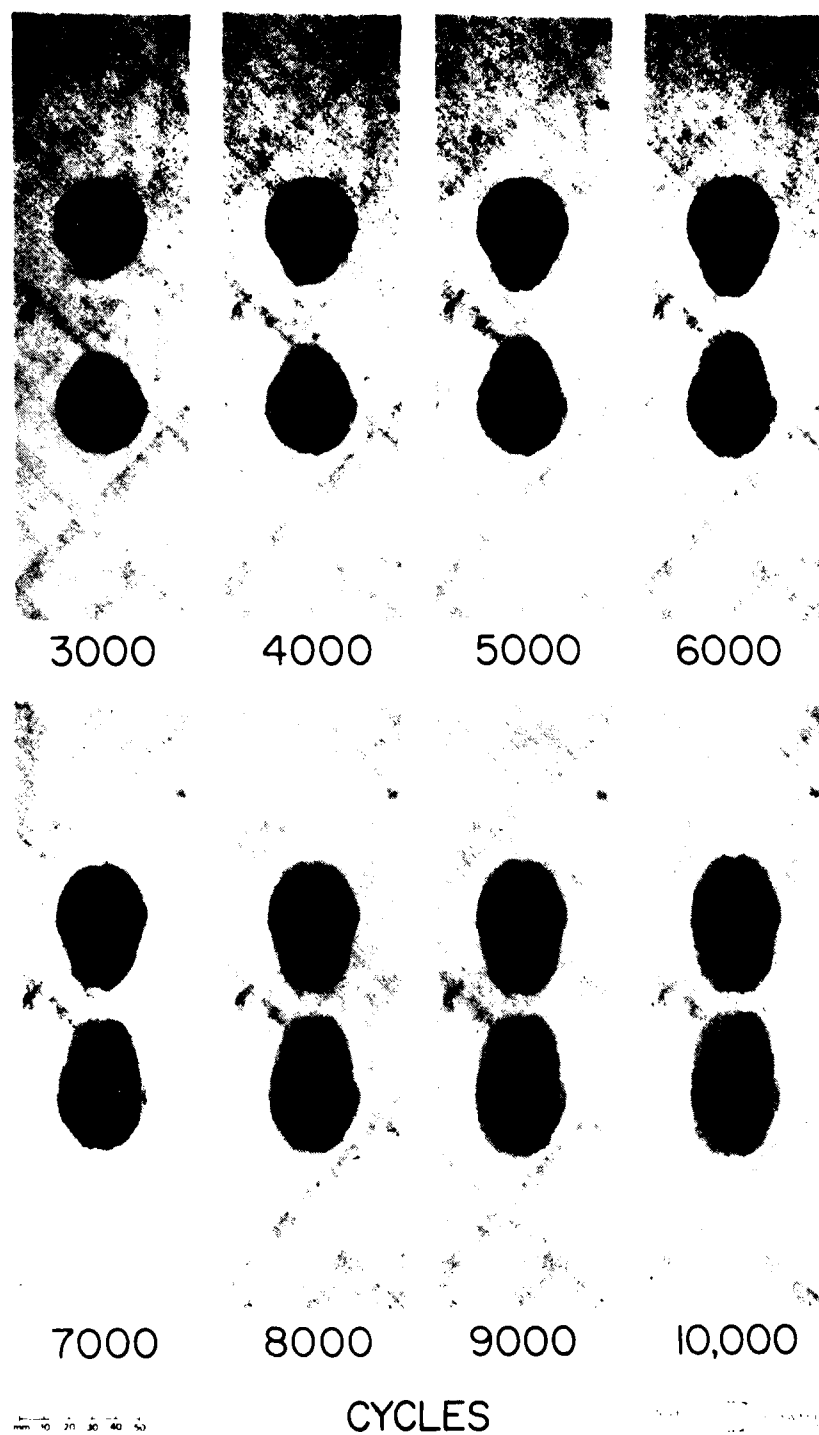
CYCLES

Figure 11. C-Scan of Specimen 1.5C-1, S=0.5
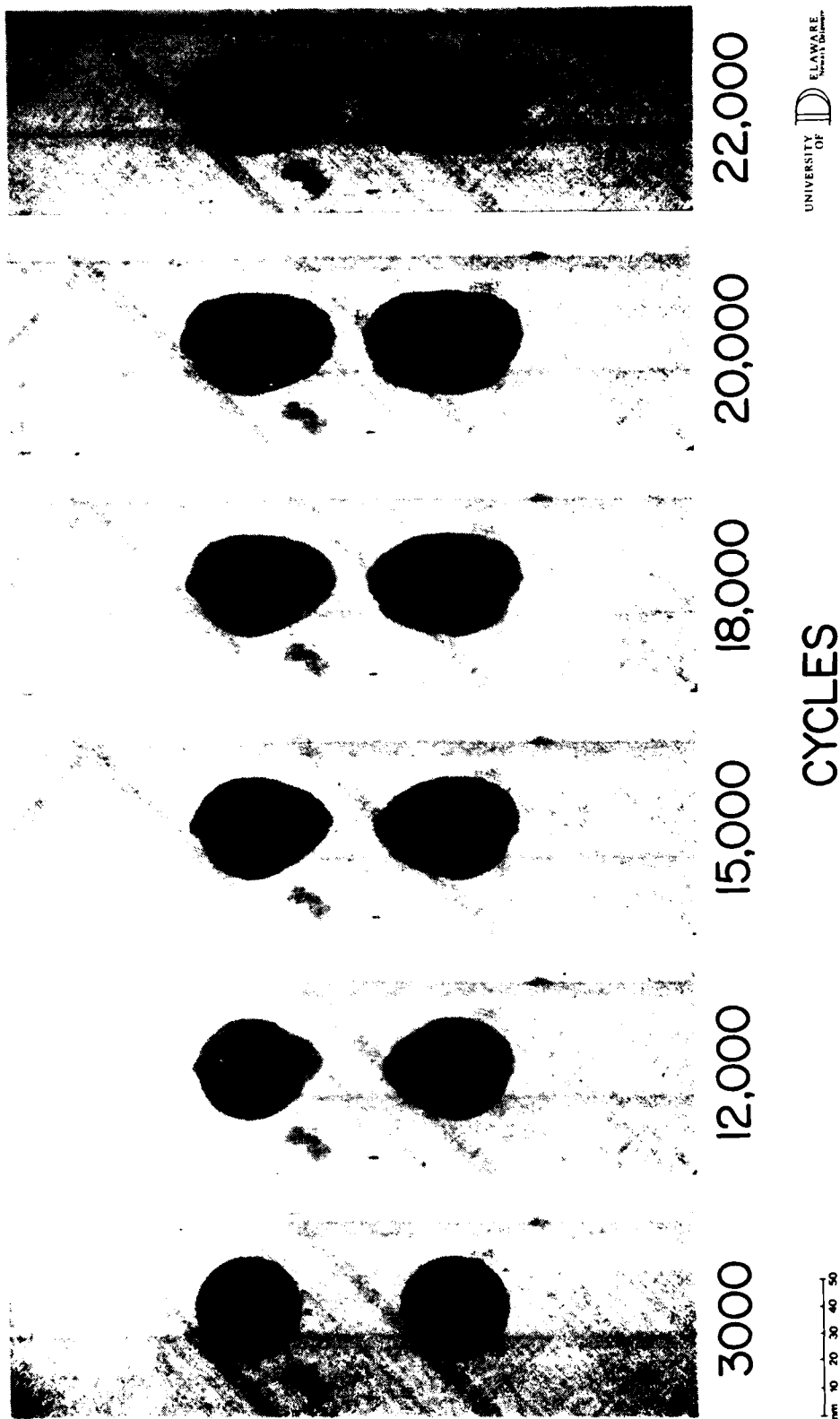
Figure 12. C-Scan of Specimen 1.5C-2, S=0.5

Figure 13. C-Scan of Specimen 1.5C2-1, S=0.5
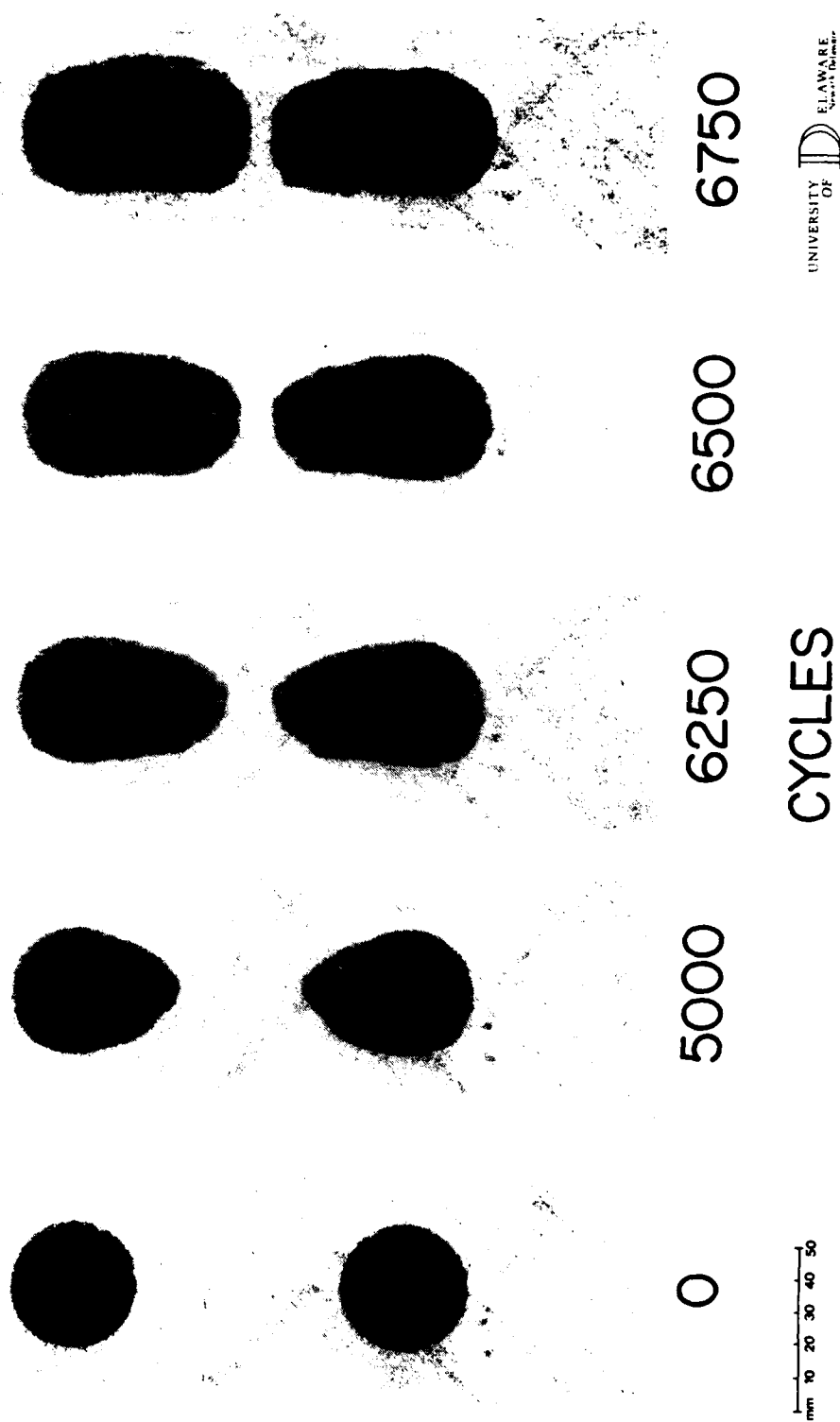
Figure 14. C-Scan of Specimen 1.5C2-2, S=0.5

Figure 15. C-Scan of Specimen 1.0C2-4, S=0.6

-63-

Figure 16. C-Scan of Specimen 1.25C-4, S=0.6

-64-

SPECIMEN 1.25 C2-4

S=0.6

3000 16,000 36,000 41,000 46,000

CYCLES
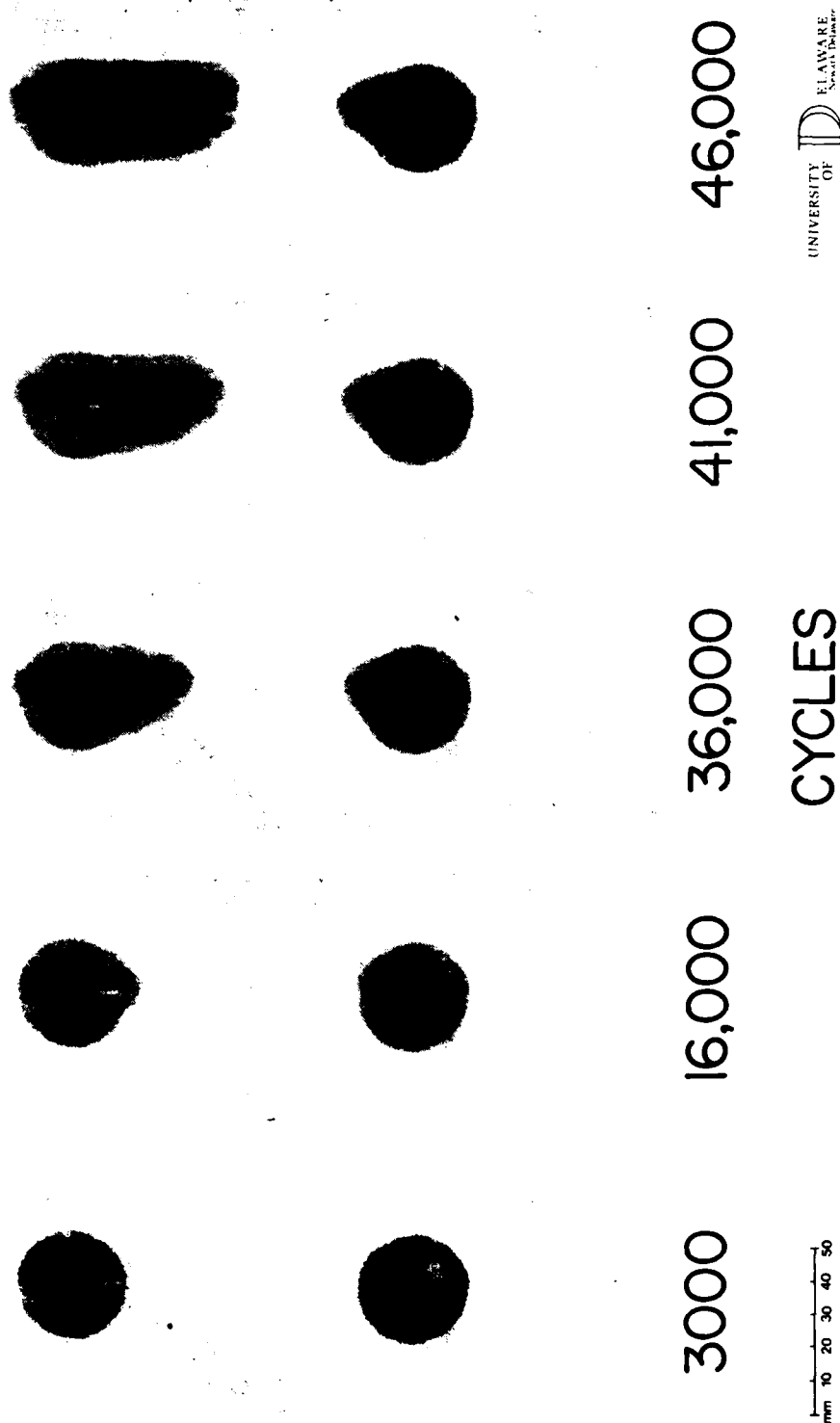
mm 10 20 30 40 50

Figure 17. C-Scan of Specimen 1.25C2-4, S=0.6

-65-

Figure 18.   C-Scan of Specimen 1.5C-4, S=0.6
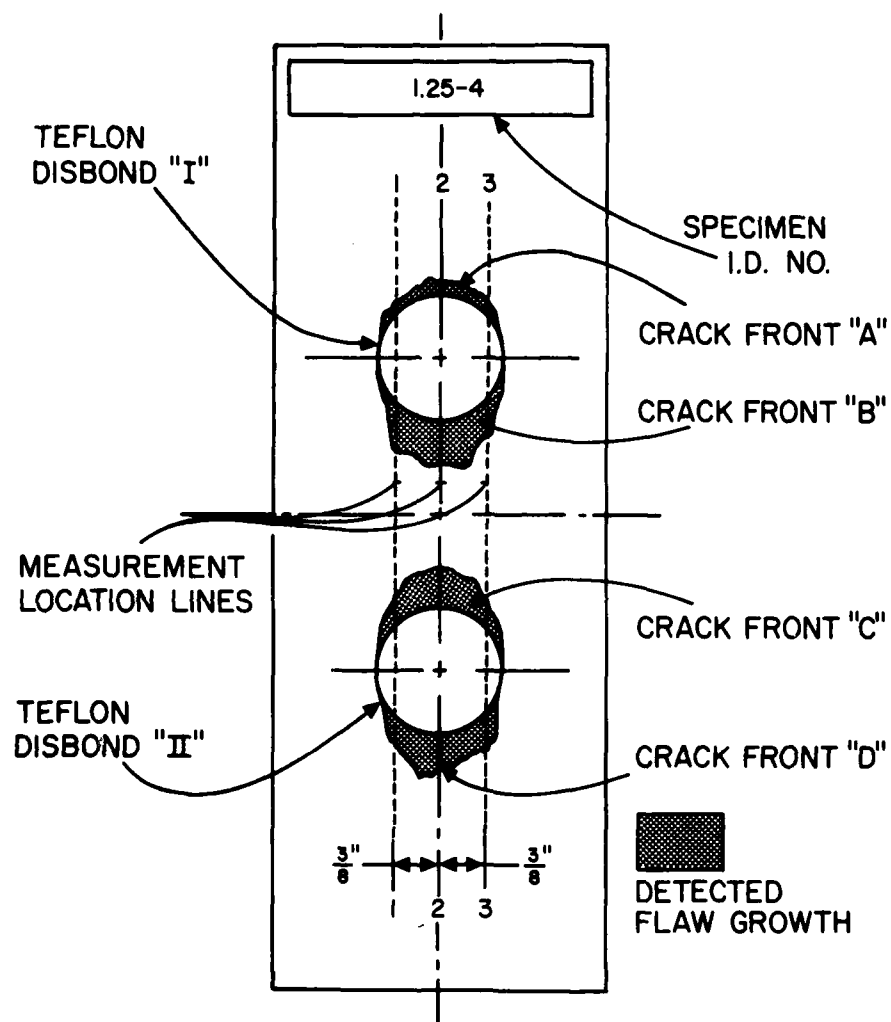
Figure 19. Measurement Locations for Four Crack Fronts
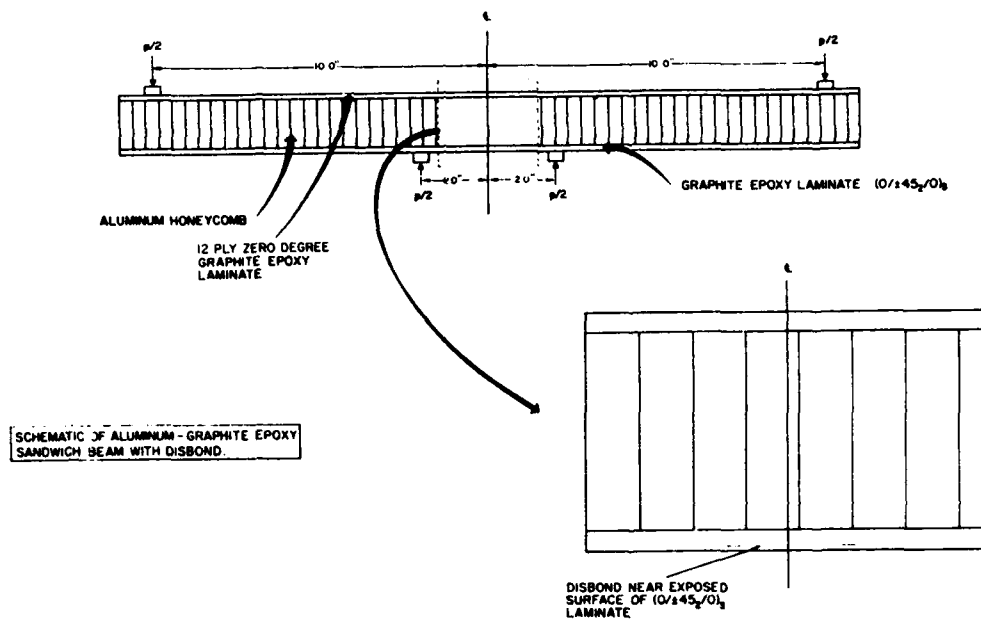
Figure 20. Sandwich Beam Specimen Geometry
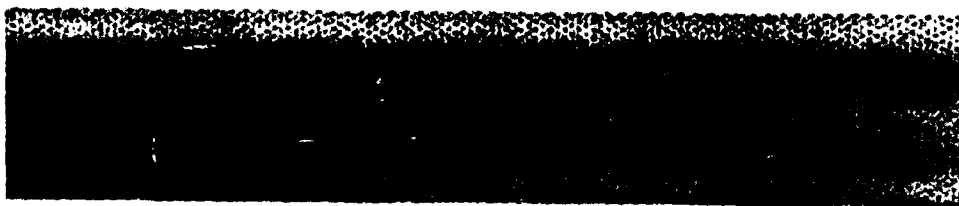
Figure 21a.   No Defect
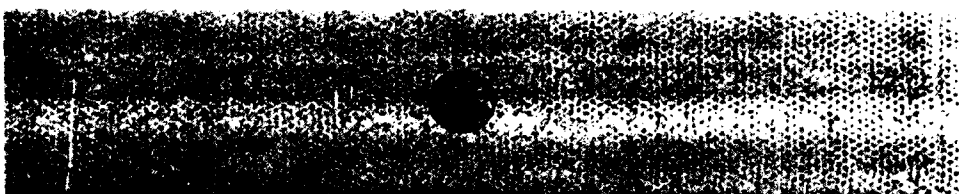
Figure 21b.   1" Circular Near Surface Defect
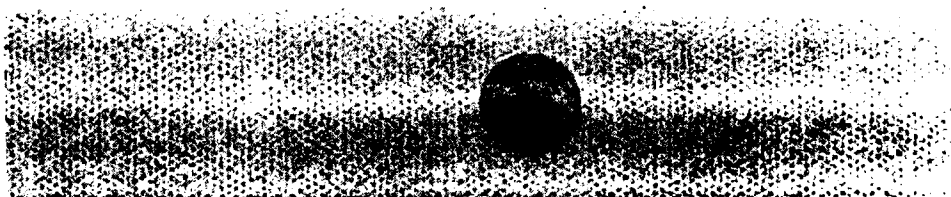
Figure 21c.   1.5" Circular Near Surface Defect
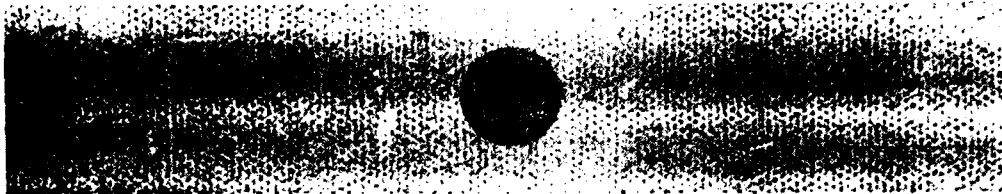
Figure 21.   C-Scans of Sandwich Beam Specimens

Figure 21d.   1.5" Circular Midply Defect

Figure 21e.   2" Circular Midply Defect

Figure 21f.   2" x 2." Square Midply Defect
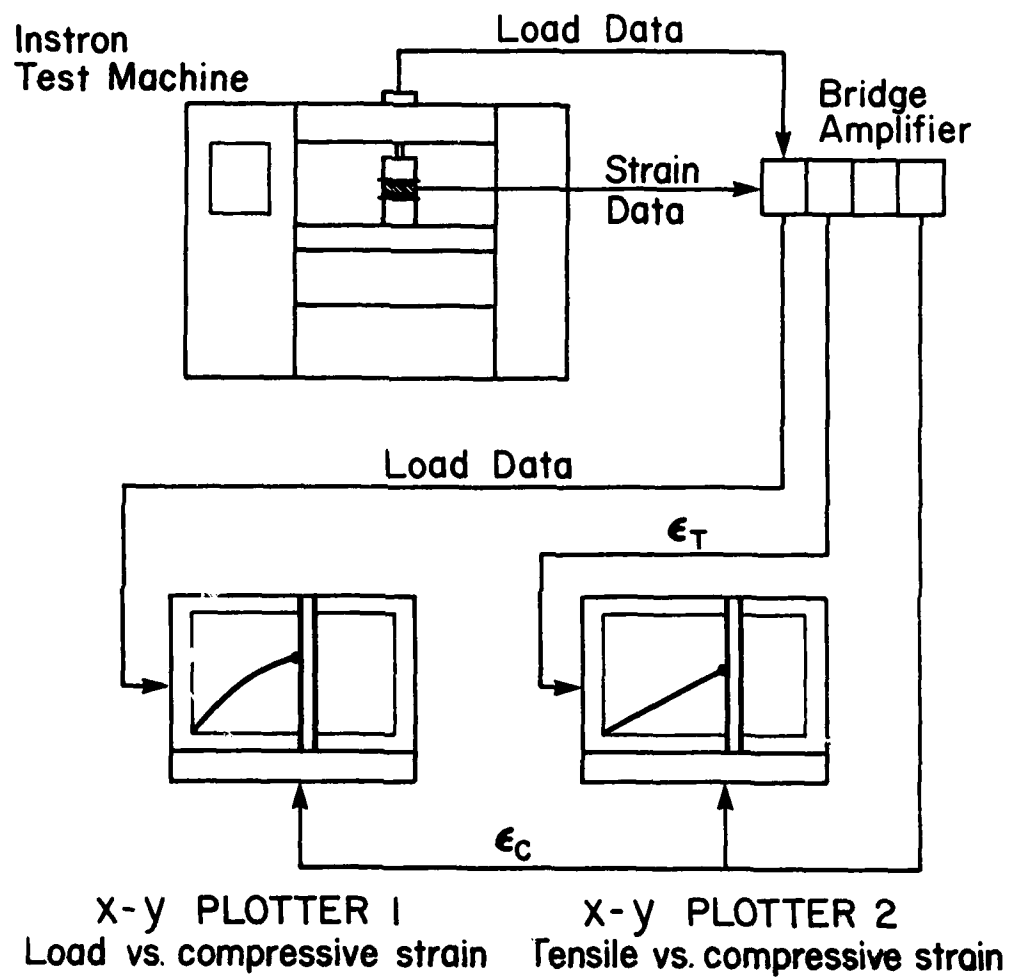
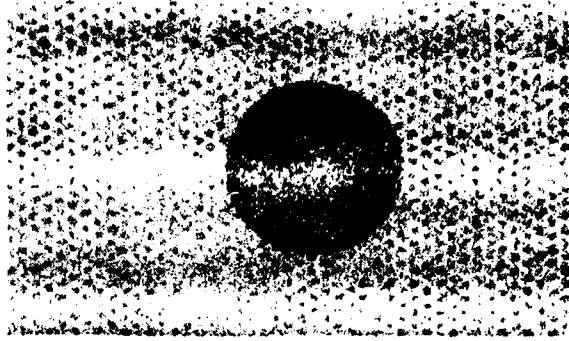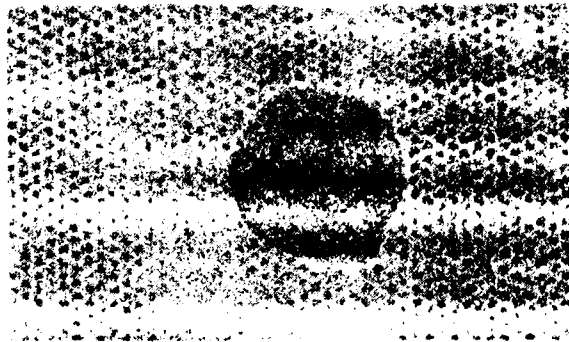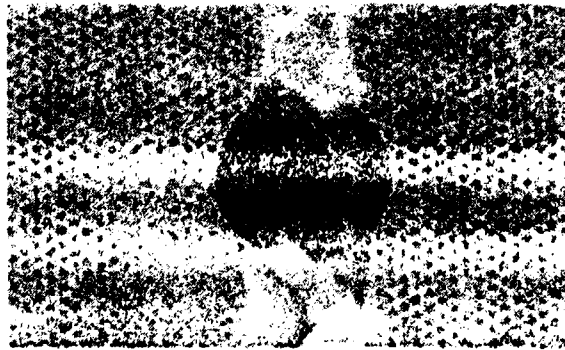Figure 21 (continued).   C-Scans of Sandwich Beam Specimens

Figure 22. Sandwich Beam Testing Schematic

1.5" Circular Near Surface Delamination Prior to Testing

1.5" Circular Near Surface Delamination After Buckling

1.5" Circular Near Surface Delamination
After 2000 Kg Applied Load

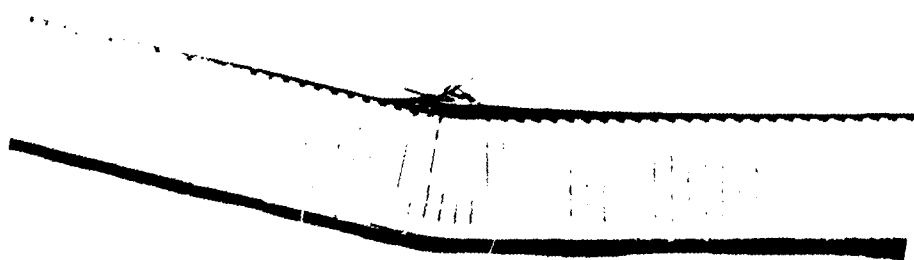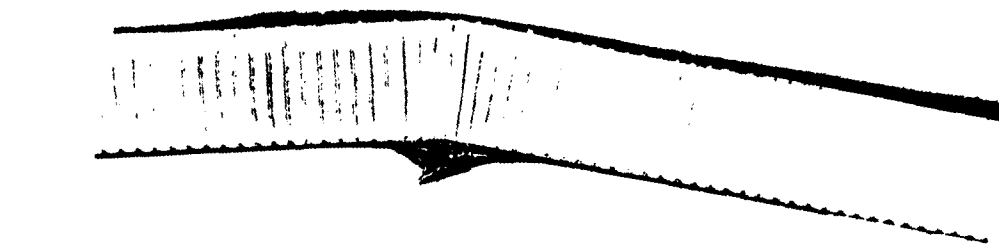Figure 23.   Near Surface Delamination Propagation Sequence

Figure 24. Failure of Sandwich Beam Composite
with No Defect
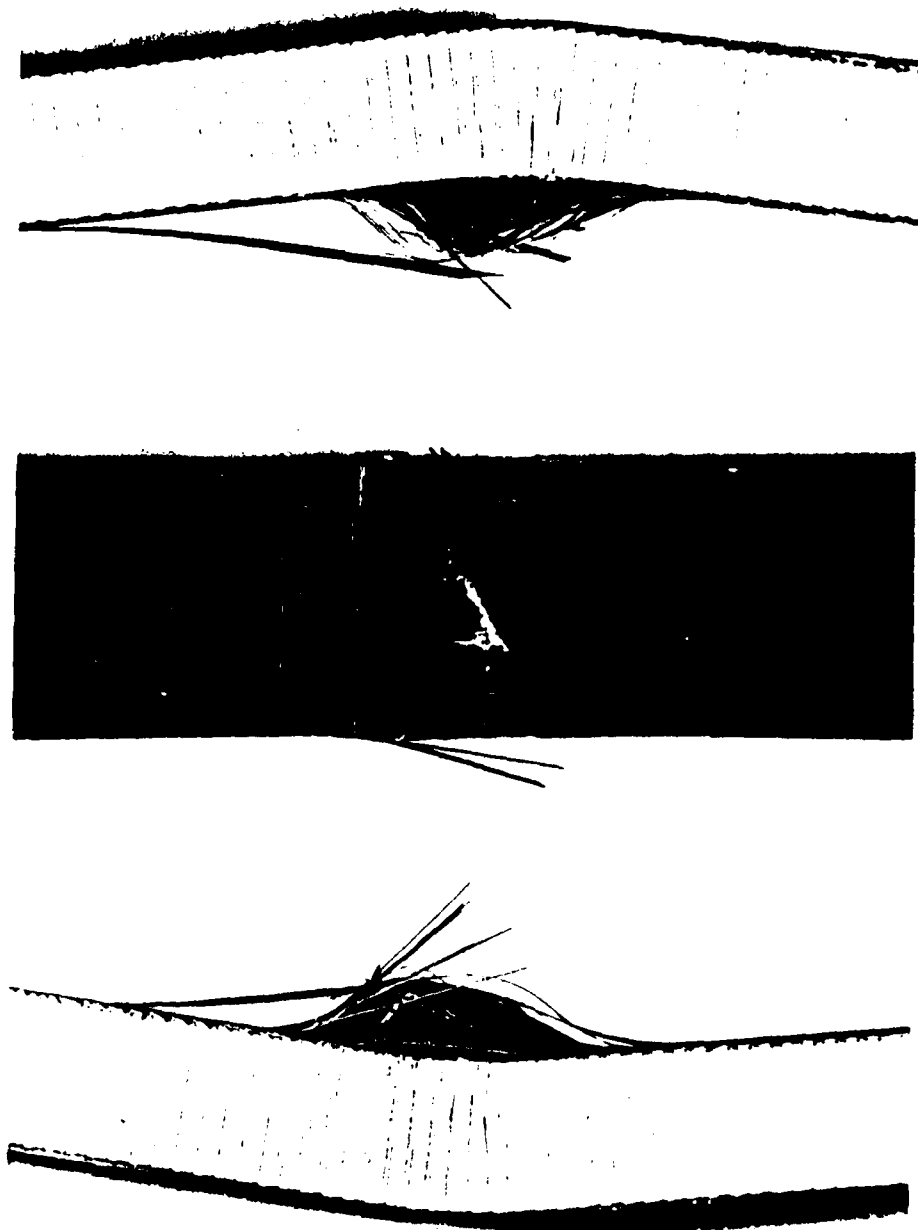
Figure 25. Failure of Sandwich Beam Composite
with a 1.0" Circular Defect
Located at the Near Surface

Figure 26. Failure of Sandwich Beam Composite
with a 1.5" Circular Defect
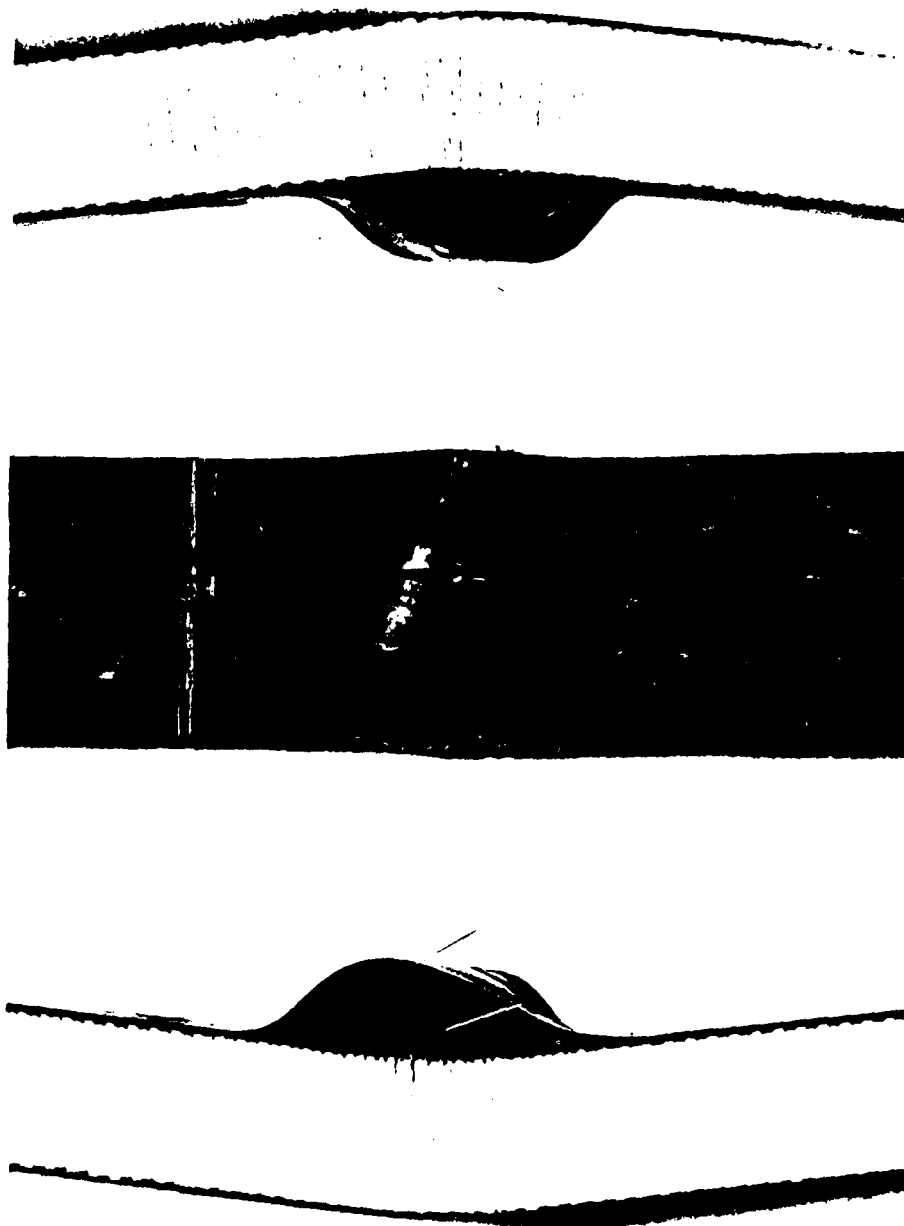Located at the Near Surface

Figure 27. Failure of Sandwich Beam Composite
with a 2.0" Circular Defect
Located at the Midply

Figure 28. Failure of Sandwich Beam Composite
with a 2.0" Defect Located at the
Midply

Figure 29. Load vs. Compressive Strain in Sandwich Beam with No Defect, Sample 1
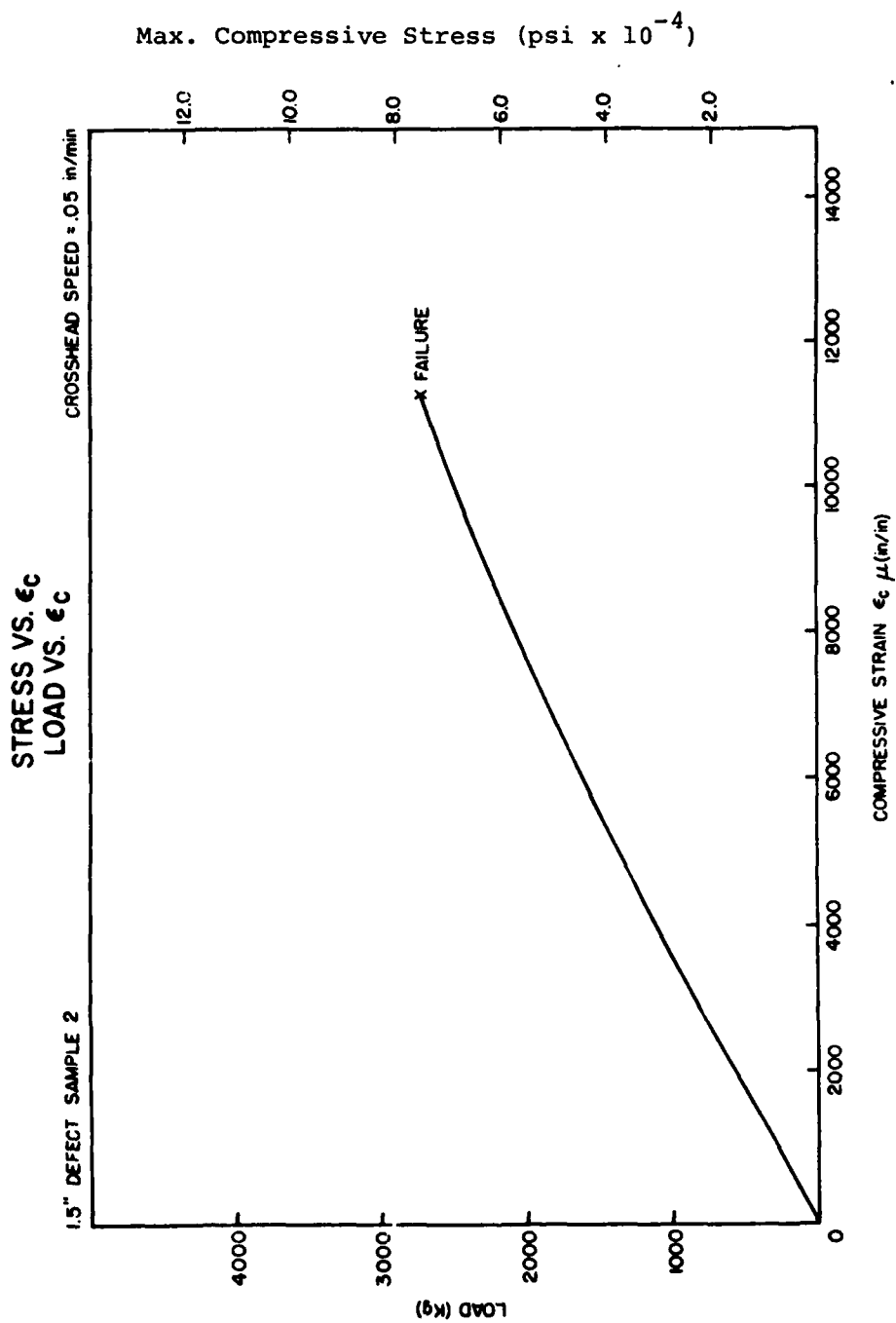
Figure 30. Load vs. Compressive Strain in Sandwich Beam with 1.5" Midply Defect, Sample 2

Max. Compressive Stress (psi x 10^{-4})

CROSSHEAD SPEED = .2 cm/min

STRESS VS. ϵ_c
LOAD VS. ϵ_c

1" DEFECT NEAR SURFACE SAMPLE 1

COMPRESSIVE STRAIN ϵ_c μ (in/in)
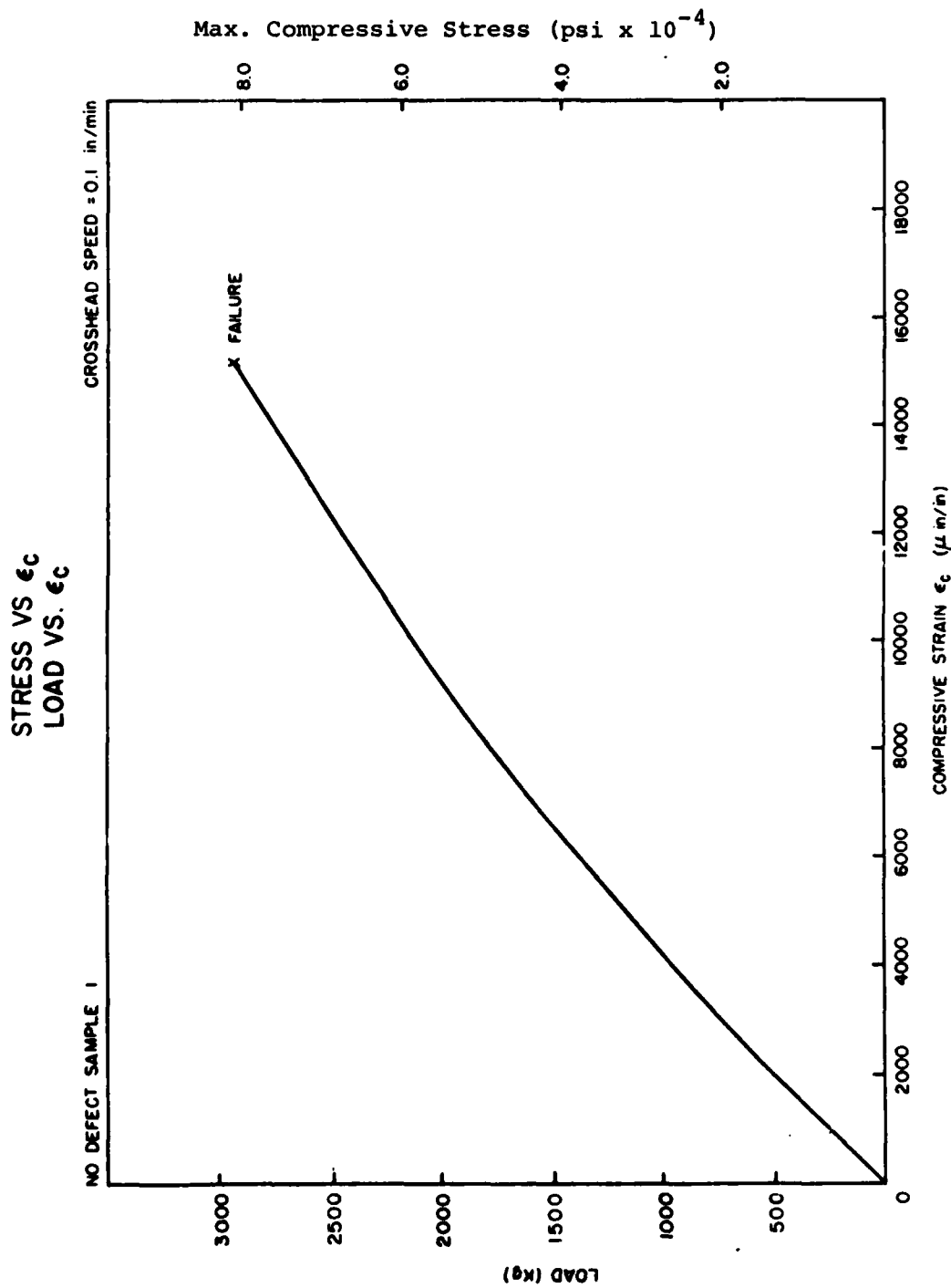
LOAD (kg)
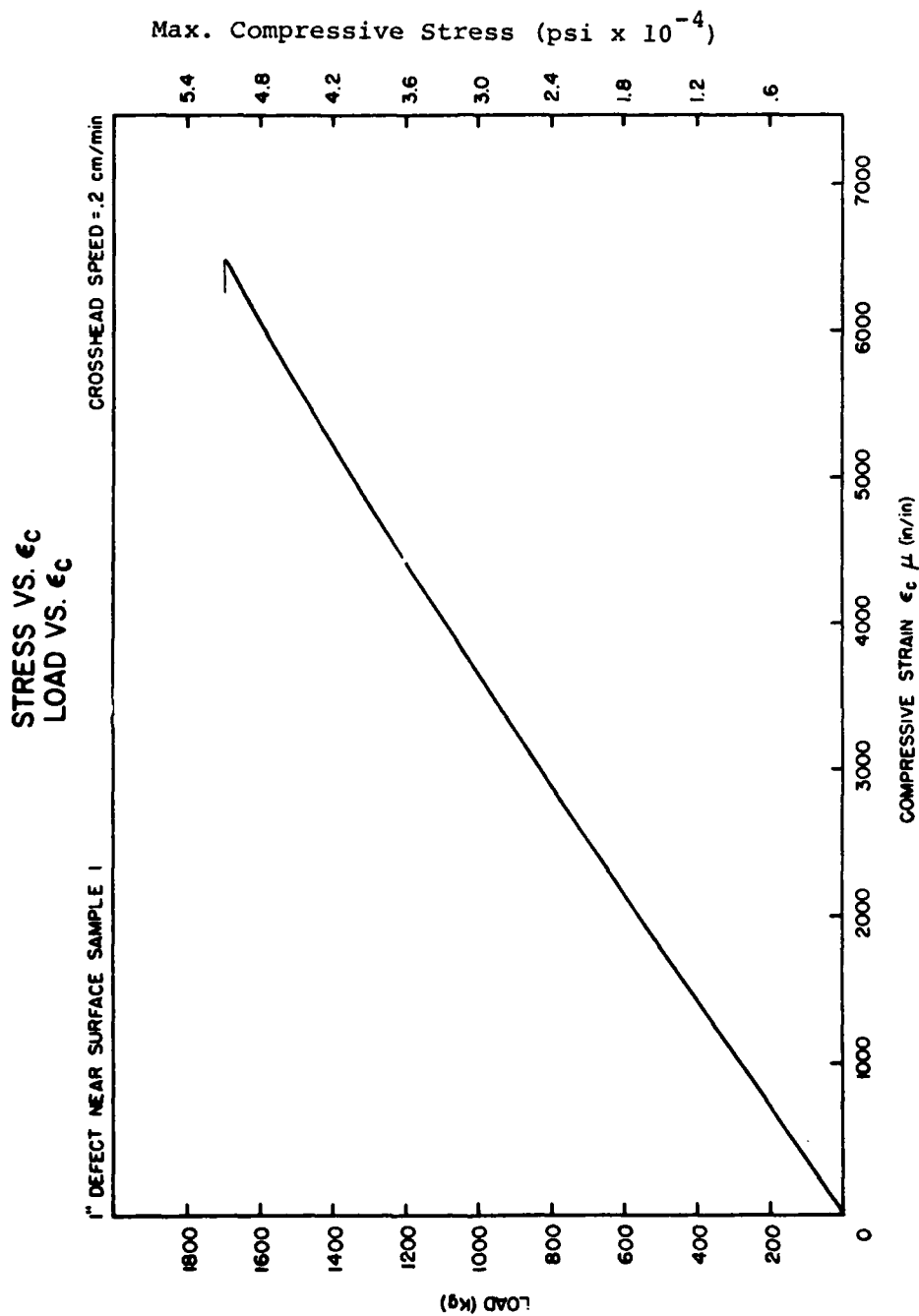
Figure 31. Load vs. Compressive Strain in Sandwich Beam
with 1" Defect Near Surface, Sample 1
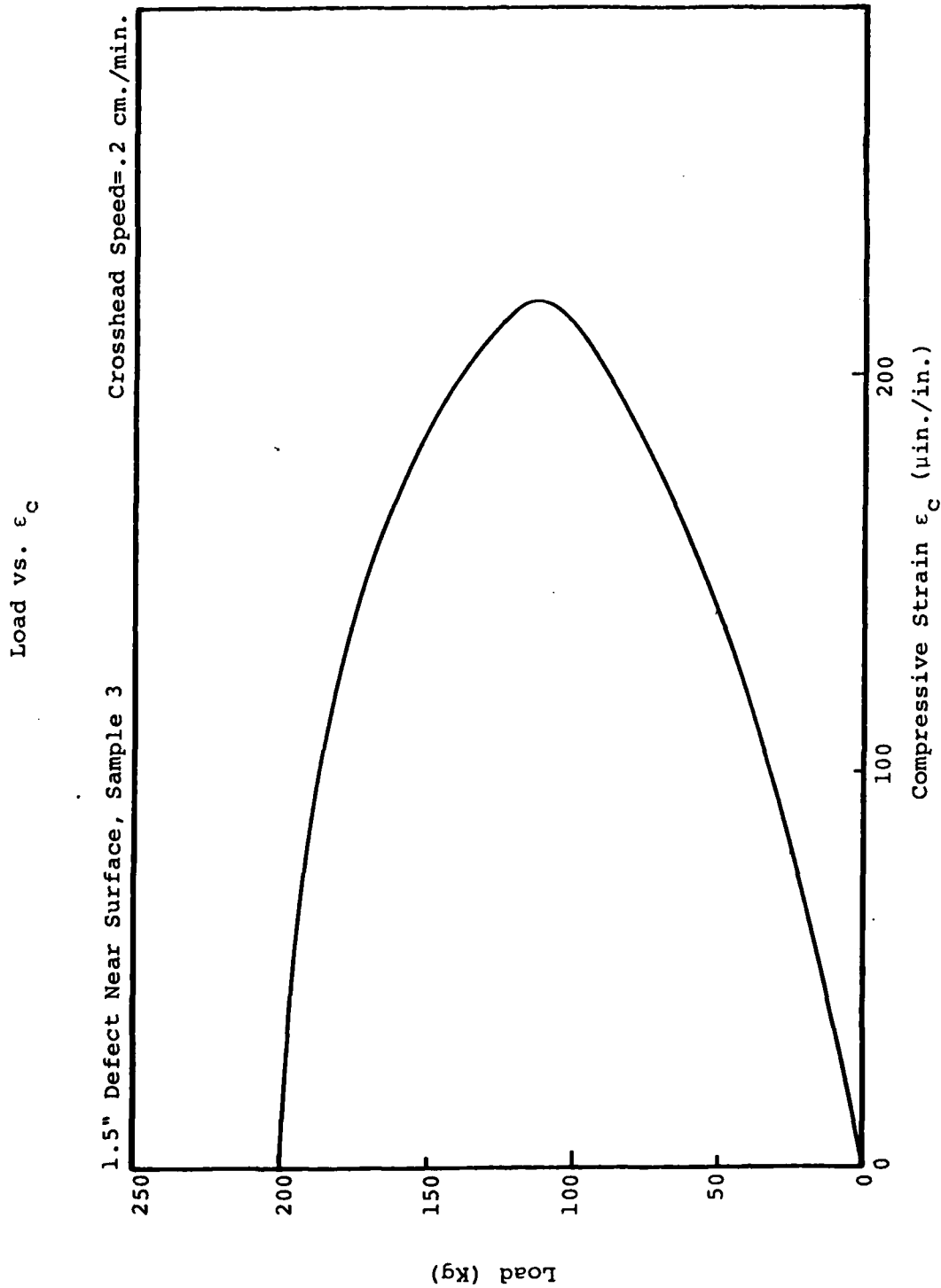
Figure 32. Load vs. Compressive Strain in Sandwich Beam with 1.5" Defect Near Surface, Sample 3

SIGNAL PROCESSING FACILITY

LA 36
PAPER
TERMINAL

DIGITAL LSI II
COMPUTER AND
EXPANSION UNIT

PERIPHERAL
INTERFACE

FLATBED
PLOTTER

TEKTRONIX
GRAPHIC
DISPLAY
TERMINAL

PAPER
TAPE
READER
PUNCH

TELEPHONE
MODEM

NICOLET
DIGITAL
OSCILLOSCOPE

LOWPASS
FILTER

ANALOG INPUT
FROM SYSTEM
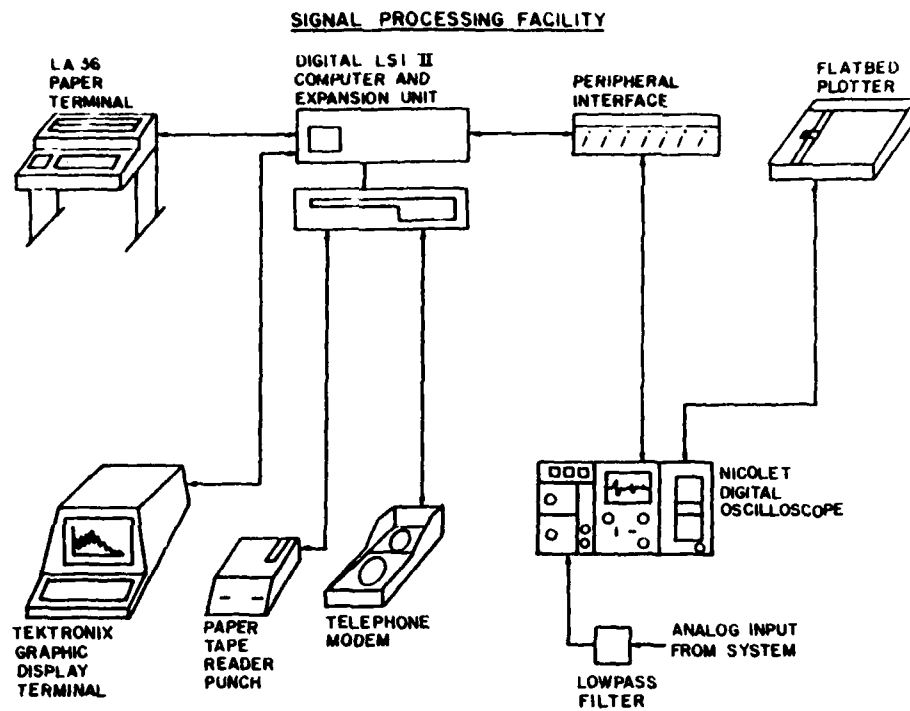
Figure 33.   Signal Processing Facility

-82-
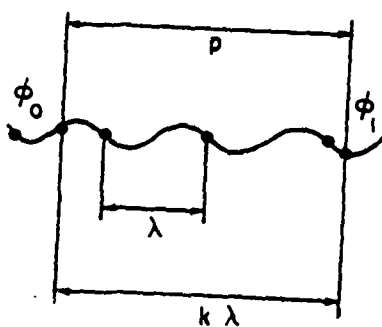
p = PATH LENGTH OF SOUND

λ = WAVE LENGTH

ϕ_0 = PHASE AT INTERFACE 0

ϕ_1 = PHASE AT INTERFACE 1

k = NUMBER OF CYCLES

c = VELOCITY OF SOUND

d = THICKNESS OF SAMPLE

f = FREQUENCY OF SOUND

ω = FREQUENCY IN RAD/SEC

$$\lambda = c/f \qquad c = \lambda f \qquad \omega = 2\pi f$$

$$(\phi_1 - \phi_0) = 2\pi k \qquad k\lambda = p \quad p = 2d$$

$$c = \frac{p f 2\pi}{(\phi_1 - \phi_0)} = \frac{p\,\omega}{(\phi_1 - \phi_0)}$$

$$c(\omega) = \frac{2d\,\omega}{(\phi_1(\omega) - \phi_0(\omega))}$$

Figure 34. Phase Velocity of Sound

1/4 INCH GRAPHITE
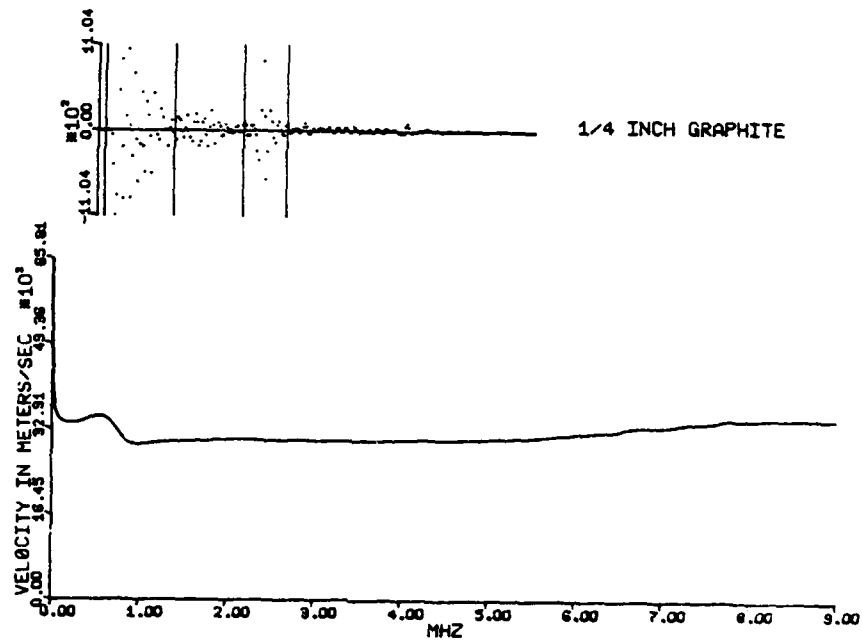
Figure 35. Velocity of Sound Measurement
for 6.35 mm. (1/4") Graphite

-84-
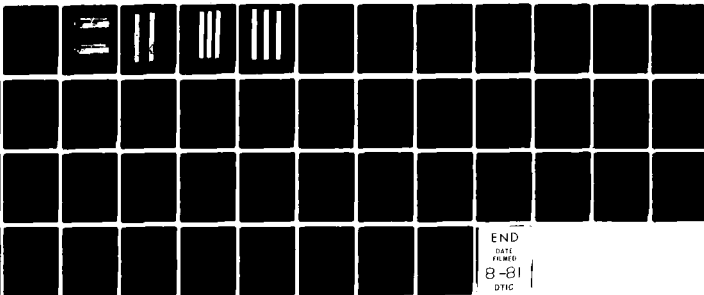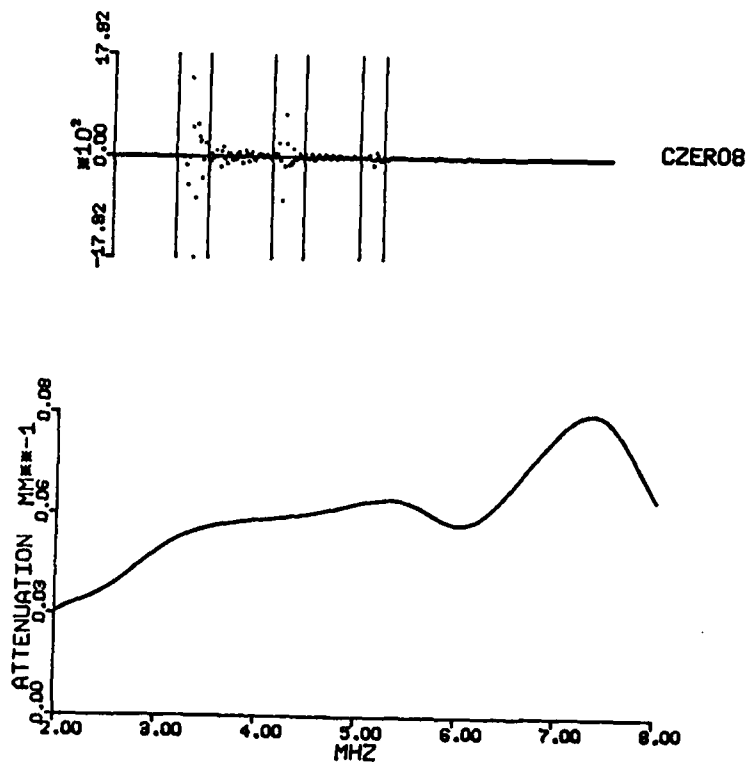
Figure 36. Attenuation of Sound Measurement
for 32-Ply, 0° Graphite/Epoxy

Figure 37. Fracture Surface of Dry Resin Sample

Figure 38. Fracture Surface of Moisture
            Conditioned Resin Sample

-86-

Moisture Conditioned $[\pm45_8]_s$ Graphite/Epoxy Sample After Static Testing

Dry $[\pm45_8]_s$ Graphite/Epoxy After Static Testing

Figure 39. C-Scans of Statically Tested Dry and Moisture Conditioned
32-Ply ±45° Graphite/Epoxy Samples
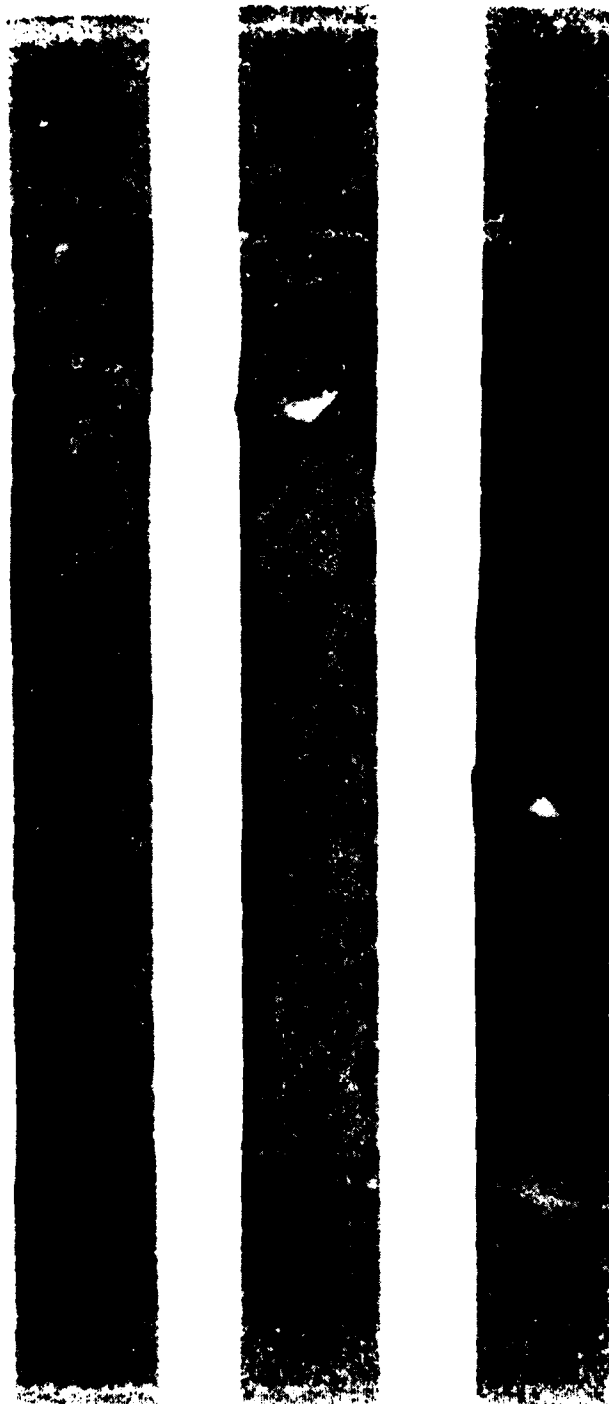
Figure 40. Ultrasonic C-Scans of Three Moisture Conditioned
and Statically Tested $[\pm 45_3]_s$ Graphite-Epoxy
Samples

75% of Ultimate Stress; 10,630 Cycles to Failure

65% of Ultimate Stress; 78,540 Cycles to Failure

50% of Ultimate Stress After 3,080,000 Cycles

Figure 41. Fatigue Conditioning of $[\pm 45_8]_s$ Graphite/Epoxy Samples
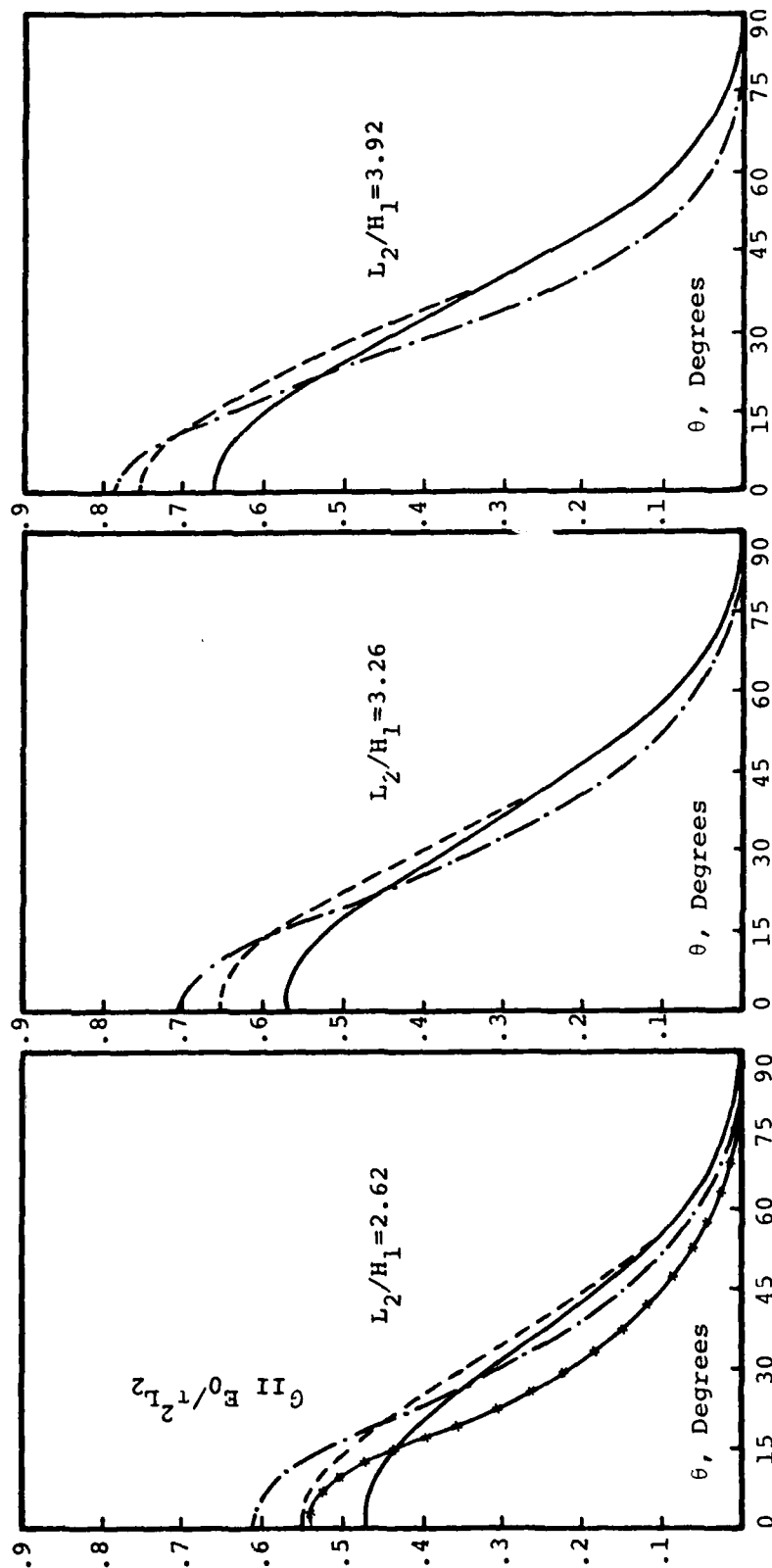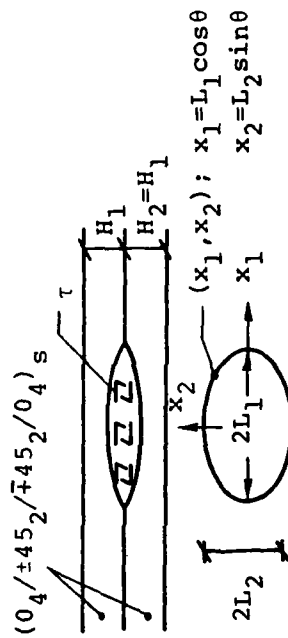
Figure 42. Variation of G_{II} with Flaw Dimensions for $[(0_4/\pm45_2/\mp45_2/0_4)_s]_s$ Laminate
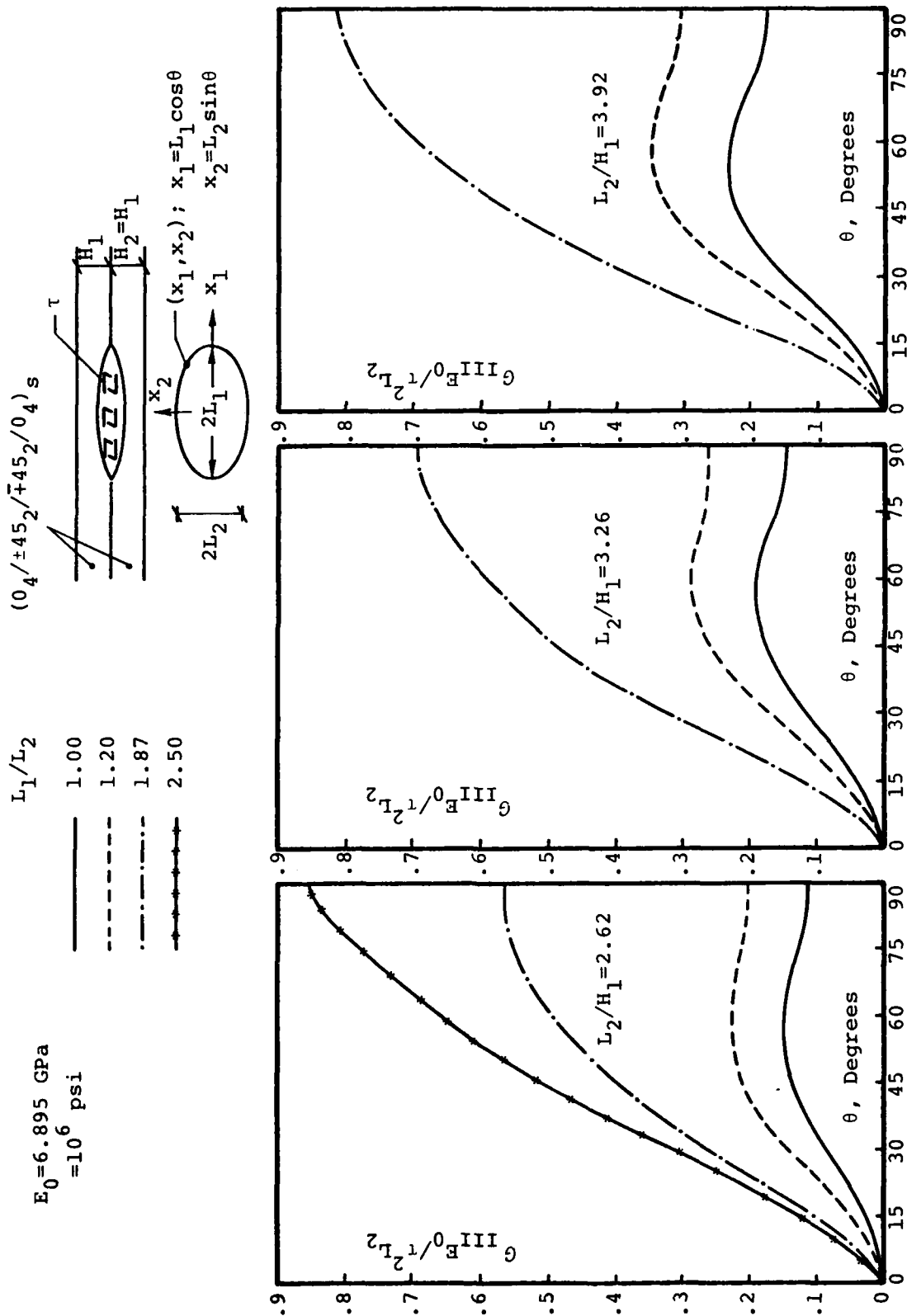
Figure 43. Variation of G_{III} with Flaw Dimensions for $[(0_4/\pm45_2/\bar{+}45_2/0_4)_s]_s$ Laminate
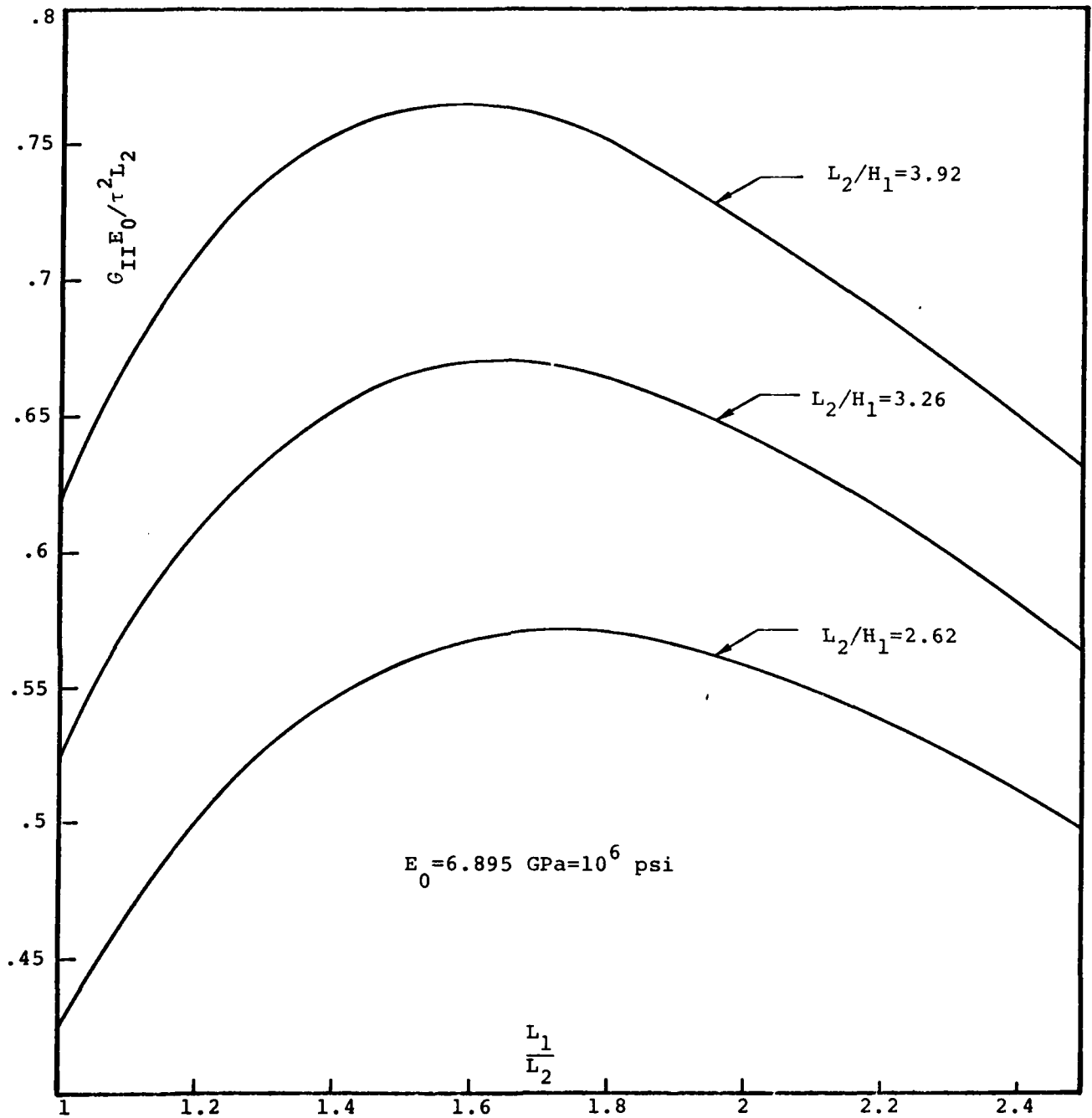
Figure 44. Variation of G_{II} at $(x=L_1, y=0)$ with L_1/L_2
for Fixed Values of L_2 for
$[(0_4/\pm45_2/\mp45_2/0_4)_s]_s$ Laminate
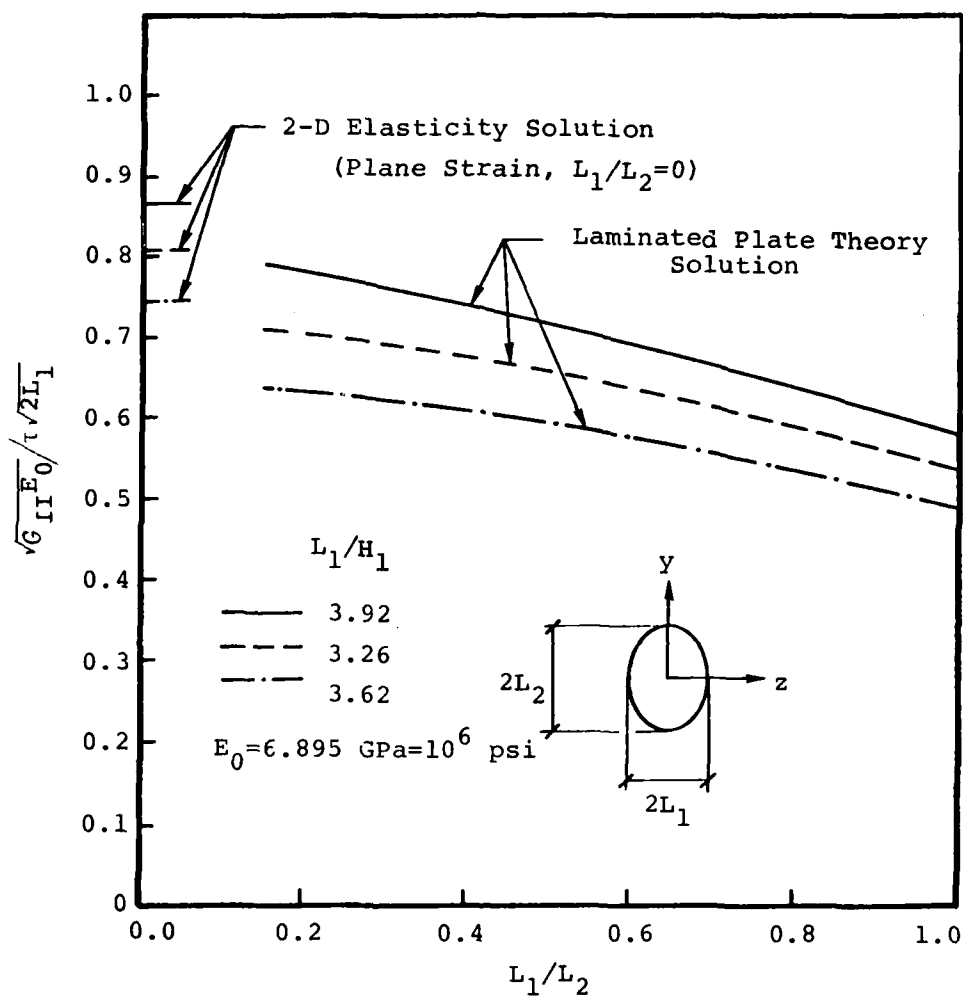
Figure 45. Variation of G_{II} at $(x=L_1, y=0)$ with L_1/L_2 for Fixed Values of L_1 for $[(0_4/\pm 45_2/\mp 45_2/0_4)_s]_s$ Laminate

-93-
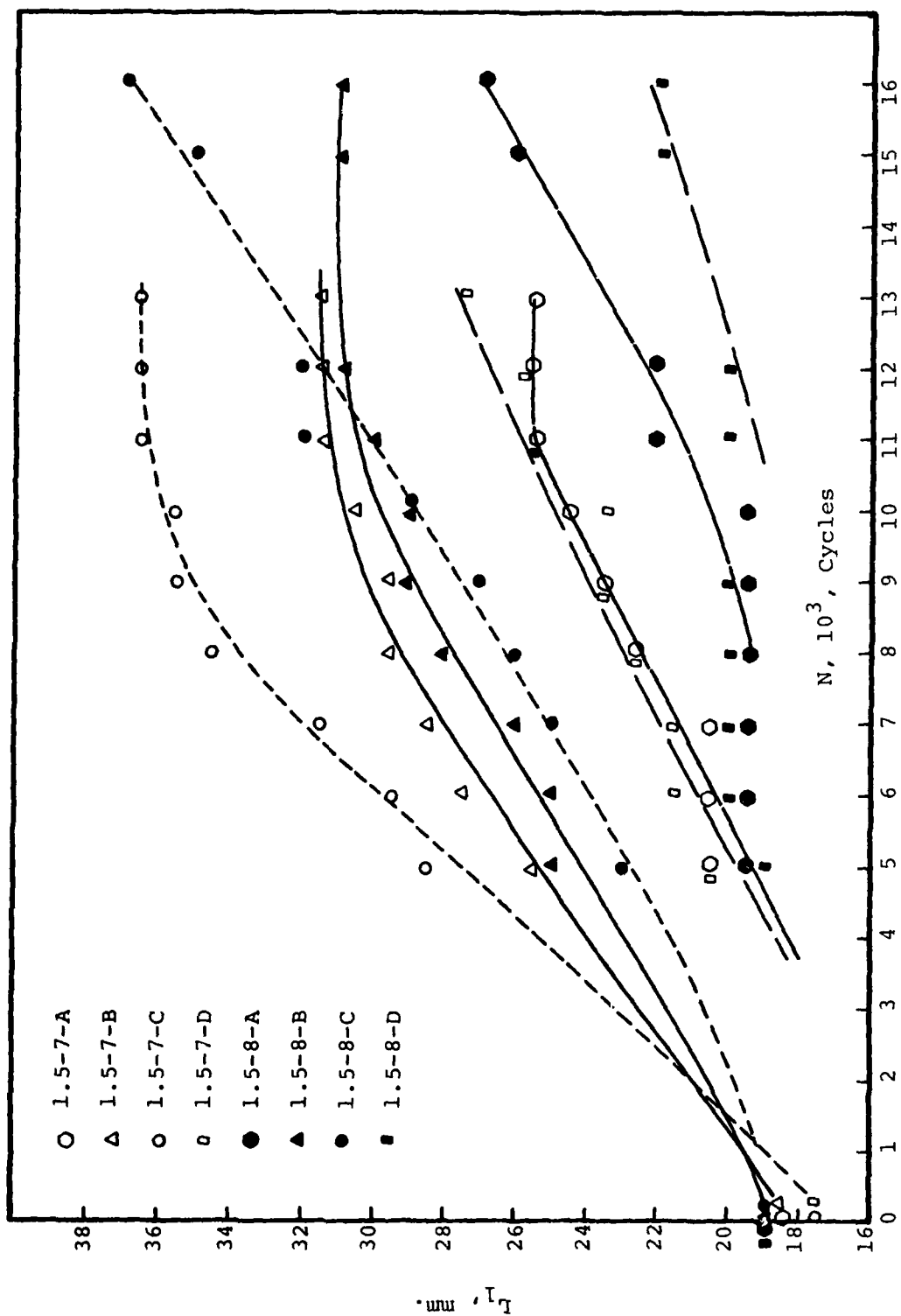
Figure 46. L_1 vs. N for Samples 1.5-7 and 1.5-8, S=0.6
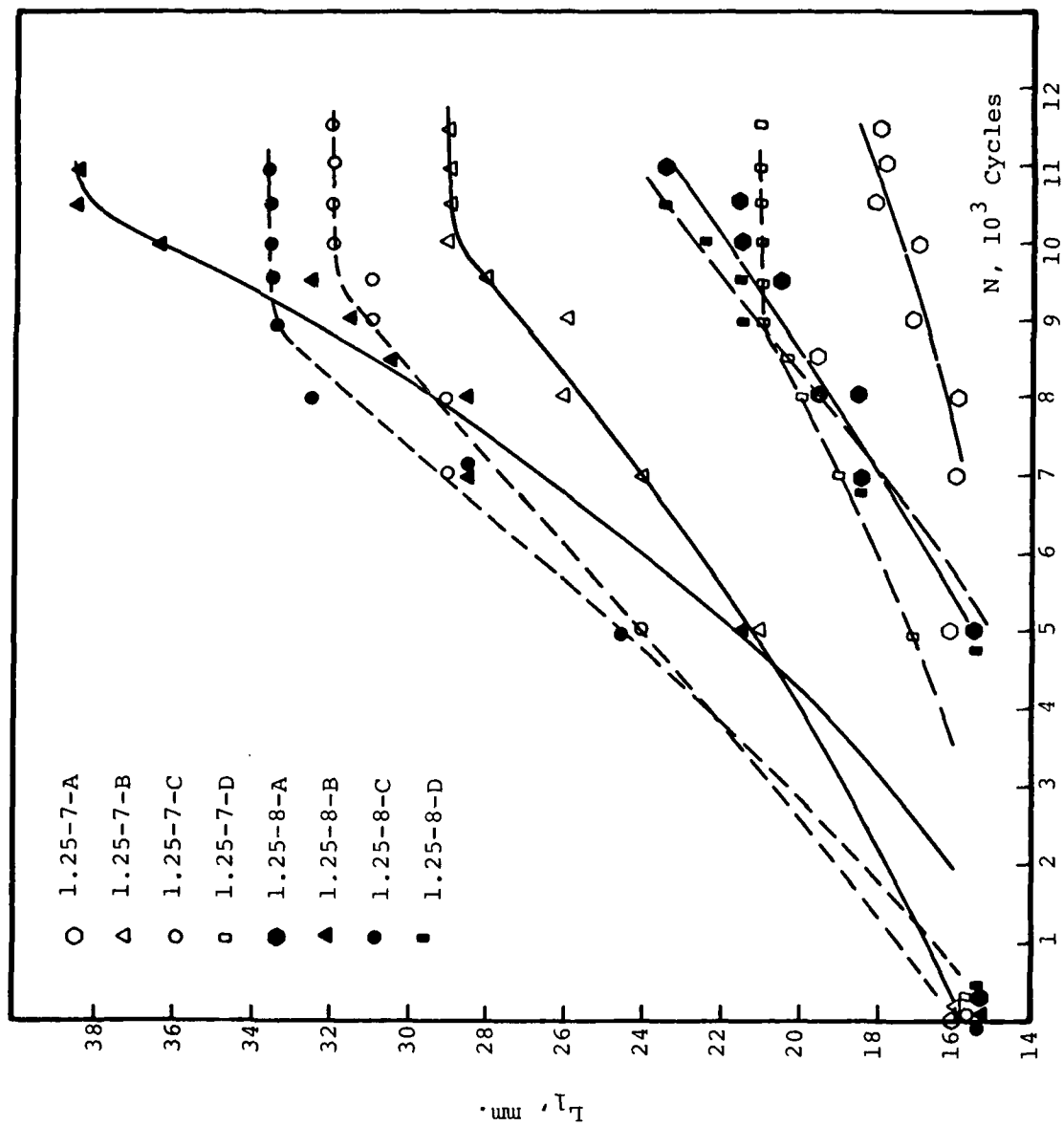
Figure 47. L_1 vs. N for Samples 1.25-7 and 1.25-8, S=0.6
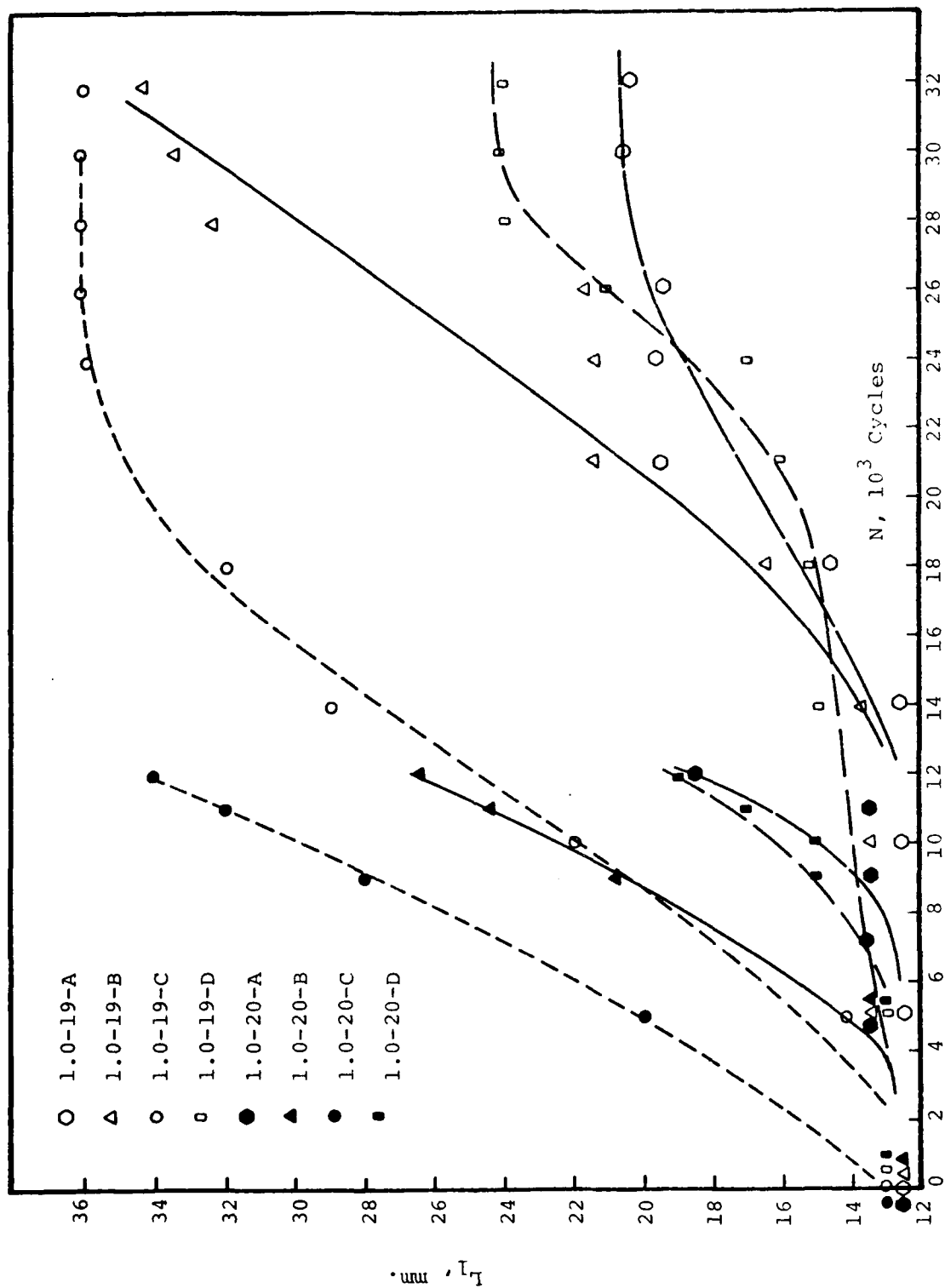
Figure 48. L_1 vs. N for Samples 1.0-19 and 1.0-20, S=0.6
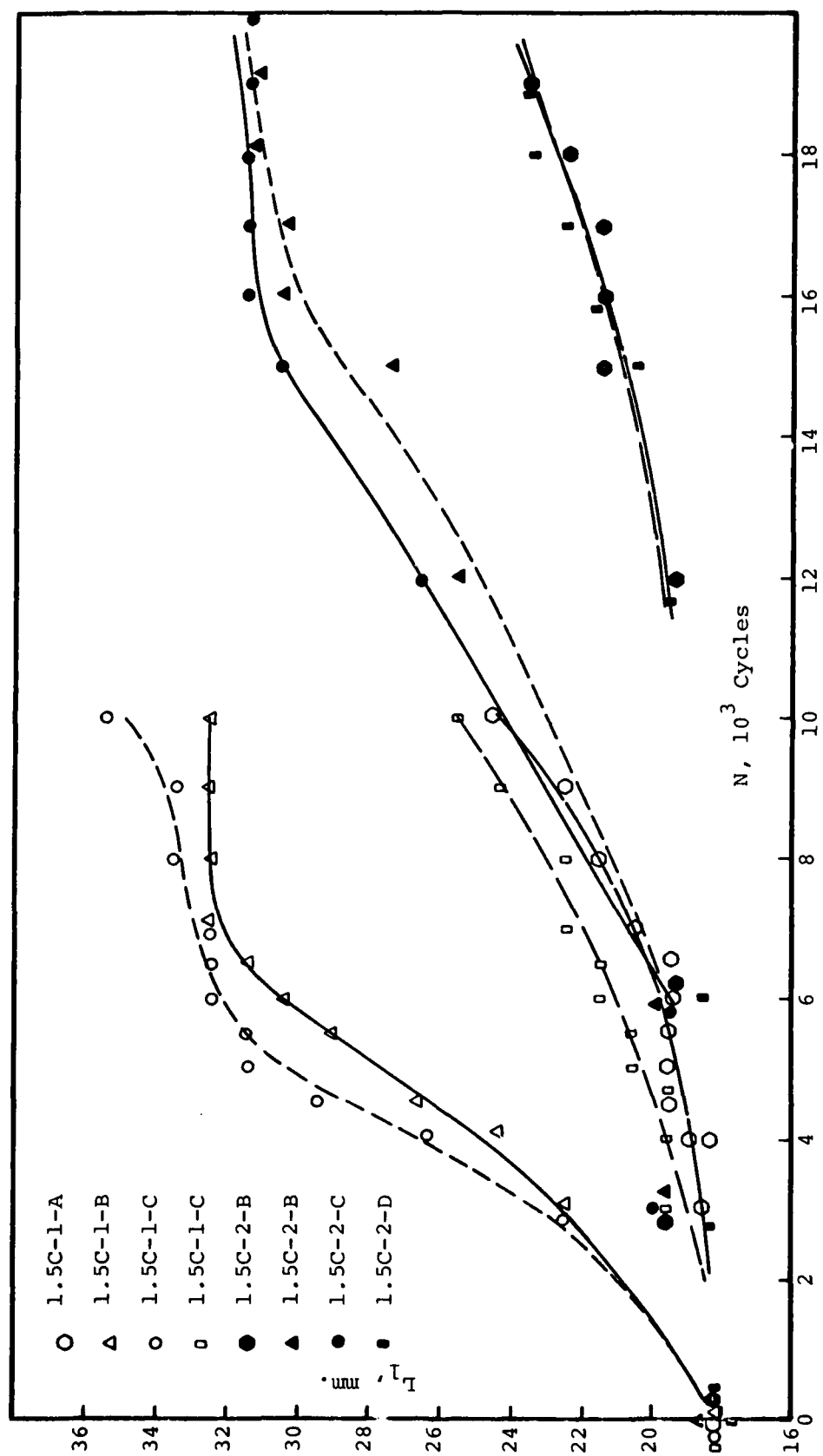
Figure 49. L_1 vs. N for Samples 1.5C-1 and 1.5C-2, S=0.5
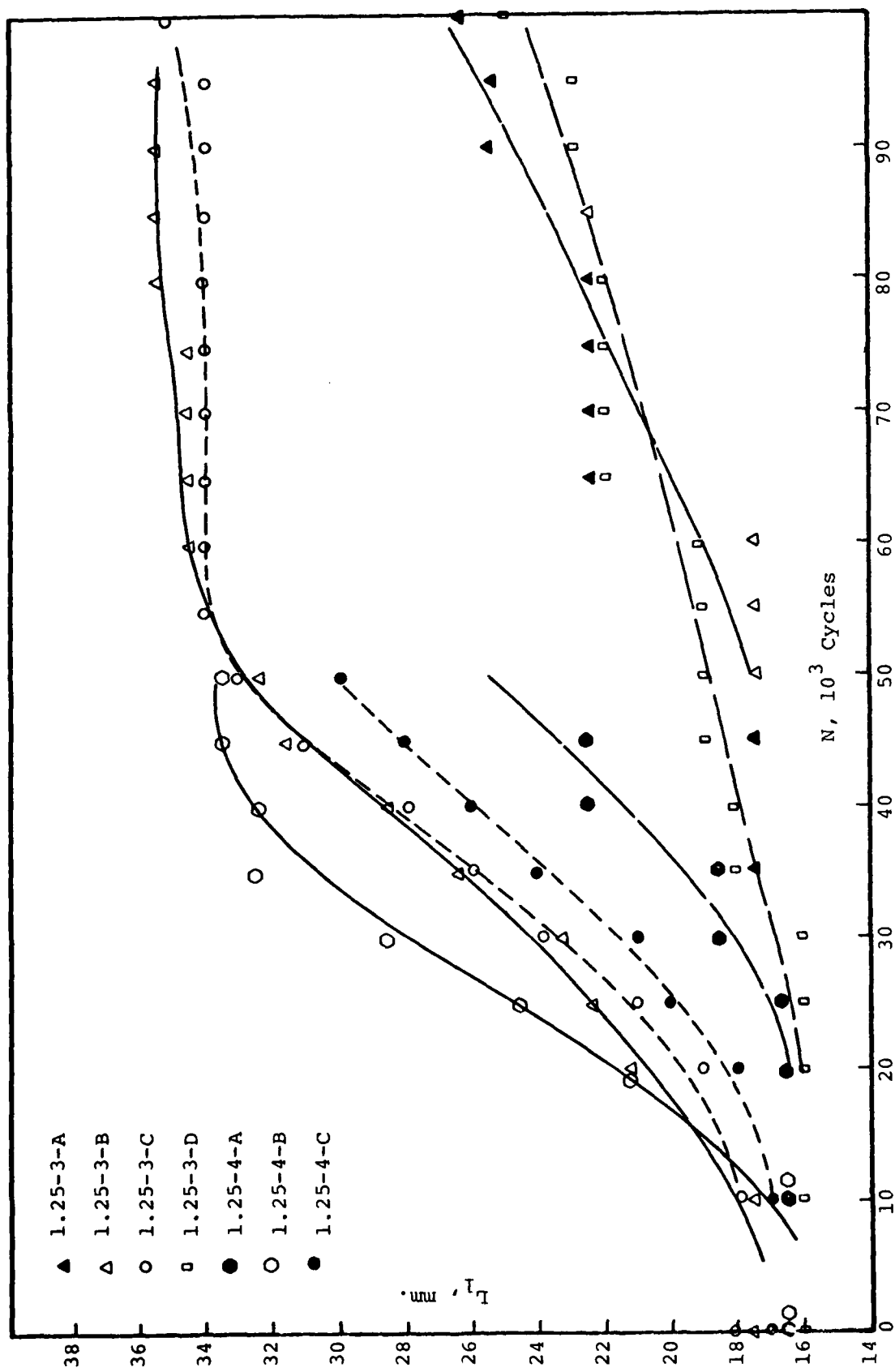
Figure 50. L_1 vs. N for Samples 1.25-3 and 1.25-4, S=0.5
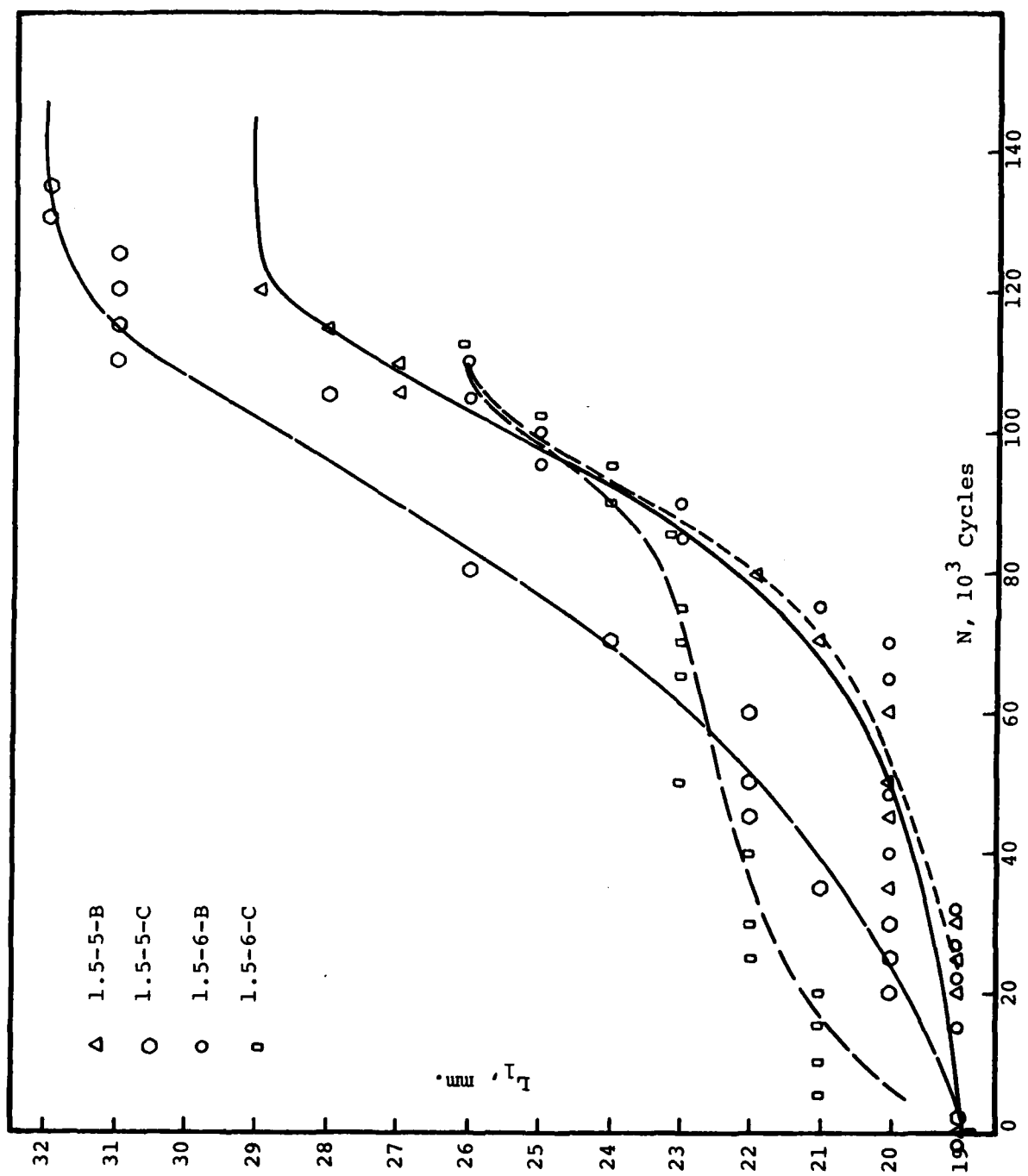
Figure 51. L_1 vs. N for Samples 1.5-5 and 1.5-6, S=0.4
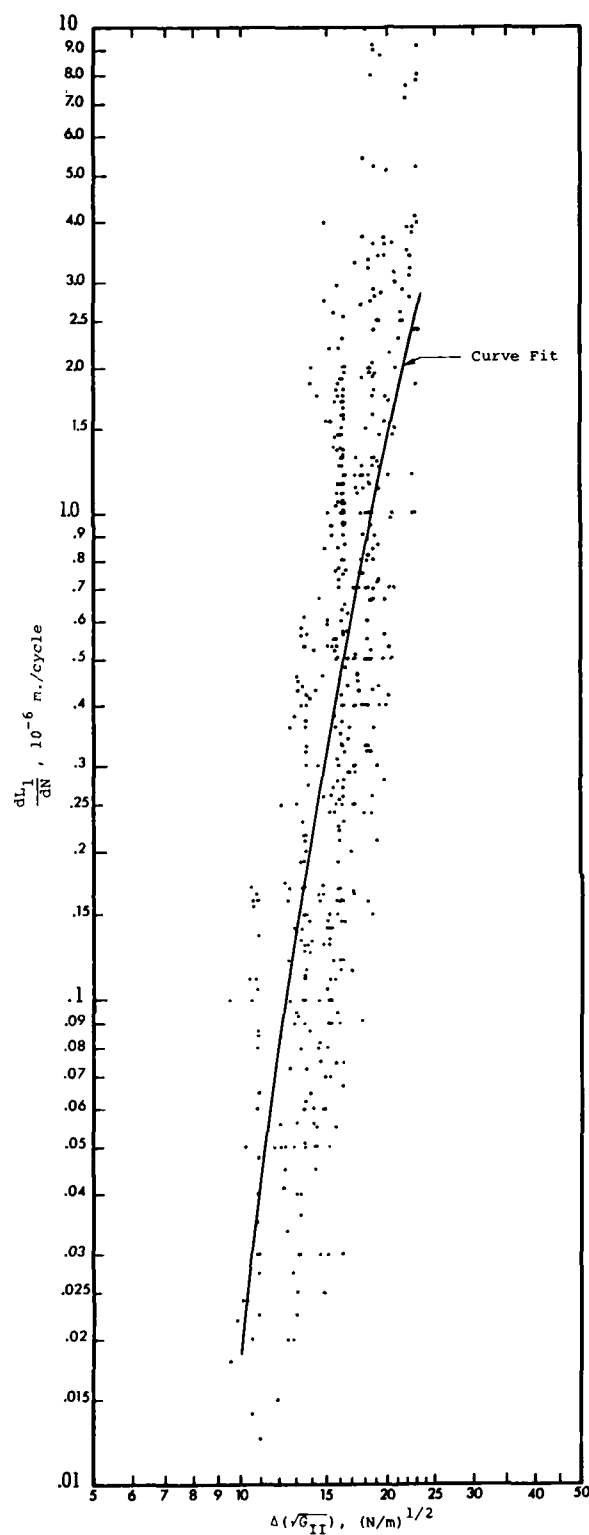
Figure 52. Growth Rates of Disbonds $\frac{dL_1}{dN}$ vs. $\Delta(\sqrt{G_{II}})$
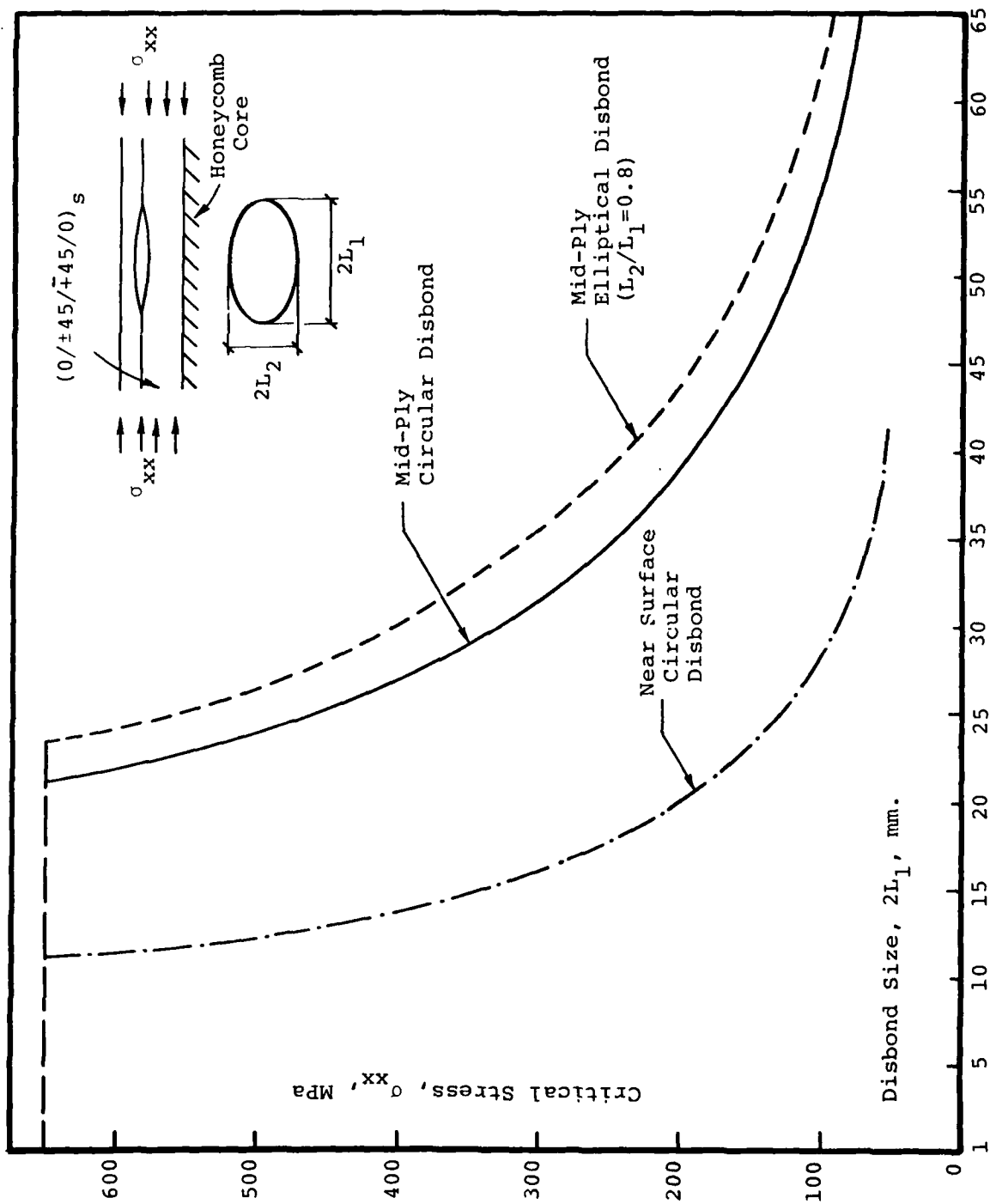
Figure 53. Critical Stress vs. Disbond Size for $(0/\pm45/\bar{+}45/0)_s$ Laminate

<u>LAMINATED PLATE THEORY WITH EFFECTS OF SHEAR</u>
<u>DEFORMATION, SURFACE TRACTIONS AND PRESTRESS</u>

The following displacement field is usually assumed in a laminated plate [ref. 7]:

$$u_x = u(x,y) + z\psi_x(x,y)$$

$$u_y = v(x,y) + z\psi_y(x,y) \qquad (A-1.1)$$

$$u_z = w(x,y)$$

The equilibrium equations in terms of the stress resultants N_{xx}, N_{yy}, N_{xy}, M_{xx}, M_{yy}, M_{xy}, Q_x, Q_y are as follows:

$$N_{xx,x} + N_{xy,y} + t_x^+ + t_x^- = 0$$

$$N_{xy,x} + N_{yy,y} + t_y^+ + t_y^- = 0$$

$$M_{xx,x} + M_{xy,y} + \frac{H}{2}(t_x^+ - t_x^-) - Q_x = 0 \qquad (A-1.2)$$

$$M_{xy,x} + M_{yy,y} + \frac{H}{2}(t_y^+ - t_y^-) - Q_y = 0$$

$$Q_{x,x} + Q_{y,y} + N_{xx}^O \, w_{,xx} + 2N_{xy}^O \, w_{,xy}$$

$$+ N_{yy}^O \, w_{,yy} + t_z^+ + t_z^- = 0$$

where $t_x^\pm$, $t_y^\pm$, $t_z^\pm$ are the surface tractions in positive x, y and z directions acting on the surfaces $z = \pm\frac{H}{2}$ of the plate, as shown in figure 2. To study the possibility of buckling under the influence of the in-plane stress resultants, the

problem is considered as that of incremental deformations. Thus, all quantities of second order are omitted. N_{xx}^{o}, N_{xy}^{o} and N_{yy}^{o} are the values of the prestresses, which are independent of spatial coordinates x and y. Their critical values are to be determined such that an alternative deformation configuration different from the present one is possible.

Substitution of the relationships between the stress resultants and derivatives of the five displacement components u, v, ψ_x, ψ_y and w results in the following system of differential equations:

$$A_{11}u_{,xx} + A_{66}u_{,yy} + 2A_{16}u_{,xy} + A_{16}v_{,xx}$$

$$+ A_{26}v_{,yy} + (A_{12} + A_{66})v_{,xy} + B_{11}\psi_{x,xx}$$

$$+ B_{66}\psi_{x,yy} + 2B_{16}\psi_{x,xy} + B_{16}\psi_{y,xx}$$

$$+ B_{26}\psi_{y,yy} + (B_{12} + B_{66})\psi_{y,xy}$$

$$+ t_x^+ + t_x^- = 0$$

$$(A-1.3)$$

$$A_{16}u_{,xx} + A_{26}u_{,yy} + (A_{12} + A_{66})u_{,xy}$$

$$+ A_{66}v_{,xx} + A_{22}v_{,yy} + 2A_{26}v_{,xy} + B_{16}\psi_{x,xx}$$

$$+ B_{26}\psi_{x,yy} + (B_{12} + B_{66})\psi_{x,xy} + B_{66}\psi_{y,xx}$$

$$+ B_{22}\psi_{y,yy} + 2B_{26}\psi_{y,xy} + t_y^+ + t_y^- = 0$$

$$B_{11}u_{,xx} + B_{66}u_{,yy} + 2B_{16}u_{,xy} + B_{16}v_{,xx}$$

$$+ B_{26}v_{,yy} + (B_{12} + B_{66})v_{,xy} + D_{11}\psi_{x,xx}$$

$$+ D_{66}\psi_{x,yy} + 2D_{16}\psi_{x,xy} + D_{16}\psi_{x,xx}$$

$$+ D_{26}\psi_{y,yy} + (D_{12} + D_{66})\psi_{y,xy} - K_{55}(\psi_x + w_{,x})$$

$$- K_{45}(\psi_y + w_{,y}) + \frac{H}{2}(t_x^+ - t_x^-) = 0$$

$$B_{16}u_{,xx} + B_{26}u_{,yy} + (B_{12} + B_{66})u_{,xy}$$

$$+ B_{66}v_{,xx} + B_{22}v_{,yy} + 2B_{26}v_{,xy} + D_{16}\psi_{x,xx}$$

$$+ D_{26}\psi_{x,yy} + (D_{12} + D_{66})\psi_{x,xy} + D_{66}\psi_{y,xx}$$

$$+ D_{22}\psi_{y,yy} + 2D_{26}\psi_{y,xy} - K_{45}(\psi_x + w_{,x})$$

$$- K_{44}(\psi_y + w_{,y}) + \frac{H}{2}(t_y^+ - t_y^-) = 0$$

$$(K_{55} + N_{xx}^O)w_{,xx} + 2(K_{45} + N_{xy}^O)w_{,xy}$$

$$+ K_{44}w_{,yy} + K_{55}\psi_{x,x} + K_{45}(\psi_{x,y} + \psi_{y,x})$$

$$+ K_{44}\psi_{y,y} + t_z^+ + t_z^- = 0$$

The laminate stiffnesses $A_{\alpha\beta}$, $B_{\alpha\beta}$, $D_{\alpha\beta}$ $(\alpha,\beta = 1,2,6)$ and $K_{\alpha\beta}$ $(\alpha,\beta = 4,5)$ are calculated from the plane stress coefficients $Q_{\alpha\beta}$ of all the layers in the plate by the following relations:

$$A_{\alpha\beta}, \; B_{\alpha\beta}, \; D_{\alpha\beta} \;\; = \;\; \int_{-H/2}^{H/2} Q_{\alpha\beta}(1,z,z^2)\,dz \; ;$$

$$(\alpha,\beta = 1,2,6) \tag{A-1.4}$$

and $\quad K_{\alpha\beta} \;\; = \;\; k'_{\alpha\beta} \, A'_{\alpha\beta} \; ; \quad (\alpha,\beta = 4,5) \tag{A-1.5}$

where $[A'] \quad = \quad [\widetilde{L}]^{-1}$

$$\widetilde{L}_{\alpha\beta} \quad = \quad \frac{1}{H^2} \int_{-H/2}^{H/2} \widetilde{S}_{\alpha\beta}\,dz$$

$$\tag{A-1.6}$$

$$[\widetilde{S}] \quad = \quad [Q]^{-1}$$

$$[Q] \quad = \quad \begin{bmatrix} Q_{44} & Q_{45} \\ Q_{45} & Q_{55} \end{bmatrix}$$

and $k'_{\alpha\beta}$ are the shear correction factors as described in references 24, 25.

APPENDIX A-2
STRESS ANALYSIS IN A DISBONDED LAMINATE

In this section a method of solution of the boundary value problem of the disbonded laminate, as shown in figure 1, is outlined. Three-dimensional elasticity solution is not attempted. A lower order structural theory based on the governing differential equations of laminated plates outlined in Appendix A-1 is utilized. The disbond is located between two laminates whose dimensions in x- and y-directions are infinitely large. The surfaces of the disbond may be subjected to surface tractions in x-, y-, and z-directions. Tractions on the two surfaces are equal in magnitude but opposite in sign. It is advantageous at this stage to introduce the following non-dimensional variables corresponding to the quantities which appear in the differential equations A-1.3. For non-dimensionalization, use is made of two quantities, i.e. (i) H_0, which has the dimension of length, and (ii) D_0, which has the dimension of bending rigidity.

1. Coordinates - $[x_1, x_2] = [x,y]/H_0$

2. Thickness - $h = H/H_0$

3. Displacement Variables - $[U_1, U_2, U_3] = (u,v,w)/H_0$

$$[\psi_1, \psi_2] = [\psi_x, \psi_y]$$

4. Stiffnesses - $a_{\alpha\beta} = A_{\alpha\beta} H_0^2 / 4 D_0$ $\Big\}$ (A-2.1)

$$b_{\alpha\beta} = B_{\alpha\beta} H_0 / D_0 h \quad \Big\} \quad \alpha,\beta = 1,2,6$$

$$d_{\alpha\beta} = D_{\alpha\beta} / D_0 h^2 \quad \Big\}$$

$$e_{\alpha\beta} = K_{\alpha\beta} H_0^2 / D_0 ; \quad \alpha,\beta = 4,5$$

5. Prestress - $[N_{11}, N_{22}, N_{12}] = [N_{xx}^0, N_{yy}^0, N_{xy}^0] H_0^2 / D_0$

6. Tractions - $[t_1, t_2, t_3] = [t_x, t_y, t_z] H_0^3 / D_0$

TRANSFORMED VARIABLES

Equations (A-1.3) can now be written in terms of the non-dimensionalized variables defined in (A-2.1) and reduced to five algebraic equations by taking multiple Fourier transforms. Transforms of variables U_j, ψ_j, and t_j are denoted with a bar on top of the quantity, i.e.

$$\bar{U}_j(s_1,s_2) = \int_{-\infty}^{\infty} \int_{-\infty}^{\infty} U_j(x_1,x_2) e^{i(s_1 x_1 + s_2 x_2)} dx_1 dx_2 \qquad (A-2.2)$$

where $i=\sqrt{-1}$. The inverse transform is given by:

$$U_j(x_1,x_2) = \frac{1}{4\pi^2} \int_{-\infty}^{\infty} \int_{-\infty}^{\infty} \bar{U}_j(s_1,s_2) e^{-i(s_1 x_1 + s_2 x_2)} ds_1 ds_2 .$$

$$(A-2.3)$$

Introduction of non-dimensionalized displacement variables u_j at $z=\pm H/2$ of a laminate given by:

$$u_j^{\pm} = U_j \pm \psi_j h/2; \quad j=1,2$$

$$(A-2.4)$$

$$u_3 = U_3$$

as well as some algebraic manipulations result in the following relationship between transformed tractions $\bar{t}_j^{\pm}$ at $z=\pm H/2$ and the displacements:

$$
\begin{bmatrix} \bar{t}_1^+ \\ \bar{t}_2^+ \end{bmatrix}
\begin{bmatrix} \bar{t}_1^- \\ \bar{t}_2^- \end{bmatrix}
\begin{bmatrix} -i(\bar{t}_3^+ + \bar{t}_3^-) \end{bmatrix}
=
\left[
\begin{array}{c|c|c}
\begin{array}{c} 11 \\ C \\ (2\times2) \end{array} & \begin{array}{c} 12 \\ C \\ (2\times2) \end{array} & \begin{array}{c} 13 \\ C \\ (2\times1) \end{array} \\
\hline
\begin{array}{c} 21 \\ C \\ (2\times2) \end{array} & \begin{array}{c} 22 \\ C \\ (2\times2) \end{array} & \begin{array}{c} 23 \\ C \\ (2\times1) \end{array} \\
\hline
\begin{array}{c} 31 \\ C \\ (1\times2) \end{array} & \begin{array}{c} 32 \\ C \\ (1\times2) \end{array} & \begin{array}{c} 33 \\ C \\ (1\times1) \end{array}
\end{array}
\right]
\begin{bmatrix} \bar{u}_1^+ \\ \bar{u}_2^+ \end{bmatrix}
\begin{bmatrix} \bar{u}_1^- \\ \bar{u}_2^- \end{bmatrix}
\begin{bmatrix} -i\bar{u}_3 \end{bmatrix}
\qquad \text{(A-2.5)}
$$

Where, $[C^{21}] = [C^{12}]$ and $[C^{31}]^{Tr} = -[C^{32}]^{Tr} = -[C^{23}] = [C^{13}]$.

The elements of the matrices $[C^{\alpha\beta}]$ are functions of laminate properties as well as s_1 and s_2. In the above expression $[C^{31}]^{Tr}$ indicates transpose of $[C^{31}]$.

For the purpose of carrying out the algebraic manipulations which are necessary to reduce the mixed boundary value problem to a set of integral equations, the following transformations are introduced.

$$
s_1 = \zeta\cos\phi/\ell_1
$$
$$
\qquad \text{(A-2.6)}
$$
$$
s_2 = \zeta\sin\phi/\ell_2
$$

$$
x_1 = \ell_1 r\cos\theta
$$
$$
\qquad \text{(A-2.7)}
$$
$$
x_2 = \ell_2 r\sin\theta
$$

where ℓ_1 and ℓ_2 are two parameters, chosen in a manner such that the disbond shape can be mapped on to a region which is close to the unit circle $r<1$. In particular an elliptic shaped disbond with semiaxes L_1 and L_2 can be mapped on to the circle $r=1$ by chosing $\ell_i=L_i/H_o$.

In terms of the variables ζ,ϕ the matrices $[C^{\alpha\beta}]$ ($\alpha,\beta=1,2$) can be written in the following fashion.

$$[C^{\alpha\beta}] = \zeta^2[C^{1^{\alpha\beta}}] + [C^{2^{\alpha\beta}}] \tag{A-2.8}$$

where,

$$[C^{2^{11}}] = [C^{2^{22}}] = -[C^{2^{12}}] = -[C^{2^{21}}] = \frac{1}{h^2}\begin{bmatrix} e_{55} & e_{45} \\ e_{45} & e_{44} \end{bmatrix} \tag{A-2.9}$$

$$c^{1^{\alpha\beta}}_{11} = E_1^{\alpha\beta}\eta_1^2 + E_2^{\alpha\beta}\eta_2^2 + 2E_3^{\alpha\beta}\eta_1\eta_2$$

$$c^{1^{\alpha\beta}}_{12} = c^{1^{\alpha\beta}}_{21} = E_3^{\alpha\beta}\eta_1^2 + E_4^{\alpha\beta}\eta_2^2 + E_5^{\alpha\beta}\eta_1\eta_2 \tag{A-2.10}$$

$$c^{1^{\alpha\beta}}_{22} = E_2^{\alpha\beta}\eta_1^2 + E_6^{\alpha\beta}\eta_2^2 + 2E_4^{\alpha\beta}\eta_1\eta_2$$

$$\eta_1 = \cos\phi/\ell_1$$

$$\tag{A-2.11}$$

$$\eta_2 = \sin\phi/\ell_2$$

and

$$E_1^{11} = a_{11} + \{d_{11}\} + (b_{11})$$

$$E_2^{11} = a_{66} + \{d_{66}\} + (b_{66})$$

$$E_3^{11} = a_{16} + \{d_{16}\} + (b_{16})$$

(A-2.12)

$$E_4^{11} = a_{26} + \{d_{26}\} + (b_{26})$$

$$E_5^{11} = a_{12} + a_{66} + \{d_{12}+d_{66}\} + (b_{12}+b_{66})$$

$$E_6^{11} = a_{22} + d_{22} + (b_{22})$$

Expressions for E_j^{22} (j=1,6) are the same as (A-2.12) with signs of the terms within parantheses changed to negative. To obtain $E_j^{12} = E_j^{21}$ (j=1,6) it is necessary to drop from (A-2.12) the terms in the parantheses and change the signs of the terms in brackets to negative.

$[C^{33}]$ and $[C^{13}]$ are given by:

$$[C^{33}] = \zeta^2 c^{33}_1$$

(A-2.13)

$$[C^{13}] = \zeta [C^{13}_1]$$

where, $c_1^{33} = (e_{55}+N_{11})\eta_1^2 + 2(e_{45}+N_{12})\eta_1\eta_2 + (e_{44}+N_{22})\eta_2^2$

$c_{11}^{13\,1} = (e_{55}\eta_1+e_{45}\eta_2)/h$

$$(A-2.14)$$

$c_{21}^{13\,1} = (e_{45}\eta_1+e_{44}\eta_2)/h$

TRACTION FREE CONDITION ON UPPER SURFACE

The top surface of laminate 1 (fig. 1) is free of tractions and therefore:

$$\bar{t}_1^+ = \bar{t}_2^+ = \bar{t}_3^+ = 0 \qquad (A-2.15)$$

Elimination of $\bar{u}_1^+$ and $\bar{u}_2^+$ from (A-2.5) results in an expression of the following form.

$$[\bar{t}^-] = \begin{bmatrix} \bar{t}_1^- \\ \\ \bar{t}_2^- \\ \\ -i\bar{t}_3^- \end{bmatrix} = \overset{(1)}{[F]}[\bar{u}^-] = \left[\begin{array}{c|c} \begin{matrix}11\\F\\(2\times2)\end{matrix} & \begin{matrix}12\\F\\(2\times2)\end{matrix} \\ \hline \begin{matrix}21\\F\\(1\times2)\end{matrix} & \begin{matrix}22\\F\\(1\times1)\end{matrix} \end{array}\right] \begin{bmatrix} \bar{u}_1^- \\ \bar{u}_2^- \\ \\ -i\bar{u}_3 \end{bmatrix} \qquad (A-2.16)$$

where

$$[F^{11}] = [C^{11}] - [C^{22}][C^{21}]^{-1}[C^{12}]$$

$$[F^{12}] = [F^{21}]^{Tr} = [C^{23}] - [C^{21}][C^{11}]^{-1}[C^{13}]$$ (A-2.17)

$$[F^{22}] = [C^{33}] - [C^{31}][C^{11}]^{-1}[C^{13}]$$

The matrix [F] can also be written as:

$$[\overset{(1)}{F}] = [\overset{(1)}{F^*}] + [\overset{(1)}{F^0}]$$ (A-2.18)

where $[F^*]$ and $[F^0]$ are of the following form.

$$[\overset{(1)}{F^*}] = \zeta^2 \begin{bmatrix} f_{11}^1 & f_{12}^1 & 0 \\ f_{21}^1 & f_{22}^1 & 0 \\ 0 & 0 & f_{33}^1 \end{bmatrix} + \zeta \begin{bmatrix} 0 & 0 & f_{13}^2 \\ 0 & 0 & f_{23}^2 \\ f_{31}^2 & f_{32}^2 & 0 \end{bmatrix} + \begin{bmatrix} f_{11}^3 & f_{12}^3 & 0 \\ f_{21}^3 & f_{22}^3 & 0 \\ 0 & 0 & f_{33}^3 \end{bmatrix} .$$

(A-2.19)

The elements $f_{\alpha\beta}^j$ (j=1,2,3) are functions of η_1 and η_2 and

$$[\overset{(1)}{F^0}] = \begin{bmatrix} f^0_{11} & f^0_{12} & \zeta f^0_{13} \\ f^0_{21} & f^0_{22} & \zeta f^0_{23} \\ \zeta f^0_{31} & \zeta f^0_{32} & f^0_{33} \end{bmatrix} \qquad (A-2.20)$$

The elements $f^0_{\alpha\beta}$ can be written as:

$$f^0_{\alpha\beta} = (\zeta^2 f^{01}_{\alpha\beta} + f^{02}_{\alpha\beta})/(\zeta^4 f^{*1} + \zeta^2 f^{*2} + f^{*3}) \qquad (A-2.21)$$

where $f^{0j}_{\alpha\beta}$ (j=1,2) and f^{*j} (j=1,2,3) are functions of η_1 and η_2 only.

LOWER SURFACE RESTING ON ELASTIC FOUNDATION

The lower surface of laminate 2 (fig. 1) is either traction free or rests on an elastic foundation. When it rests on elastic support one has the following conditions.

$$\bar{t}^-_j + K^0_j \bar{u}^-_j = 0 \; ; \; j=1,2$$

$$\qquad (A-2.22)$$

$$\bar{t}^-_3 + K^0_3 \bar{u}_3 = 0$$

where $K^0_j = K^S_j H^4_0/D_0$, K^S_j (j=1,2,3) being modulus of the elastic subgrade (traction to cause unit deflection) in x-, y- and z-directions, respectively. Substitution of (A-2.22) in (A-2.5)

-113-

and elimination of $\bar{u}_1^-$ and $\bar{u}_2^-$ result in a relationship of the form given below.

$$[\bar{t}^+] = \begin{bmatrix} \bar{t}_1^+ \\ \\ \bar{t}_2^+ \\ \\ -i\bar{t}_3^+ \end{bmatrix} = \overset{(2)}{[F]}[\bar{u}^+] = \overset{(2)}{[F]} \begin{bmatrix} \bar{u}_1^+ \\ \\ \bar{u}_2^+ \\ \\ -i\bar{u}_3 \end{bmatrix} \qquad (A-2.23)$$

where $\overset{(2)}{[F]}$ has the same form as $\overset{(1)}{F}$ (see equations A-2.18 – A-2.21).

CONDITIONS AT INTERFACE

Transform of the traction vector ($[\bar{t}]=[\bar{t}_1,\bar{t}_2,-i\bar{t}_3]$) acting on laminate 1 or 2 at the interface containing the disbond is related to the transform of displacement vector ($[\bar{u}]=[\bar{u}_1,\bar{u}_2,-i\bar{u}_3]$) of the same laminate at the same interface in terms of the stiffness matrices $\overset{(1)}{[F]}$ or $\overset{(2)}{[F]}$ by means of equations (A-2.16) and (A-2.23). In what follows tractions and displacements on laminates 1 and 2 will be identified by superscripts – and +, respectively. Since the applied tractions on top and bottom surfaces of the disbond (as well as everywhere else on the interface) are equal in magnitude and opposite in sign, one has the following identity.

$$[\bar{t}^-] + [\bar{t}^+] = 0 \qquad (A-2.24)$$

-114-

Furthermore, if $u_k^*(x_1, x_2)$, k=1,2,3 are the difference between the displacements (at the interface) of laminates 1 and 2 in x-, y-, z-directions, then:

$$[\bar{u}^-] - [\bar{u}^+] = [\bar{u}^*] = [\bar{u}_1^*, \bar{u}_2^*, -i\bar{u}_3^*] \qquad \text{(A-2.25)}$$

where $\bar{u}_k^*$, k=1,2,3 are the transforms of u_k^*. The four equations (A-2.16) and (A-2.23-A-2.25) can now be formally solved and the transformed tractions at the interface can be expressed as:

$$[\bar{t}^-] = -[\bar{t}^+] = [G][\bar{u}^*] \qquad \text{(A-2.26)}$$

where [G] is given by the following relations.

$$[G] = [\overset{(1)}{F}][\overset{(1)}{F} + \overset{(2)}{F}]^{-1}[F^r] + [\overset{(1)}{F^0}][\widetilde{F^*}]^{-1}[\overset{(2)}{F^*}]$$
$$\text{(A-2.27)}$$
$$+ [\overset{(1)}{F^*}][\widetilde{F^*}]^{-1}[\overset{(2)}{F^*}]$$

$$[\overset{(i)}{F}] = [\overset{(i)}{F^*}] + [\overset{(i)}{F^0}] \qquad \text{(as in (A-2.18))}$$

$$[\widetilde{F^*}] = [\overset{(1)}{F^*}] + [\overset{(2)}{F^*}] \qquad \text{(A-2.28)}$$

and

$$[F^r] = [\overset{(2)}{F^0}][\widetilde{F^*}]^{-1}[\overset{(1)}{F^*}] - [\overset{(1)}{F^0}][\widetilde{F^*}]^{-1}[\overset{(2)}{F^*}]. \qquad \text{(A-2.29)}$$

The matrix [G] can also be expressed as:

$$[G] = \zeta^2 [G^1] + \zeta [G^2] + [G^3] + [G^4] \qquad \text{(A-2.30)}$$

where the matrices $[G^j]$ (j=1,4) are symmetric and the elements of the matrices are such that:

$$g^1_{13} = g^1_{23} = g^3_{13} = g^3_{23} = g^2_{11} = g^2_{12} = g^2_{22} = g^2_{33} = 0. \qquad \text{(A-2.31)}$$

Other non-zero elements of $[G^j]$ (j=1,2,3) are functions of η_1, η_2 and properties of the two laminates.

The matrix $[G^4]$ is of the form:

$$[G^4] = \begin{bmatrix} g^4_{11} & g^4_{12} & \zeta g^4_{13} \\ g^4_{21} & g^4_{22} & \zeta g^4_{23} \\ \zeta g^4_{31} & \zeta g^4_{32} & g^4_{33} \end{bmatrix} \qquad \text{(A-2.32)}$$

where $g^4_{\alpha\beta} = g^{4*}_{\alpha\beta} (\zeta^2)/g^* (\zeta^2)$, $\alpha, \beta = 1,2,3$; $g^{4*}_{\alpha\beta}$ and g^* being polynomials of ζ^2 with coefficients of the powers of ζ^2, which are functions of η_1 and η_2 and properties of the laminates. It is noted that the degree of the polynomial g^* exceeds that of $g^{4*}_{\alpha\beta}$ by unity.

A SET OF INTEGRAL EQUATIONS FOR ELLIPTIC DISBOND

The displacements of the two laminat.   : the interface differ only over the area of the disbond which will be assumed to be an ellipse in $x_1 x_2$ plane with semiaxes ℓ_1 and ℓ_2. Further, the ellipse is mapped on to a unit circle ($r \leq 1$) by the transformation (A-2.7). It is possible to expand the discontinuity in the displacements u_k^* across the disbond as well as the tractions acting on the top surface of the disbond in the form:

$$u_k^*(r',\theta) = u_k^*(x_1,x_2) = \sum_{p=-\infty}^{\infty} r'^{|p|} u_{kp}^*(r'^2) e^{ip\theta}; \quad r' \leq 1; \quad k=1,2,3$$

$$= 0 \quad r' \geq 1 \tag{A-2.33}$$

$$t_j^-(r,\psi) = t_j^-(x_1,x_2) = \sum_{m=-\infty}^{\infty} t_{jm}(r) e^{im\psi}; \quad k=1,2,3 \tag{A-2.34}$$

where $u_{k(-p)}^*$ and $t_{k(-p)}$ are complex conjugates of $u_{k\,p}^*$ and $t_{k\,p}$, respectively.

Taking multiple Fourier transform of u_k^* (as expressed in equation A-2.33) results in:

$$\bar{u}_k^*(\zeta,\phi) = \bar{u}_k^*(s_1,s_2) = \int_{-\infty}^{\infty} \int_{-\infty}^{\infty} u_k^*(x_1,x_2) e^{i(s_1 x_1 + s_2 x_2)} dx_1 dx_2$$

$$= \ell_1 \ell_2 \sum_{p=-\infty}^{\infty} \int_0^1 \int_0^{2\pi} r'^{|p|+1} u_{kp}^*(r'^2) e^{ip\theta} e^{i\zeta r' \cos(\theta-\phi)} d\theta dr'$$

$$\tag{A-2.35}$$

Use of the identity (ref. 26)

$$\int_0^{2\pi} e^{ip\theta} e^{i\zeta r' \cos(\theta-\phi)} d\theta = 2\pi e^{-ip\phi} (i)^p J_p(\zeta r') \qquad \text{(A-2.36)}$$

yields

$$\bar{u}_k^*(\zeta,\phi) = 2\pi \ell_1 \ell_2 \sum_{p=-\infty}^{\infty} (i)^p e^{-ip\phi} \int_0^1 r'^{|p|+1} u_{kp}^*(r^2) J_p(\zeta r') dr' \qquad \text{(A-2.37)}$$

where J_p denotes Bessel function of the first kind of order p.

In what follows the following relations and substitutions are utilized.

$$t_j^-(r,\psi) = t_j^-(x_1,x_2) = \frac{1}{4\pi^2} \int_{-\infty}^{\infty} \int_{-\infty}^{\infty} \bar{t}_j^-(s_1,s_2) e^{-i(s_1 x_1 + s_2 x_2)} ds_1 ds_2$$

$$= \frac{1}{4\pi^2 \ell_1 \ell_2} \int_0^{\infty} \int_0^{2\pi} \zeta \, \bar{t}j^-(\zeta,\phi) e^{-i\zeta r \cos(\psi-\phi)} d\phi d\zeta \qquad \text{(A-2.38)}$$

$$t_{jm}(r) = \frac{1}{2\pi} \int_0^{2\pi} t\bar{j}^-(r,\psi) e^{-im\psi} d\psi \qquad \text{(A-2.39)}$$

$$\int_0^{2\pi} e^{-im\psi} e^{-i\zeta r \cos(\psi-\phi)} d\psi = 2\pi (-i)^m e^{-im\phi} J_m(\zeta r) \qquad \text{(A-2.40)}$$

$$\frac{d}{dr'} u_{kp}^*(r'^2) = r' u_{kp}(r'^2) \tag{A-2.41}$$

$$u_{kp}(r'^2) = u_{kp}^R(r'^2) \div i\, u_{kp}^I(r'^2) \tag{A-2.42}$$

$$t_{jm}(r) = t_{jm}^R(r^2) + i\, t_{jm}^I(r^2) \tag{A-2.43}$$

For elements g_{11}, g_{12}, and g_{33} of matrix G (in equation A-2.30)

$$\int_0^{2\pi} g_{jk}(\zeta,\phi) e^{i(p-m)\phi} d\phi = 2\int_0^{\pi} g_{jk}(\zeta,\phi) e^{i(p-m)\phi} d\phi; \quad p-m=\text{even}$$

$$= 0 \qquad\qquad p-m=\text{odd}$$

$$\tag{A-2.44}$$

For elements g_{13} and g_{23} of matrix [G]

$$\int_0^{2\pi} g_{jk}(\zeta,\phi) e^{i(p-m)\phi} d\phi = 0 \qquad\qquad ;\ p-m=\text{even}$$

$$= 2\int_0^{\pi} g_{jk}(\zeta,\phi) e^{i(p-m)\phi} d\phi; \quad p-m=\text{odd}$$

$$\tag{A-2.45}$$

(A-2.38) and (A-2.39) are the laws of inversion of Fourier transforms, (A-2.40) is an identity (ref. 26) and (A-2.44) as well as (A-2.45) follow from the properties of the elements of g_{jk} of matrix [G]. Because of (A-2.44) and (A-2.45) the problem may be divided into two parts such that for part 1:

$$
-\begin{bmatrix} t^R_{1(2p)} \\ t^I_{2(2p)} \\ t^R_{3(2p+1)} \end{bmatrix} = \begin{bmatrix} t^{(1)}_{1p_1} \\ t^{(1)}_{2p_2} \\ t^{(1)}_{3p_3} \end{bmatrix} , \quad -\begin{bmatrix} t^I_{1(2p)} \\ t^R_{2(2p)} \\ t^I_{3(2p)} \end{bmatrix} = \begin{bmatrix} t^{(2)}_{1p_1} \\ t^{(2)}_{2p_2} \\ t^{(2)}_{3p_3} \end{bmatrix}
$$

$$
\begin{bmatrix} \alpha_{2p} u^R_{1(2p)} \\ \alpha_{2p} u^I_{2(2p)} \\ u^R_{3(2p+1)} \end{bmatrix} = \begin{bmatrix} u^{(1)}_{1p_1} \\ u^{(1)}_{2p_2} \\ u^{(1)}_{3p_3} \end{bmatrix} , \quad \begin{bmatrix} \alpha_{2p} u^I_{1(2p)} \\ \alpha_{2p} u^R_{(2p)} \\ u^I_{3(2p+1)} \end{bmatrix} = \begin{bmatrix} u^{(2)}_{1p_1} \\ u^{(2)}_{2p_2} \\ u^{(2)}_{3p_3} \end{bmatrix}
$$

(A-2.46)

and for part 2:

$$
-\begin{bmatrix} t^R_{1(2p+1)} \\ t^I_{2(2p+1)} \\ t^R_{3(2p)} \end{bmatrix} = \begin{bmatrix} t^{(1)}_{1p_1} \\ t^{(1)}_{2p_2} \\ t^{(1)}_{3p_3} \end{bmatrix} , \quad -\begin{bmatrix} t^I_{1(2p+1)} \\ t^R_{2(2p+1)} \\ t^R_{3(2p)} \end{bmatrix} = \begin{bmatrix} t^{(2)}_{1p_1} \\ t^{(2)}_{2p_2} \\ t^{(1)}_{3p_3} \end{bmatrix}
$$

$$
\begin{bmatrix} u^R_{1(2p+1)} \\\\ u^I_{2(2p+1)} \\\\ \alpha_{2p} \, u^R_{3(2p)} \end{bmatrix}
=
\begin{bmatrix} u^{(1)}_{1p_1} \\\\ u^{(1)}_{2p_2} \\\\ u^{(1)}_{3p_3} \end{bmatrix}
,
\begin{bmatrix} u^I_{1(2p+1)} \\\\ u^R_{2(2p+1)} \\\\ \alpha_{2p} \, u^I_{3(2p)} \end{bmatrix}
=
\begin{bmatrix} u^{(2)}_{1p_1} \\\\ u^{(2)}_{2p_2} \\\\ u^{(2)}_{3p_3} \end{bmatrix}
$$

(A-2.47)

where p varies from $0,1,2\ldots\infty$, and $\alpha_{2p}=1/2$, $p=0$; $\alpha_{2p}=1$, $p>1$.

Substitution of (A-2.37) in (A-2.26) as well as use of (A-2.38 - A-2.47) yield the following set of equations after integration by parts with respect to r' and utilization of the condition $u^*_{kp}(1)=0$.

$$
t^{(q_1)}_{jm_j}(r) = \frac{2}{\pi} \sum_{q_2=1}^{2} \sum_{k=1}^{3} \sum_{p=0}^{\infty} (-1)^{p_k - m_j} \int_0^\infty \int_0^\pi g_{jk}(\zeta,\phi) \, \gamma^{(q_1 q_2)}_{jk}(m_j, p_k, \phi) J_{m_j}(\zeta r)
$$

$$
\int_0^1 r'^{p_k+2} J_{p_{k+1}}(\zeta r') \, u^{(q_2)}_{kp_k}(r'^2) dr' d\phi d\zeta
$$

(A-2.48)

$$
\begin{aligned}
&; \; j = 1,\ldots 3 \\\\
&\quad m = 0,1,\ldots\infty \\\\
&\quad q_1 = 1,2
\end{aligned}
$$

where the repeated indices jk do not indicate summation and

-121-

$$m_j = 2m \quad , \; p_j = 2p \qquad \text{for } j=1,2$$

$$\qquad\qquad\qquad\qquad\qquad\qquad\qquad ; \text{ for part 1}$$

$$m_j = 2m+1, \; p_j = 2p+1 \qquad \text{for } j=3$$

$$(\text{A-2.49})$$

$$m_j = 2m+1, \; p_j = 2p+1 \qquad \text{for } j=1,2$$

$$\qquad\qquad\qquad\qquad\qquad\qquad\qquad ; \text{ for part 2}$$

$$m_j = 2m \quad , \; p_j = 2p \qquad \text{for } j=3$$

and $\gamma_{jk}^{(q_1 q_2)}$ $(q_1, q_2 = 1,2; \; j,k = 1,2,3)$ are given by four [3x3] matrices as given below.

$$(11) \; [\gamma] = \begin{bmatrix} \cos m_1\phi\cos p_1\phi & -\cos m_1\phi\sin p_2\phi & \cos m_1\phi\cos p_3\phi \\ -\sin m_2\phi\cos p_1\phi & \sin m_2\phi\sin p_2\phi & -\sin m_2\phi\cos p_3\phi \\ \cos m_3\phi\cos p_1\phi & -\cos m_3\phi\sin p_2\phi & \cos m_3\phi\cos p_3\phi \end{bmatrix}$$

$$(12) \; [\gamma] = \begin{bmatrix} -\cos m_1\phi\sin p_1\phi & \cos m_1\phi\cos p_2\phi & -\cos m_1\phi\sin p_3\phi \\ \sin m_2\phi\sin p_1\phi & -\sin m_2\phi\cos p_2\phi & \sin m_2\phi\sin p_3\phi \\ -\cos m_3\phi\sin p_1\phi & \cos m_3\phi\cos p_2\phi & -\cos m_3\phi\sin p_3\phi \end{bmatrix}$$

$$(\text{A-2.50})$$

$$(21) \; [\gamma] = \begin{bmatrix} -\sin m_1\phi\cos p_1\phi & \sin m_1\phi\sin p_2\phi & -\sin m_1\phi\cos p_3\phi \\ \cos m_2\phi\cos p_1\phi & -\cos m_2\phi\sin p_2\phi & \cos m_2\phi\cos p_3\phi \\ -\sin m_3\phi\cos p_1\phi & \sin m_3\phi\sin p_2\phi & -\sin m_3\phi\cos p_3\phi \end{bmatrix}$$

$$(22) \; [\gamma] = \begin{bmatrix} \sin m_1\phi\sin p_1\phi & -\sin m_1\phi\cos p_2\phi & \sin m_1\phi\sin p_3\phi \\ -\cos m_2\phi\sin p_1\phi & \cos m_2\phi\cos p_2\phi & -\cos m_2\phi\sin p_3\phi \\ \sin m_3\phi\sin p_1\phi & -\sin m_3\phi\cos p_2\phi & \sin m_3\phi\sin p_3\phi \end{bmatrix}$$

For $0 \leq r < 1$, equations (A-2.48) are a set of integral equations, which must be solved to determine the displacements and stress states in the disbonded laminate.

SOLUTION OF THE SET OF INTEGRAL EQUATIONS

The discontinuities in displacements across the disbond, u_k^* can be calculated with the help of equations (A-2.46 or A-2.47), (A-2.42), (A-2.41), and (A-2.33) after the functions $u_{kp_k}^{(q_2)}$ are evaluated by solving (A-2.48). The left-hand side of (A-2.48) contains functions which are determined from the prescribed tractions on the disbond surfaces by the use of (A-2.39), (A-2.43), and (A-2.46 or A-2.47). To solve the set of integral equations (A-2.48), the functions $u_{kp_k}^{(q)}(r'^2)$ are expanded in a series of Legendre polynomials $P_{n-1}(2r'^2-1)$, $n=1,2,\ldots\infty$.

$$u_{kp_k}^{(q)}(r'^2) = \sum_{n=1}^{\infty} u_{kpqn} \, P_{n-1}(2r'^2-1) \qquad (A-2.51)$$

Substitution of (A-2.51) in (A-2.48) and use of the relations (A-2.52 and A-2.54) given below (ref. 26):

$$P_{n-1}(2r'^2-1) = \sum_{n_1=1}^{n} \frac{X_{n_1 n}}{X_{n_1}^*} (1-r'^2)^{n_1-1} \qquad (A-2.52)$$

Where

$$\chi_{1n} = 1 \text{ and } \chi_1^* = 1$$

$$\chi_{n_1 n} = \frac{(-n+1)_{n_1-1}(n)_{n_1-1}}{(n_1-1)!} \text{ and } \chi_{n_1}^* = (n_1-1)! ; \quad n_1 = 1,2\ldots n$$

$$(n)_{n_1-1} = n(n+1)(n+2)\ldots\ldots(n+n_1-2)$$

(A-2.53)

$$\int_0^1 r'^{p_k+2} J_{p_k+1}(\zeta r')(1-r'^2)^{n_1-1} dr' = 2^{n_1-1} \chi_{n_1}^* \zeta^{-n_1} J_{p_k+n_1+1}(\zeta)$$

(A-2.54)

as well as integration of both sides of the resulting expression
between 0 to r after multiplying with r^{m_j+1} results in:

$$t_{jm_j}^{*(q_1)}(r) = \frac{2}{\pi} \sum_{q_2=1}^{2} \sum_{k=1}^{3} \sum_{p=0}^{\infty} \sum_{n=1}^{\infty} (-1)^{p_k-m_j} u_{kpq_2 n} \sum_{n_1=1}^{n} \chi_{n_1 n} 2^{n_1-1} r^{m_j+1}$$

$$\int_0^{\infty} \int_0^{\pi} \zeta^{-n_1-1} g_{jk}(\zeta,\phi) \gamma_{jk}^{(q_1 q_2)}(m_j, p_k, \phi) J_{p_k+n_1+1}(\zeta) J_{m_j+1}(\zeta r) d\phi d\zeta$$

(A-2.55)

Where:

$$\overset{(q)}{t^{*}_{jm_j}}(r) = \int_0^r \overset{(q)}{t}_{jm_j}(r') r'^{m_j+1} \, dr' \qquad \text{A-2.56)}$$

If one expands $\overset{(q_1)}{t^{*}_{mj}}(r)$; $0 \le r < 1$ in a series of Legendre polynomials $P_{n'-1}(2r^2-1)$, $n'=1,2.\ .\ .\infty$, then the coefficients are given:

$$t_{jm}q_1 n' = 4 \int_0^1 r \; \overset{(q_1)}{t^{*}_{jm_j}}(r) \; P_{n'-1}(2r^2-1) \; dr$$

$$= \sum_{q_2=1}^{2} \sum_{k=1}^{3} \sum_{p=0}^{\infty} \sum_{n=1}^{\infty} L_{kpq_2n}^{jmq_1n'} \; u_{kpq_2n}; \quad \begin{matrix} j =1,2,3 \\ m =0,1,2...\infty \\ q_1=1,2 \\ n'=1,2.....\infty \end{matrix} \qquad \text{(A-2.57)}$$

Equation (A-2.57) is an infinite system of linear algebraic equations involving the unknowns u_{kpq_2n}. The coefficients $L_{kpq_2n}^{jmq_1n'}$ are given by:

$$L_{kpq_2n}^{jmq_1n'} = \frac{2}{\pi} (-1)^{p_k - m_j} \sum_{n_1=1}^{n} \sum_{n_1'=1}^{n'} X_{n_1 n} X_{n_1' n'} \; 2^{n_1 + n_1'}$$

$$\qquad\qquad\qquad\qquad\qquad\qquad\qquad\qquad\qquad \text{(A-2.58)}$$

$$\int_0^{\infty} \int_0^{\pi} \zeta^{-n_1-n'-1} \; g_{jk}(\zeta,\phi) \; \overset{(q_1 q_2)}{\gamma_{jk}}(m_j, p_k, \phi) J_{p_k+n_1+1}(\zeta) J_{m_j+n_1'+1}(\zeta) \, d\phi \, d\zeta$$

g_{jk} are the elements of the matrix $[G]$ which is given in equation (A-2.31) and can be rewritten as the sum of four terms, i.e.:

$$[G] = \sum_{\beta=1}^{3} \zeta^{3-\beta} [G^{\beta}(\phi)] + [G^{4}(\zeta,\phi)] \qquad (A-2.59)$$

Substitution of (A-2.59) in (A-2.58) results in four infinite integrals, the first three of which can be evaluated in closed form by the use of the following relation (ref. 26):

$$\int_{0}^{\infty} \zeta^{-\lambda} J_{\mu}(\zeta) J_{\nu}(\zeta) d\zeta = \frac{\Gamma(\lambda)\Gamma(\lambda_1)}{2^{\lambda}\Gamma(\lambda_2)\Gamma(\lambda_3)\Gamma(\lambda_4)} \; ; \; \lambda_1, \lambda_2 > 0$$

$$= 0 \quad ; \; \lambda_2 \text{ or } \lambda_4 \leq 0 \qquad (A-2.60)$$

where

$$\lambda_1 = (\nu+\mu-\lambda+1)/2$$

$$\lambda_2 = (-\nu+\mu+\lambda+1)/2$$

$$\lambda_3 = (\nu+\mu+\lambda+1)/2$$

$$\lambda_4 = (\nu-\mu+\lambda+1)/2$$

and Γ denotes the Gamma function. It is necessary to evaluate the integral (A-2.60), only when λ and λ_{β}; $\beta=1,\ldots4$ are positive integers. Integration with respect to ϕ can be performed numerically by the formula given below.

$$\int_0^\pi \Omega(\phi) d\phi = \frac{\pi}{M_1} \sum_{\beta_1=0}^{M_1} \omega_{\beta_1}^1 \Omega(\phi_{\beta_1}) \qquad \text{(A-2.61)}$$

where

$$\omega_{\beta_1}^1 = 1/2 \qquad , \qquad \beta_1 = 0, M_1$$

$$= 1 \qquad , \qquad \beta_1 = 1, 2 \ldots M_1 - 1$$

$$\phi_{\beta_1} = \pi\beta_1/M_1 \quad , \quad \beta_1 = 0, 1 \ldots M_1.$$

The last integral, which is the contribution due to $[G^4]$ in (A-2.59 and A-2.30) contains more complicated functions of ζ and ϕ. In this study $[G^4]$ is evaluated numerically by the use of (A-2.27) for various values of ζ and ϕ and the integral is evaluated numerically by the formula:

$$\int_0^\infty \int_0^\pi \Lambda(\zeta,\phi) d\phi d\zeta = \frac{\pi}{M_1} \sum_{\beta_2=1}^{M_2} \sum_{\beta_1=0}^{M_1} \omega_{\beta_2}^2 \omega_{\beta_1}^1 \Lambda(\zeta_{\beta_2}, \phi_{\beta_1}) \qquad \text{(A-2.62)}$$

where,

$$\zeta_{\beta_2} = \frac{1 - \zeta_{\beta_2}^*}{1 + \zeta_{\beta_2}^*} \zeta_0$$

$$\omega_{\beta_2}^2 = \left[2\omega_{\beta_2}^* / (1 + \zeta_{\beta_2}^*)^2 \right] \zeta_0$$

$\zeta_{\beta_2}^*$ are the zeroes of Legendre polynomic $P_{M_2}(\zeta^*)$; $-1 < \zeta^* < 1$ and $\omega_{\beta_2}^*$ are the weights for Gaussion integration and ζ_0 is a multiplier chosen for obtaining rapid convergence of the integrals.

For the purpose of numerical solution it is necessary to truncate the infinite system (A-2.57):

$$m, \; p \; \leq \; m_{max}$$

$$n, \; n' \; \leq \; n_{max}.$$

Further, for laminates which are orthotropic with x,y axes as the principal material axes, the set of equations for u_{kp1n} and u_{kp2n} are uncoupled and can be solved separately.

CALCULATIONS OF STRAIN ENERGY RELEASE RATES

It follows from equations (A-2.33), (A-2.41), (A-2.42), (A-2.46), (A-2.47) and (A-2.51) that the derivatives of $u_k^*(r', \theta)$ as r' approaches 1 are given by:

$$\frac{\partial u_k^*}{\partial r'}\bigg|_{r' \to 1} = 2 \sum_{p=0}^{\infty} \sum_{n=1}^{\infty} [u_{kp1n}\cos p_k\theta - u_{kp2n}\sin p_k\theta]; \; k=1,3$$

$$= 2 \sum_{p=0}^{\infty} \sum_{n=1}^{\infty} [-u_{kp1n}\sin p_k\theta + u_{kp2n}\cos p_k\theta]; \; k=2$$

(A-2.63)

Denoting the displacement discontinuities in directions normal and tangential to the elliptical boundary of the disbond by U_I and U_{II}, respectively, and in z-direction by U_{III}, the rate of change of these quantities at the boundary in the direction x_I, normal to the boundary curve are given by:

$$U'_I = \frac{\cos\theta}{\ell_1} \frac{\partial u^*_1}{\partial r'} + \frac{\sin\theta}{\ell_2} \frac{\partial u^*_2}{\partial r'}$$

$$U'_{II} = \frac{\sin\theta}{\ell_2} \frac{\partial u^*_1}{\partial r'} + \frac{\cos\theta}{\ell_1} \frac{\partial u^*_2}{\partial r'} \qquad (A\text{-}2.64)$$

$$U'_{III} = \sqrt{\frac{\cos^2\theta}{\ell_1^2} + \frac{\sin^2\theta}{\ell_2^2}} \; \frac{\partial u^*_3}{\partial r'}$$

Since these derivatives are zero outside the disbond area, they have a discontinuity as the boundary is crossed. As will be seen next, the integrals of tractions imposed by one of the laminates on the other at the plane of the disbond with respect to the normal x_I also has a discontinuity, indicating existence of concentrated (line) forces at the disbond boundary. This is the type of force singularity which the laminated plate theory assumptions yield in contrast to the type of stress singularity encountered in 2-D or 3-D elasticity theories.

Substitution of (A-2.51-A-2.54) and (A-2.30) in (A-2.48) and omission of all terms which do not yield concentrated line forces on the elliptic boundary (r=1) yields the following expression from which the magnitudes of the concentrated forces are to be obtained.

$$t^{(q_1)c}_{jm_j}(r) = \frac{2}{\pi} \sum_{q_2=1}^{2} \sum_{k} \sum_{p=0}^{\infty} \sum_{n=1}^{\infty} (-1)^{p_k - m_j} u_{kpq_2n} \int_0^{\infty} \int_0^{\pi} g^1_{jk}(\phi) \; \gamma^{(q_1 q_2)}_{jk}(m_j, p_k, \phi)$$

$$\zeta \, J_{p_k+2}(\zeta) \, J_{m_j}(\zeta r) \, d\phi d\zeta \qquad (A\text{-}2.65)$$

For j=1,2 the summation over k is to be performed over k=1,2 and for j=3 k is taken equal to 3. This follows from (A-2.31). Integration with respect to ϕ can be performed numerically by the formula (A-2.61). The infinite integral (w.r.t. ζ) can be written as:

$$\int_0^\infty \zeta\, J_{p_k+2}(\zeta) J_{m_j}(\zeta r)\, d\zeta = r^{m_j-1} \frac{d}{dr}\left[\Omega(p_k, m_j, r)\right] \qquad \text{(A-2.66)}$$

where

$$\Omega(p_k, m_j, r) = r \int_0^\infty J_{p_k+2}(\zeta)\, J_1(\zeta r)\, d\zeta \qquad ;\ m_j = 0 \qquad \text{(A-2.67)}$$

$$= -r^{1-m_j} \int_0^\infty J_{p_k+2}(\zeta)\, J_{m_j-1}(\zeta r)\, d\zeta; \ m_j > 0 \qquad \text{(A-2.68)}$$

The expressions (A-2.67) and (A-2.68) are discontinuous at r=1 and can be expressed as (ref. 26):

$$\Omega(p_k, 0, 1^+) = 0$$

$$\Omega(p_k, 0, 1^-) = \frac{\Gamma(\frac{p_k+4}{2})}{\Gamma(\frac{p_k+2}{2})} \; F^h(\frac{p_k+4}{2}, -\frac{p_k}{2}, 2, 1)$$

and for $m_j > 0$

$$\Omega(p_k, m_j, 1^+) = -\frac{\Gamma(\frac{p_k+m_j+2}{2})}{\Gamma(\frac{m_j-p_k-2}{2})\Gamma(p_k+3)} \; F^h(\frac{p_k+m_j+2}{2}, -\frac{m_j-p_k-4}{2}, p_k+3, 1)$$

$$; \; m_j > p_k + 2$$

$$= 0 \; ; \; m_j \leq p_k + 2$$

$$\Omega(p_k, m_j, 1^-) = -\frac{\Gamma(\frac{p_k+m_j+2}{2})}{\Gamma(\frac{p_k-m_j+4}{2})\Gamma(m_j)} \; F^h(\frac{p_k+m_j+2}{2}, -\frac{p_k-m_j+2}{2}, m_j, 1)$$

$$; \; m_j < p_k + 4$$

$$= 0 \; ; \; m_j \geq p_k + 4 \qquad\qquad (A-2.69)$$

where $F^h(\mu_1, \mu_2, \mu_3, z)$ is the hypergeometric series with μ_1, μ_2 and μ_3 as integers, which terminates because of the fact that μ_2 is negative.

If x_I is the direction normal to the elliptic boundary with semiaxes ℓ_1 and ℓ_2, then the partial derivative of a function Λ with respect to x_I is given by:

$$\frac{\partial \Lambda}{\partial x_I} = \sqrt{\frac{\cos^2\theta}{\ell_1^2} + \frac{\sin^2\theta}{\ell_2^2}} \; \frac{\partial \Lambda}{\partial r} + \frac{\sin\theta\cos\theta(\ell_1^2 + \ell_2^2)}{\ell_1 \ell_2 \sqrt{\ell_2^2\cos^2\theta + \ell_1^2\sin^2\theta}} \; \frac{1}{r} \frac{\partial \Lambda}{\partial \theta}.$$

(A-2.70)

Therefore, the concentrated force components in nondimensional form are given by:

$$t_{jm_j}^{(q_1)} c = \frac{2}{\pi\sqrt{\dfrac{\cos^2\theta}{\ell_1^2} + \dfrac{\sin^2\theta}{\ell_2^2}}} \sum_{q_2=1}^{2} \sum_{k} \sum_{p=0}^{\infty} \sum_{n=1}^{\infty} (-1)^{p_k - m_j} u_{kpq_2 n}$$

$$[\Omega(p_k, m_j, 1^+) - \Omega(p_k, m_j, 1^-)] \int_0^\pi g_{jk}^1(\phi) \; \gamma_{jk}^{(q_1 q_2)}(p_k, m_j, \phi) d\phi$$

(A-2.71)

Summing over m and q_1, one has the following expression for forces in x-, y-, and z-directions:

$$t_j^C = \sum_{m=0}^{\infty} 2\alpha_{m_j} [-t_{jm_j}^{(1)C} \cos m_j \theta + t_{jm_j}^{(2)C} \sin m_j \theta] \quad ; \quad j=1,3$$

$$= \sum_{m=0}^{\infty} 2\alpha_{m_j} [t_{jm_j}^{(1)C} \sin m_j \theta - t_{jm_j}^C \cos m_j \theta] \quad ; \quad j=2$$

where, $\alpha_{m_j} = 1/2$; $m_j = 0$

$$= 1 \; ; \; m_j > 0 \tag{A-2.72}$$

If T_I^C and T_{II}^C are the forces in directions normal and tangential to the elliptic boundary, respectively, and T_{III}^C is the force in z-direction (in units of force), then:

$$T_I^C = (\frac{\cos\theta}{\ell_1} t_1^C + \frac{\sin\theta}{\ell_2} t_2^C) \frac{D_0}{H_0^2 \Delta}$$

$$T_{II}^C = (- \frac{\sin\theta}{\ell_2} t_1^C + \frac{\cos\theta}{\ell_1} t_2^C) \frac{D_0}{H_0^2 \Delta} \tag{A-2.73}$$

$$T_{III}^C = \frac{t_3^C D_0}{H_0^2}$$

where $\Delta = \sqrt{\frac{\cos^2\theta}{\ell_1^2} + \frac{\sin^2\theta}{\ell_2^2}}$

and D_0 and H_0 are the quantities introduced for nondimensionalization (see equation A-2.1).

The strain energy release rates for modes I, II, and III can then be calculated at various positions on the elliptic boundary by the relationship:

$$G_{I,II,III} = \frac{1}{2} T^C_{I,II,III} \ U'_{I,II,III}$$

(A-2.74)